COMILLAS
UNIVERSIDAD PONTIFICIA
ICAI

MASTER EN INGENIERIA INDUSTRIAL

TRABAJO FIN DE MASTER

Optimization of Composite Laminates for Aeroelastic Design of Flexible Aerodynamic Components through Coupled Aero-Structural Simulation

Autor: Alberto Caballero Valls

Director: Ignacio Granell Heredero

Madrid
febrero de 2026

Declaration of originality

I declare under my responsibility that the Project presented with the title **Optimization of composite laminates for aeroelastic design of flexible aerodynamic components through coupled aero-structural simulation** at the ICAI School of Engineering of the Comillas Pontifical University in the academic year **2025-2026** is of my authorship and has not been presented previously for other purposes. The Project is not plagiarised from any other, either totally or partially, and the information that has been taken from other documents is duly referenced.

Use of Artificial Intelligence[1]

I declare under my responsibility that (indicate the correct option):

☒ I have not used Artificial Intelligence in the preparation of this document.

☐ I have used Artificial Intelligence in the preparation of this document and/or Annex B under the conditions allowed by Comillas Pontifical University, i.e. applying Level 2 of the Perkins et al. (2024) Assessment Scale: "AI can be used for pre-task activities such as brainstorming, description and initial research. This level focuses on the use of AI for planning, synthesising and generating ideas, but assessments should emphasise the ability to develop and refine these ideas independently". Specifically, Artificial Intelligence has been used to:

(indicate here the concrete use that has been made of Artificial Intelligence)

CABALLERO VALLS ALBERTO - 51258446W   Firmado digitalmente por CABALLERO VALLS ALBERTO - 51258446W Fecha: 2026.05.23 14:28:03 +02'00'
Signature (student):
Date: 23-05-2026

[1] This declaration refers to the use of generative Artificial Intelligence to carry out the Project documents (Annex B and Memory). It does not apply to Projects where, by their nature, artificial intelligence must be used as part of them (application of machine learning techniques, neural networks, data analysis...).

Authorisation for Project delivery

Thesis supervisor	Thesis deputy supervisor (if any)
12/7/26	
Signature: Ignacio Granell Heredero	Signature:
Date: 12/07/2026	Date:

COMILLAS
UNIVERSIDAD PONTIFICIA
ICAI

MASTER EN INGENIERIA INDUSTRIAL

TRABAJO FIN DE MASTER

Optimization of Composite Laminates for Aeroelastic Design of Flexible Aerodynamic Components through Coupled Aero-Structural Simulation

Autor: Alberto Caballero Valls

Director: Ignacio Granell Heredero

Madrid
febrero de 2026

1 Resumen

1.1 Introducción

Este proyecto optimiza el laminado compuesto del alerón trasero de un Fórmula 1 para conseguir una deformación controlada bajo carga aerodinámica. El diseño reduce la resistencia al avance, conocido como "drag", en rectas manteniendo la carga aerodinámica en curvas.

Los circuitos de Fórmula 1 presentan carácteristicas distintas y para conseguir el mayor rendimiento posible, los equipos necesitan adaptar las configuraciones aerodinámicas en cada carrera. Los circuitos con alta velocidad media, como Monza requieren poca resistencia al avance para poder alcanzar la velocidad máxima, mientras que los circuitos de baja velocidad, como Mónaco con rectas cortas donde no se alcanzan velocidades tan altas, necesitan más carga aerodinámica para mejorar el agarre en curvas. Los equipos cambian diseños de los alerones y ajustan la suspensión para conseguir el mejor tiempo por vuelta posible.

Los estructuras fabricadas con laminados compuestos permiten controlar la rigidez variando los parámetros que definen el laminado, como el número de capas, el tipo de fibra usada y sus la orientación de cada capa. Este proyecto estudia cómo estos parámetros permiten flexionar el alerón de forma controlada, optimizando el compromiso entre resistencia al avance y carga aerodinámica mediante la propuesta de diseño de un alerón trasero de Formula 1 que cumpla con la normativa técnica de la temporada 2025 definida por la Federación Internacional del Automobilismo (FIA).

1.2 Metodología

El proyecto está compuesto de varios análisis:

1. Selección de materiales con Granta para los soportes, el núcleo de los componentes del alerón y el tipo fibra usada
2. Ingeniería inversa de un alerón de F1 para conseguir la geometría
3. Modelado CAD del alerón
4. Dinámica de fluidos para analizar el rendimiento aerodinámico (CFD) y conseguir el mapa de presiones en el alerón en el caso de estudio
5. Análisis estructural estático para comprobar que cumple con la normativa
6. Analísis de la interacción fluido-estructura (FSI) para conocer el valor y la manera en la que se deforma el alerón debido a la carga aerodinámica
7. Análisis modal de frecuencias para calcular las frecuencias naturales
8. Optimización multiobjetivo del laminado para poder definir el laminado que optimice los requisitos de diseño

El objetivo es capturar la interacción entre la deformación producida por la corriente de aire y el alerón para encontrar el laminado óptimo que mejore el rendimiento aerodinámico sin comprometer la resistencia estructural ni el cumplimiento normativo. El flujo completo del trabajo aparece en la figura 8, en la que el trabajo se divide en dos etapas. La primera es conseguir una geometría del alerón y una definición inicial de materiales y laminado que cumplan con la normativa. La segunda parte corresponde a la optimización del laminado para conseguir los objetivos de diseño definidos.

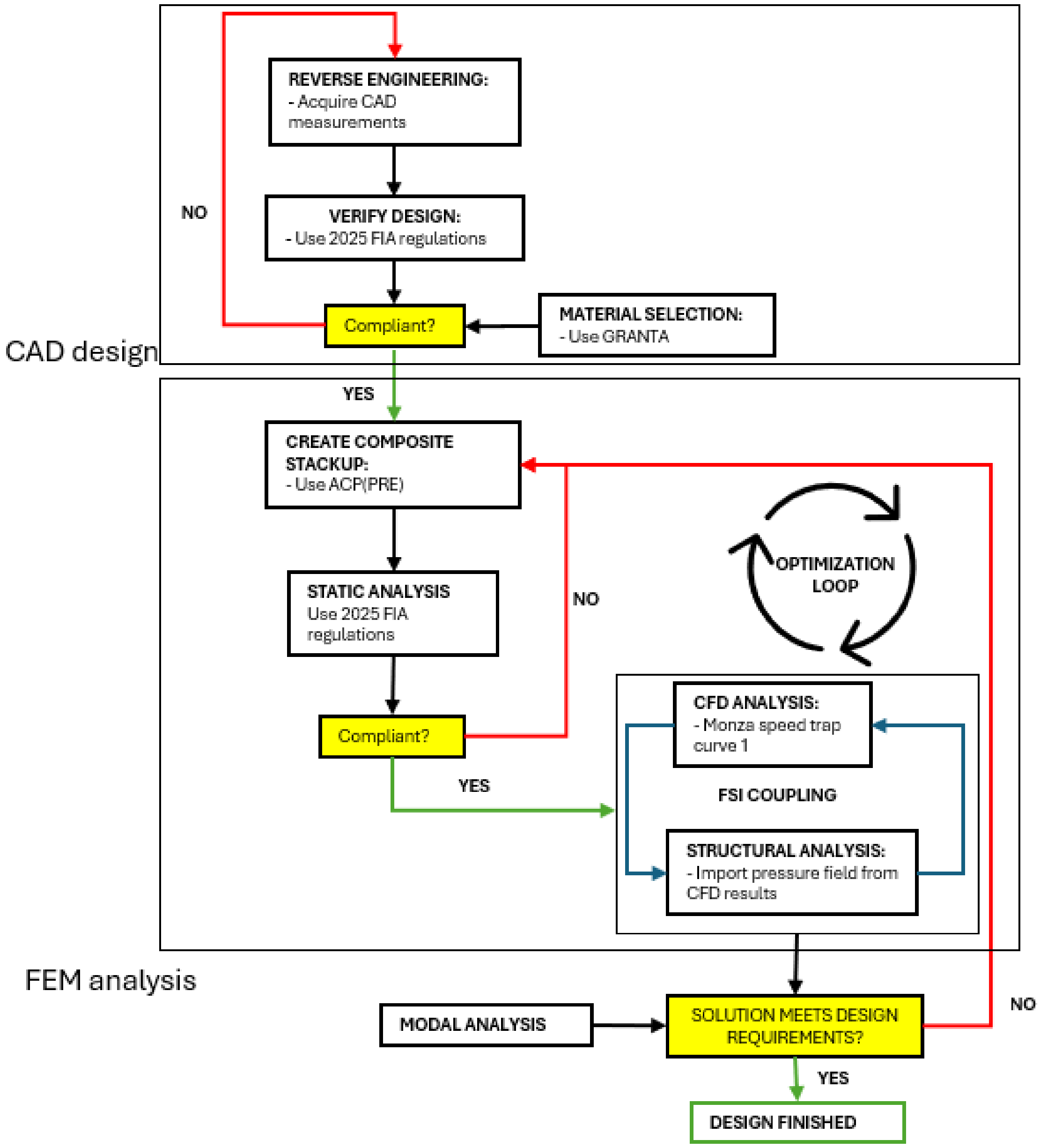

Figure 1: Flujo de trabajo del proyecto

1.3 Descripción del modelo

La Figura 9 muestra el modelo CAD final del alerón, donde el alerón principal está coloreado en rojo, el DRS en azul, los flaps en negro y los soportes en gris.

Figure 2: Modelo CAD final.

Se han analizado 20 laminados. La primera etapa de la optimización está formada por doce laminados, clasificados en cuatro de 4 capas, cuatro de 6 capas y cuatro de 8 capas, manteniendo las relaciones angulares entre configuraciones. Se ha elegido una configuración para continuar con la siguiente etapa de la optimización, donde se han estudiado 8 laminados.

1.4 Requisitos de diseño

Los requisitos que se han tenido en cuenta para el diseño del alerón son los siguientes:

1. **Casos de carga**:
   (a) Simulación estructural estática con las cargas de la normativa técnica 2025 de la FIA.
   (b) Simulación estructural dinámica con la velocidad máxima alcanzada al final de la recta principal del circuito de Monza.
2. **Objetivos estructurales**:
   (a) Conseguir una flexión estática máxima inferior a la descrita en la normativa
   (b) Tener una flexión dinámica de 20 mm en el caso estudiado

(c) Alcanzar una frecuencia natural del primer modo de vibración superior a 50 Hz para evitar resonancias $f_1 > 50$ Hz

(d) Conseguir un factor de seguridad > 1.5 según el criterio de Tsai-Wu en la unión metal-composite.

(e) Tener un valor de deformación cortante < 0.020

(f) Masa total < 1.25 kg con un espesor de capa ≤ 0.25 mm

1.5 Optimización multiobjetivo

La optimización ha tenido en cuenta los siguientes objetivos y condiciones:

- **Objetivo 1:** Minimizar masa buscando el menor número de capas de CFRP
- **Objetivo 2:** Conseguir un desplazamiento dínamico máximo del DRS de 20 mm
- **Condición:** Número mínimo de 4 capas para cumplir con la normativa FIA 2025
- **Variables:** Número de capas y ángulo de cada capa

1.5.1 Optimización por número de capas

La tabla 29 compara la deformación máxima y la masa de los 12 laminados propuestos en la primera etapa del proceso de optimización.

Configuración	Deformación	Masa
4 capas		
1 [woven 0 ud 0,ud 45, ud 0]	22.92 mm	316.2 g
2 [woven 0, ud 0, ud 45, ud 0]	22.49 mm	316.2 g
3 [woven 0, ud 0, ud 90, ud 0]	17.95 mm	316.2 g
4 [woven 0, ud 0, ud 45, ud -45]	21.09 mm	316.2 g
6 capas		
5 [woven 0, ud 0, ud 45, ud 0, ud -45, ud 0]	19.98 mm	474.3 g
6 [woven 0, ud 0, ud 45, ud 0, ud 45, ud 0]	21.26 mm	474.3 g
7 [woven 0, ud 0, ud 0, ud 90, ud 0, ud 0]	17.61 mm	474.3 g
8 [woven 0, ud 0, ud 45, ud 90, ud 45, ud 0]	16.85 mm	474.3 g
8 capas		
9 [woven 0, ud 0, ud 45, ud 0, ud 0, ud 45, ud 0, woven 0]	17.96 mm	632.4 g
10 [woven 0, ud 45, ud 0, ud 45, ud 45, ud 0, ud 45, woven 0]	17.62 mm	632.4 g
11 [woven 0, ud 0, ud 45, ud 90, ud 90, ud 45, ud 0, woven 0]	13.53 mm	632.4 g
12 [woven 0, ud -45, ud 0, ud 45, ud 45, ud 0, ud -45, woven 0]	16.39 mm	632.4 g

Table 1: Deformación máxima del DRS en cada configuración

La Figura 107 muestra las tendencias de cada configuración. La configuración C ($[woven0/ud0/ud90/ud0]_s$), mostrada en verde, mantiene mejor la rigidez longitudinal al tener menor variación entre la deformación con 4 capas y con 8 capas. Para continuar con las segunda fase del proceso de optimización, se ha elegido la configuración C con 4 capas debido a que tiene menor masa y tiene un valor de deformación máxima cercano al valor objetivo.

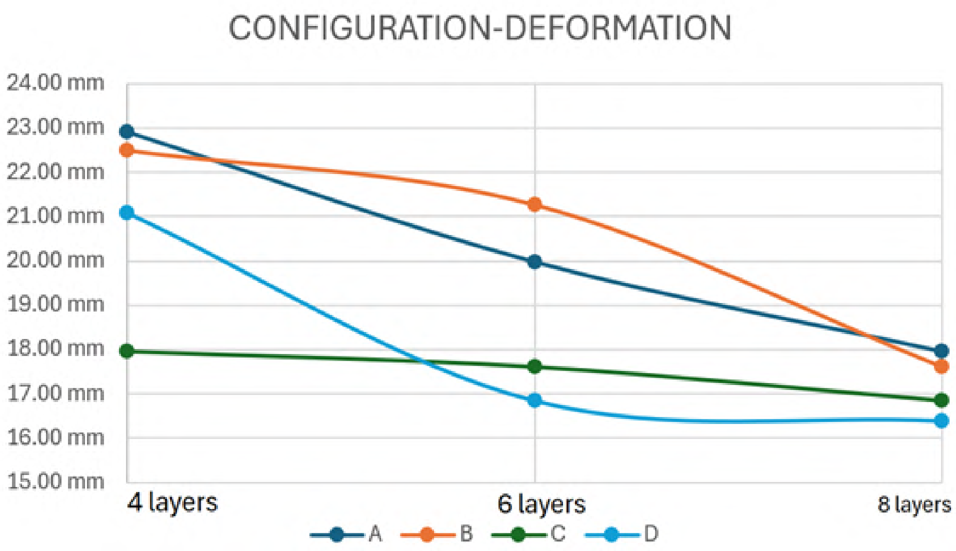

Figure 3: Tendencia deformación vs. número de capas

1.5.2 Optimización de ángulos

Se ha optimizado el ángulo θ en la configuración C de 4 capas ($[0/0/\theta/0]_s$). Los resultados de las simulaciones, mostrados en la figura 108 muestran que el valor óptimo es $\theta \approx 67°$.

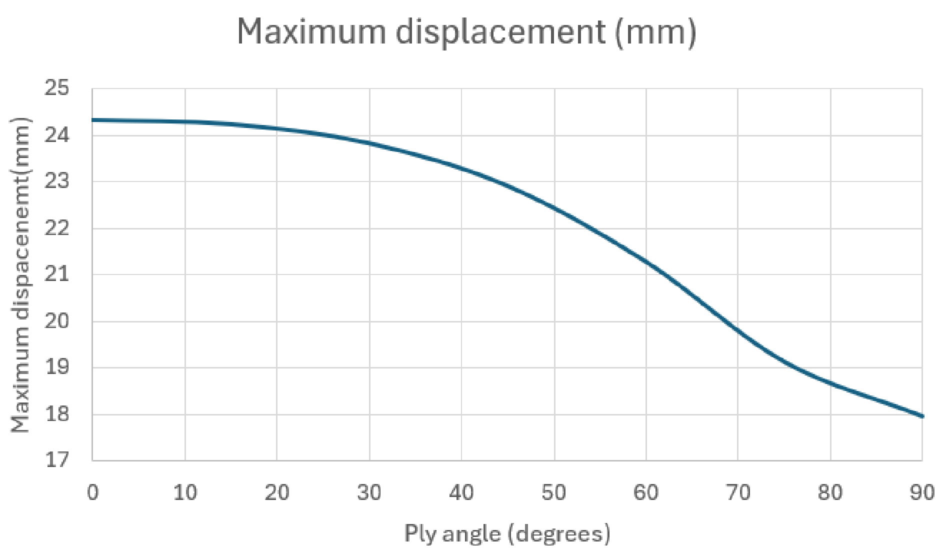

Figure 4: Desplazamiento DRS vs. ángulo θ

1.6 Resultados

La tabla 31 muestra el resultado final de los materiales usados en cada componente y la definición del laminado.

Table 2: Laminados finales optimizados.

Componente	Laminado	Espesor
DRS	$[woven(0°)/ud(0°)/ud(67°)/ud(0°)]_s$	1.00 mm
Flap	$[woven(0°)/ud(0°)/ud(0°)]_s$	0.75 mm
Alerón principal	$[woven(0°)/ud(0°)/ud(0°)]_s$	0.75 mm
Núcleo	Espuma Rohacell 71	–
Soportes	Aluminio 7055	–

La tabla 32 presenta cómo se ha cumplido cada objetivo.

Table 3: Cumplimiento de requisitos.

Requisito	Objetivo	Logrado
Deflexión estática	< 4 mm	< 2 mm
Deflexión dinámica	$= 20$ mm	20 mm
f_1	> 50 Hz	64.872 Hz
Factor seguridad	> 1.5	3.608
Deformación cortante	< 0.020	0.016
Masa	< 1.25 kg	1.051 kg

- **Requisito 1: Conseguir una flexión estática máxima inferior a la descrita en la normativa**

  La tabla 33 muestra cada punto de la normativa que condiciona la rigidez estructural del alerón, presentando el límite impuesto en la normativa y el valor alcanzado en las simulaciones.

Table 4: Resultados de pruebas de rigidez según FIA Artículo 3 (desplazamientos máximos).

Prueba	**Componente**	**Límite FIA**	**Resultado**
3.15.9 parte 1	Desplazamiento alerón principal	3.0 mm	1.99 mm (66%)
3.15.9 parte 2	Desplazamiento alerón principal	2.5 mm	1.78 mm (71%)
3.15.10 parte 1	Desplazamiento DRS	5.0 mm	0.51 mm (10%)
3.15.10 parte 2	Desplazamiento DRS	6.0 mm	0.62 mm (10%)
3.15.11 parte 1	Desplazamiento alerón principal	2.0 mm	0.21 mm (11%)
3.15.11 parte 2	Desplazamiento alerón principal	2.0 mm	0.21 mm (10%)
3.15.11 parte 3	Desplazamiento alerón principal	2.0 mm	0.21 mm (11%)

Todos los casos cumplen los límites reglamentarios FIA 2025 con amplio margen de seguridad.

- **Requisito 2: Tener una flexión dinámica de ≤ 20 mm en el caso estudiado**

  La figura 109 presenta el resultado de la simulación FSI, mostrando la deformación máxima deseada de 20 mm en el caso dinámico estudiado.

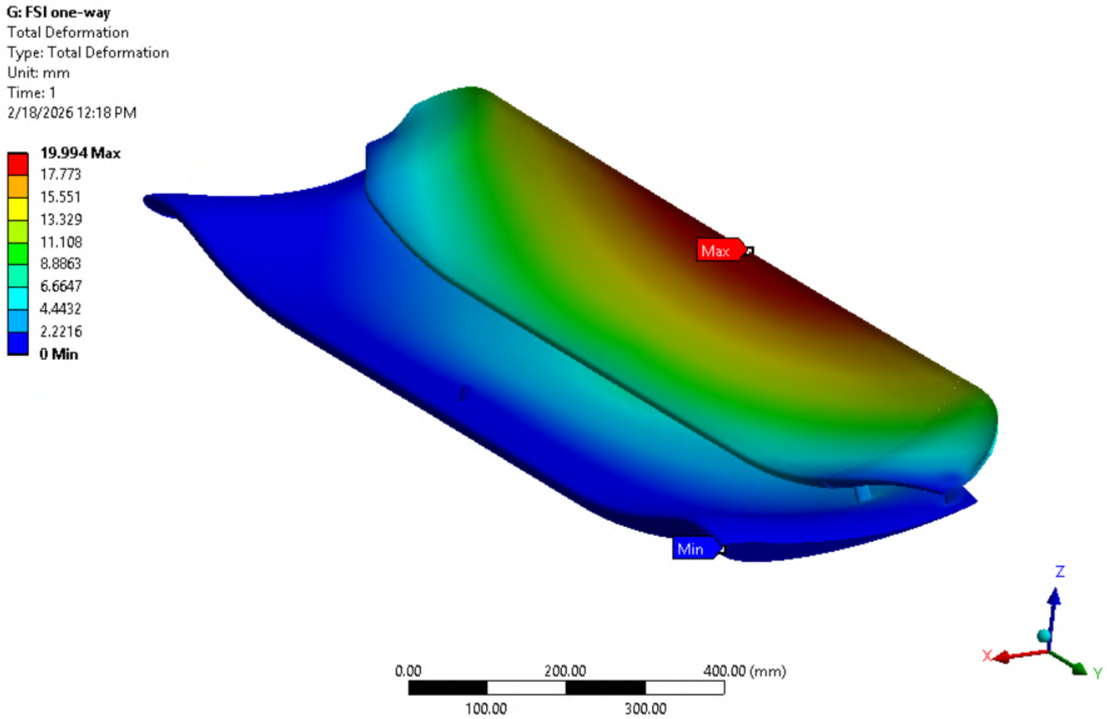

Figure 5: FSI: desplazamiento DRS 20 mm.

- **Requisito 3: Alcanzar una frecuencia natural del primer modo de vibración superior a 50 Hz para evitar resonancias $f_1 > 50$ Hz**

  La tabla 34 muestra las frecuencias naturales de cada modo.

Table 5: Frecuencias naturales.

Modo	Significado	f (Hz)
1	1ª flexión	64.872
2	1ª torsión	148.39
3	2ª flexión	189.38
4	1ª flexión transversal	236.79
5	2ª Torsión	247.47
6	3ª Flexión	286.02

- **Requisito 4: Conseguir un factor de seguridad** > 1.5 **según el criterio de Tsai-Wu em las uniones metal-composite**

  La figura 116 mustra el valor del coeficiente de seguridad según el criterio de Tsai-Wu en las uniones metal-composite, donde se muestra un valor promedio de 3.6, superior a la condición de 1.5.

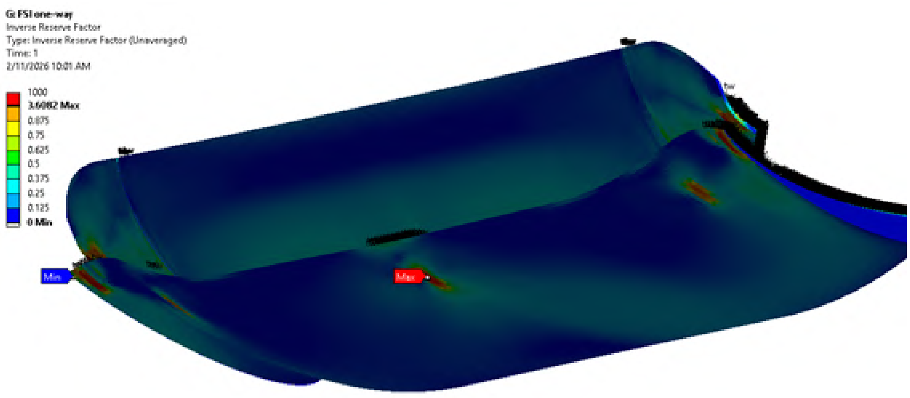

Figure 6: Coeficiente de seguridad según el criterio de Tsai-Wu

- **Requisito 5: Tener un valor de deformación cortante** < 0.020

  El valor máximo de la deformación cortante se presenta en la figura 117

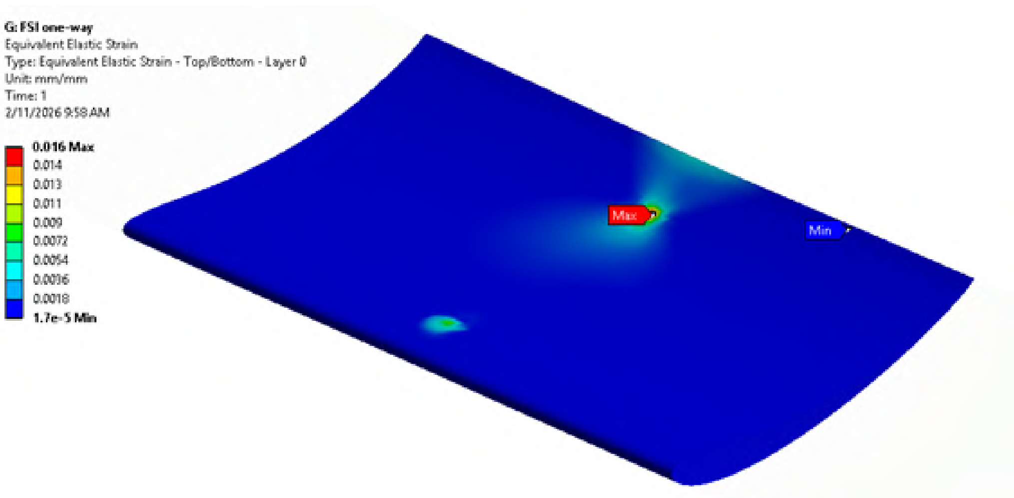

Figure 7: Deformación cortante equivalente

- **Requisito 6: Masa total inferior a 1.25 kg**

  La Tabla 35 muestra la distribución de masa de cada componente, alcanzando una masa total del alerón trasero de 1051 g, un 16% por debajo de la restricción de diseño de 1.25 kg.

Table 6: Resumen de masas por componente

Componente	**Subcomponente**	**Masa (g)**
DRS	Núcleo RH71	316.4
	Núcleo T700	320.9
ALERÓN PRINCIPAL	Núcleo RH71	660.7
	Núcleo T700	240.6
FLAP	Núcleo RH71	20.5
	Núcleo T700	26.2
TOTAL		**1051.4**

1.7 Conclusiones: Ganancias aerodinámicas

La tabla 36 presenta los resultados del análisis de la ganancia aerodinámica producida por la flexión controlada del alerón. En esta tabla se compara los resultados del analisis aerodinámico del alerón rigido sin deformar y del alerón deformado por el efecto de la carga aerodinámica.

Table 7: Comparación resultados aerodinámicos: alerón deformado vs. rígido.

Parámetro	**Deformado**	**Rígido**	**Variación (%)**
Fuerza de sustentación	6813 N	6821 N	-0.12%
Fuerza de resistencia	1613 N	1616 N	-0.19%
Relación sustentación/resistencia	4.224	4.221	+0.07%
Área de referencia	0.1562 m^2	0.1658 m^2	-5.79%
C_D (coef. resistencia)	1.75	1.65	+6.06%
C_L (coef. sustentación)	7.40	6.98	+6.02%

La longitud de la recta principal del circuito de Monza son 1120 m, donde con este diseño se obtendría la ganancia mostrada en la tabla 16

Table 8: Ganancias Monza

Métrica	Ganancia
Velocidad máxima	+11.7 km/h
Tiempo recta principal	−0.49 s

2 Summary

2.1 Introduction

This project optimizes the composite layup of a Formula 1 rear wing to achieve controlled deformation under aerodynamic loading. The design reduces drag on straights while maintaining downforce in corners.

Formula 1 circuits have distinct characteristics, and to achieve maximum performance, teams must adapt aerodynamic configurations for each race. High average speed circuits like Monza require low drag to reach top speed, while low-speed circuits like Monaco, with short straights where high speeds are not reached, need more downforce for better grip in corners. Teams change wing designs and adjust suspension to achieve the best possible lap time.

Structures made with composite laminates allow controlling stiffness by varying layup parameters such as the number of plies, fiber type, and orientation of each ply. This project studies how these parameters enable controlled flexing of the wing, optimizing the trade-off between drag and downforce through the proposed design of a Formula 1 rear wing that complies with the 2025 technical regulations defined by the Fédération Internationale de l'Automobile (FIA).

2.2 Methodology

The project consists of several analyses:

1. Material selection using Granta for supports, wing component cores, and fiber type
2. Reverse engineering of an F1 wing to obtain the geometry
3. CAD modeling of the wing
4. Computational fluid dynamics (CFD) analysis to evaluate aerodynamic performance and obtain the pressure map on the wing in the case study
5. Static structural analysis to verify compliance with regulations
6. Fluid-structure interaction (FSI) analysis to determine the value and manner of wing deformation due to aerodynamic loading
7. Modal frequency analysis to calculate natural frequencies
8. Multi-objective layup optimization to define the layup that optimizes design requirements

The objective is to capture the interaction between airflow-induced deformation and the wing to find the optimal layup that improves aerodynamic performance without compromising structural strength or regulatory compliance. The complete workflow is shown in Figure 8, where the work is divided into two stages. The first obtains a wing geometry and initial material and layup definition that complies with regulations. The second stage corresponds to layup optimization to achieve the defined design objectives.

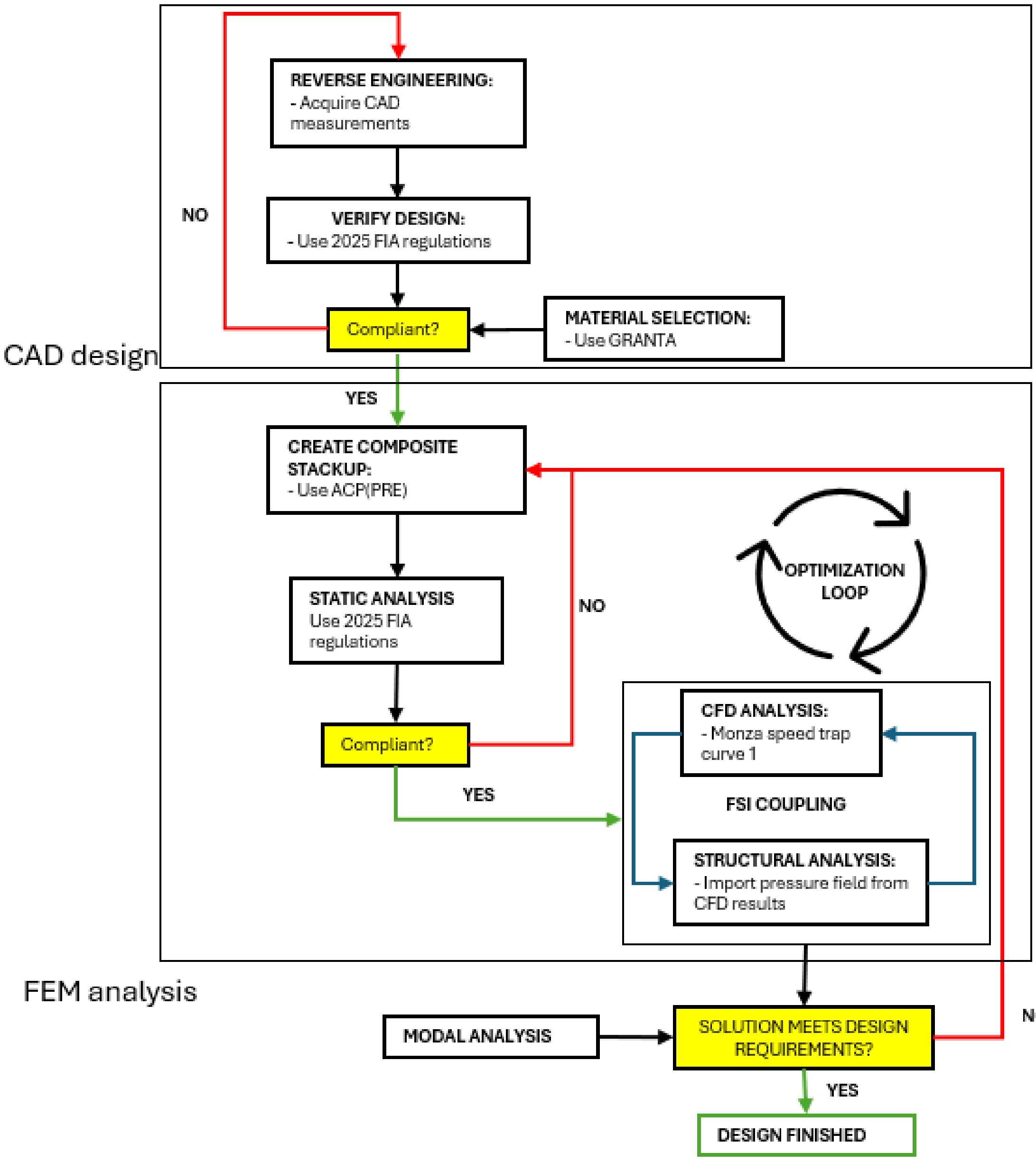

Figure 8: Project workflow

2.3 Model Description

Figure 9 shows the final CAD model of the wing, where the main wing is colored red, the DRS in blue, flaps in black, and supports in gray.

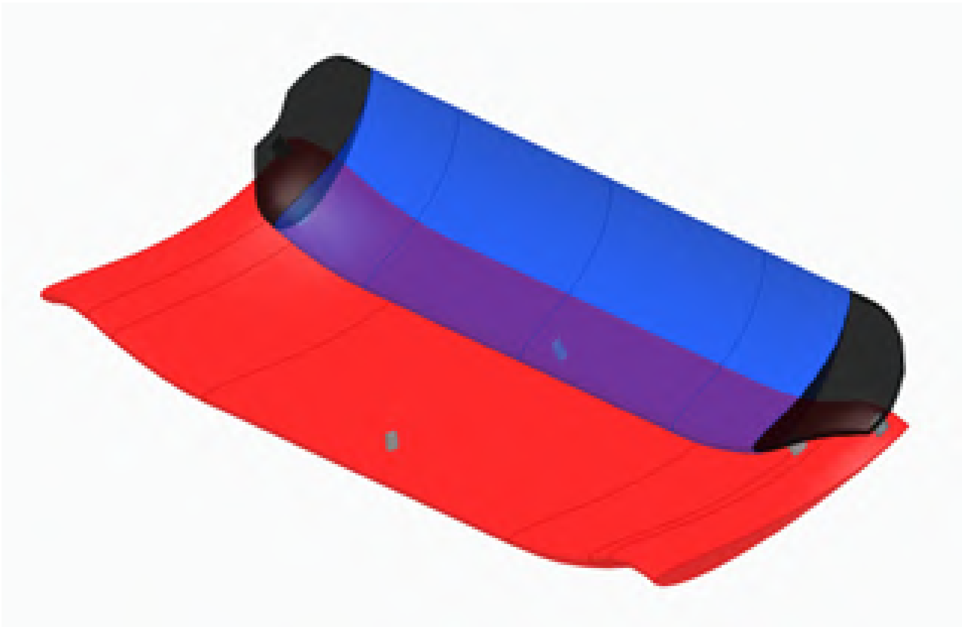

Figure 9: Final CAD model.

Twenty layups were analyzed. The first optimization stage consists of twelve layups, classified into four with 4 plies, four with 6 plies, and four with 8 plies, maintaining angular relationships between configurations. One configuration was selected to proceed to the next optimization stage, where 8 layups were studied.

2.4 Design Requirements

The requirements considered for the wing design are as follows:

1. **Load cases**:
   (a) Static structural simulation with loads from the 2025 FIA technical regulations.
   (b) Dynamic structural simulation at the maximum speed reached at the end of Monza's main straight.
2. **Structural objectives**:
   (a) Achieve maximum static deflection below the regulatory limit
   (b) Have 20 mm dynamic deflection in the studied case
   (c) Reach a first natural vibration mode frequency above 50 Hz to avoid resonances $f_1 > 50$ Hz

(d) Achieve a safety factor > 1.5 according to Tsai-Wu criterion in the metal-composite interface

(e) Have shear strain < 0.020

(f) Total mass < 1.25 kg with ply thickness ≤ 0.25 mm

2.5 Multi-Objective Optimization

The optimization considered the following objectives and conditions:

- **Objective 1:** Minimize mass by seeking the fewest CFRP plies
- **Objective 2:** Achieve 20 mm maximum dynamic DRS displacement
- **Constraint:** Minimum 4 plies to comply with FIA 2025 regulations
- **Variables:** Number of plies and angle of each ply

2.5.1 Optimization by Number of Plies

Table 29 compares the maximum deformation and mass of the 12 layups proposed in the first optimization stage.

Configuration	Deformation	Mass
4 plies		
1 [woven 0 ud 0,ud 45, ud 0]	22.92 mm	316.2 g
2 [woven 0, ud 0, ud 45, ud 0]	22.49 mm	316.2 g
3 [woven 0, ud 0, ud 90, ud 0]	17.95 mm	316.2 g
4 [woven 0, ud 0, ud 45, ud -45]	21.09 mm	316.2 g
6 plies		
5 [woven 0, ud 0, ud 45, ud 0, ud -45, ud 0]	19.98 mm	474.3 g
6 [woven 0, ud 0, ud 45, ud 0, ud 45, ud 0]	21.26 mm	474.3 g
7 [woven 0, ud 0, ud 0, ud 90, ud 0, ud 0]	17.61 mm	474.3 g
8 [woven 0, ud 0, ud 45, ud 90, ud 45, ud 0]	16.85 mm	474.3 g
8 plies		
9 [woven 0, ud 0, ud 45, ud 0, ud 0, ud 45, ud 0, woven 0]	17.96 mm	632.4 g
10 [woven 0, ud 45, ud 0, ud 45, ud 45, ud 0, ud 45, woven 0]	17.62 mm	632.4 g
11 [woven 0, ud 0, ud 45, ud 90, ud 90, ud 45, ud 0, woven 0]	13.53 mm	632.4 g
12 [woven 0, ud -45, ud 0, ud 45, ud 45, ud 0, ud -45, woven 0]	16.39 mm	632.4 g

Table 9: Maximum DRS deformation for each configuration

Figure 107 shows the trends for each configuration. Configuration C ($[woven0/ud0/ud90/ud0]_s$), shown in green, maintains better longitudinal stiffness with the smallest variation in deformation between 4 and 8 plies. To proceed to the second optimization phase, configuration C with 4 plies was selected due to its lower mass and maximum deformation close to the target value.

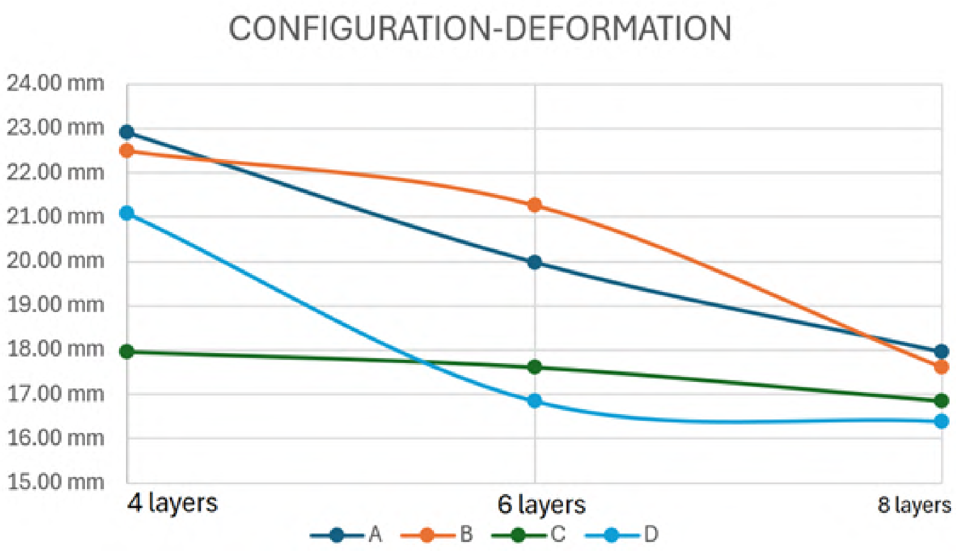

Figure 10: Deformation trend vs. number of plies

2.5.2 Angle Optimization

The angle θ was optimized in the 4-ply configuration C ($[0/0/\theta/0]_s$). The simulation results, shown in Figure 108, indicate the optimal value is $\theta \approx 67°$.

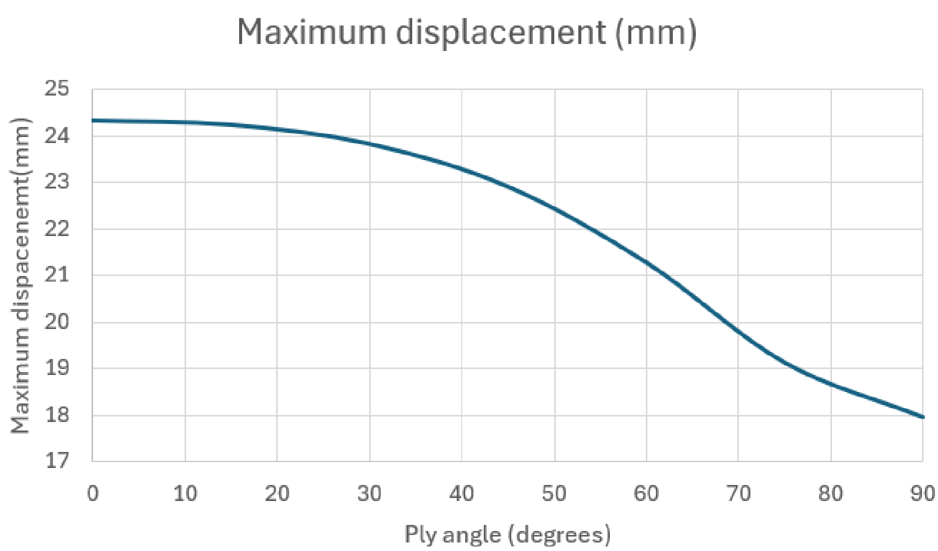

Figure 11: DRS displacement vs. angle θ

2.6 Results

Table 31 shows the final materials used in each component and the layup definition.

Table 10: Final optimized layups.

Component	Layup	Thickness
DRS	$[woven(0°)/ud(0°)/ud(67°)/ud(0°)]_s$	1.00 mm
Flap	$[woven(0°)/ud(0°)/ud(0°)]_s$	0.75 mm
Main wing	$[woven(0°)/ud(0°)/ud(0°)]_s$	0.75 mm
Core	Rohacell 71 foam	–
Supports	Aluminum 7055	–

Table 32 presents how each objective was met.

Table 11: Requirements compliance.

Requirement	Target	Achieved
Static deflection	< 4 mm	< 2 mm
Dynamic deflection	$= 20$ mm	20 mm
f_1	> 50 Hz	64.872 Hz
Safety factor	> 1.5	3.608
Shear strain	< 0.020	0.016
Mass	< 1.25 kg	1.051 kg

- **Requirement 1: Achieve maximum static deflection below regulatory limit**

  Table 33 shows each regulation point conditioning the wing's structural stiffness, presenting the regulatory limit and simulation results.

Table 12: Stiffness test results per FIA Article 3 (maximum displacements).

Test	**Component**	**FIA Limit**	**Result**
3.15.9 part 1	Main wing displacement	3.0 mm	1.99 mm (66%)
3.15.9 part 2	Main wing displacement	2.5 mm	1.78 mm (71%)
3.15.10 part 1	DRS displacement	5.0 mm	0.51 mm (10%)
3.15.10 part 2	DRS displacement	6.0 mm	0.62 mm (10%)
3.15.11 part 1	Main wing displacement	2.0 mm	0.21 mm (11%)
3.15.11 part 2	Main wing displacement	2.0 mm	0.21 mm (10%)
3.15.11 part 3	Main wing displacement	2.0 mm	0.21 mm (11%)

- **Requirement 2: Achieve ≤ 20 mm dynamic deflection in the studied case**

  Figure 109 presents the FSI simulation result, showing the desired maximum deformation of 20 mm in the studied dynamic case.

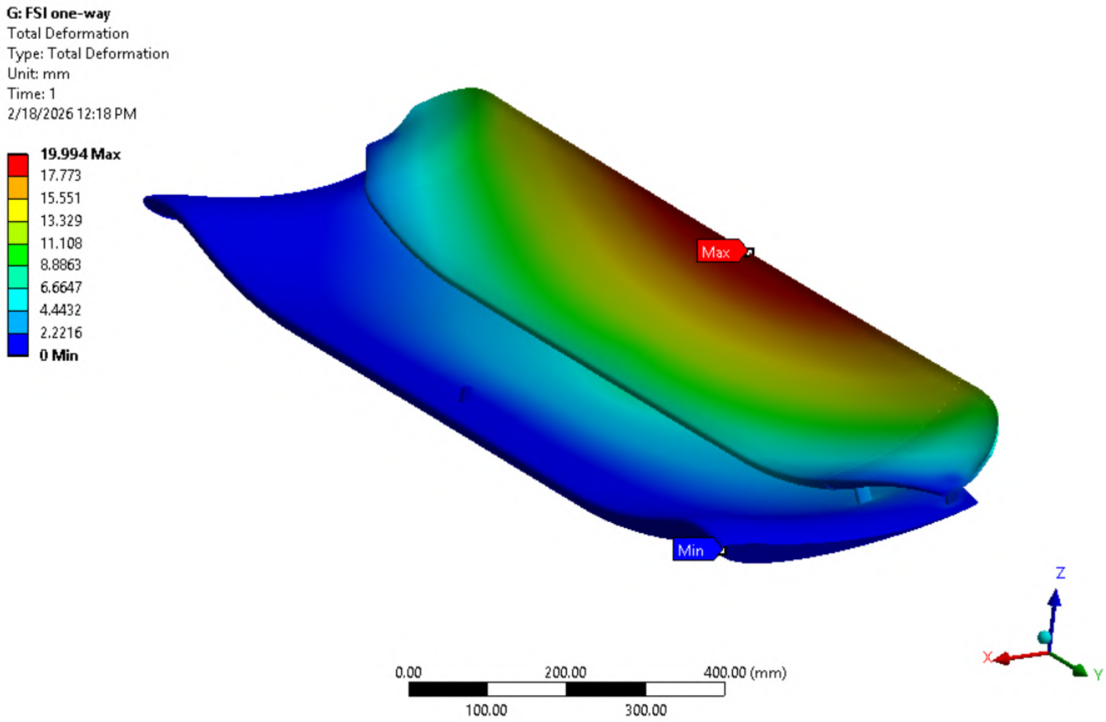

Figure 12: FSI: DRS displacement 20 mm.

- **Requirement 3: Reach first natural vibration mode frequency above 50 Hz to avoid resonances $f_1 > 50$ Hz**

  Table 34 shows the natural frequencies of each mode.

Table 13: Natural frequencies.

Mode	Description	f (Hz)
1	1st bending	64.872
2	1st torsion	148.39
3	2nd bending	189.38
4	1st transverse bending	236.79
5	2nd torsion	247.47
6	3rd bending	286.02

- **Requirement 4: Achieve safety factor** > 1.5 **per Tsai-Wu criterion in the metal-composite interface**

  Figure 116 shows the safety factor value according to the Tsai-Wu criterion. The result achieved is an average value of 3.6 in the metal-composite conection, which is higher to the 1.5 safety factor goal.

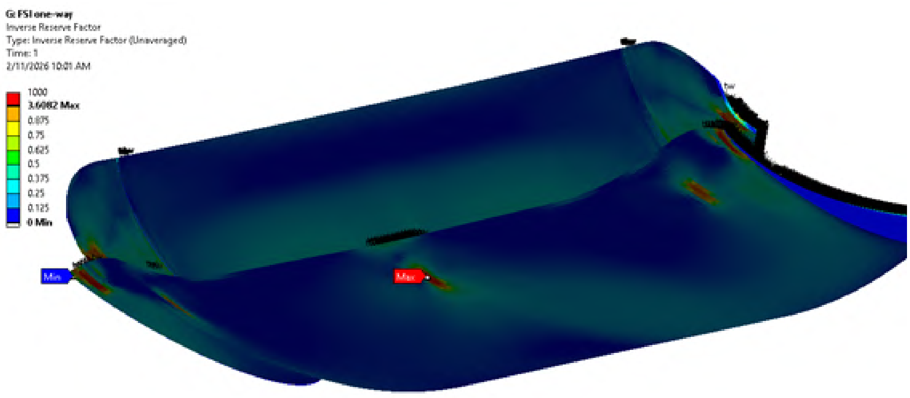

Figure 13: Safety factor per Tsai-Wu criterion

- **Requirement 5: Have shear strain** < 0.020

  The maximum shear strain value is presented in Figure 117.

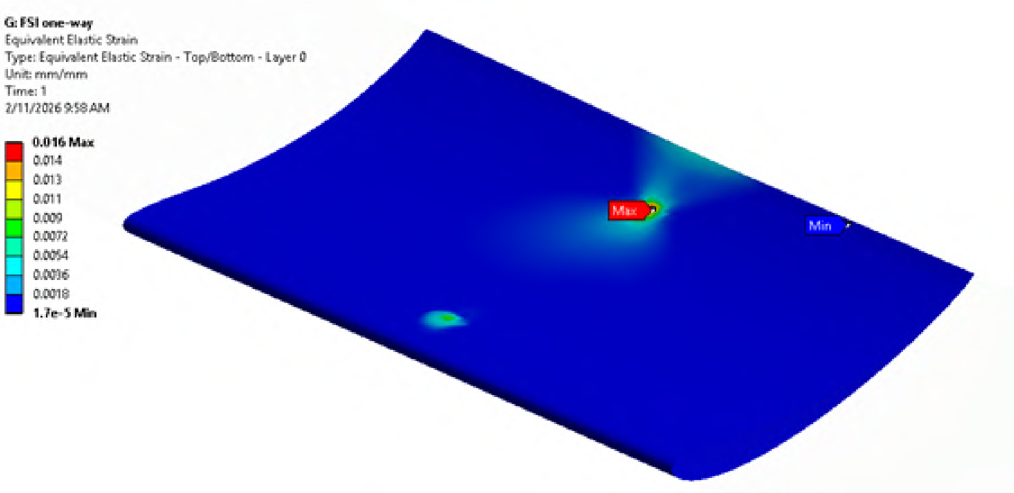

Figure 14: Equivalent shear strain

- **Requirement 6: Assembly weight below 1.25kg**

  Table 35 shows the mass distribution of each component, achieving a total rear wing mass of 1051 g, 16% below the 1.25 kg design constraint.

Table 14: Component weights summary

Component	**Subcomponent**	**Weight (g)**
DRS	Core RH71	316.4
	Core T700	320.9
MAIN WING	Core RH71	660.7
	Core T700	240.6
FLAP	Core RH71	20.5
	Core T700	26.2
TOTAL		**1051.4**

2.7 Conclusions: Aerodynamic Gains

Table 36 presents the aerodynamic gain results from controlled wing flexing. This table compares aerodynamic analysis results of the rigid undeformed wing and the deformed wing under aerodynamic loading.

Table 15: Aerodynamic results comparison: deformed vs. rigid wing.

Parameter	**Deformed**	**Rigid**	**Variation (%)**
Lift force	6813 N	6821 N	-0.12%
Drag force	1613 N	1616 N	-0.19%
Lift/drag ratio	4.224	4.221	+0.07%
Reference area	0.1562 m^2	0.1658 m^2	-5.79%
C_D (drag coefficient)	1.75	1.65	+6.06%
C_L (lift coefficient)	7.40	6.98	+6.02%

Monza's main straight is 1120 m long, where this design yields the gains shown in Table 16.

Table 16: Monza gains

Metric	Gain
Top speed	+11.7 km/h
Main straight time	−0.49 s

Contents

1 Resumen **1**
1.1 Introducción 1
1.2 Metodología 1
1.3 Descripción del modelo 3
1.4 Requisitos de diseño 3
1.5 Optimización multiobjetivo 4
1.5.1 Optimización por número de capas 4
1.5.2 Optimización de ángulos 5
1.6 Resultados 6
1.7 Conclusiones: Ganancias aerodinámicas 10

2 Summary **11**
2.1 Introduction 11
2.2 Methodology 11
2.3 Model Description 13
2.4 Design Requirements 13
2.5 Multi-Objective Optimization 14
2.5.1 Optimization by Number of Plies 14
2.5.2 Angle Optimization 15
2.6 Results 16
2.7 Conclusions: Aerodynamic Gains 20

3 State of the Art **29**
3.1 Introduction 29
3.2 Aerodynamic Forces on a Rear Wing 31
3.3 Equilibrium of forces 31
3.3.1 Lift (Downforce) 33
3.3.2 Drag 33
3.3.3 Lift-to-Drag Ratio 34
3.4 Composites in Advanced Engineering 34
3.4.1 Carbon Fibers 38
3.4.2 Other Polymeric Fibers 39
3.4.3 Laminate Optimization Techniques 39
3.4.4 Frequency Optimization 40
3.4.5 Buckling Optimization 40
3.4.6 Multi-Objective Optimization 40
3.4.7 Lamination Parameters 41
3.4.8 Bending Lamination Parameters 42
3.4.9 Extension Lamination Parameters 42
3.5 Aeroelastic Modeling 42
3.5.1 Aeroelasticity 42
3.5.2 Aeroelasticity in Motorsport 43
3.6 CFD–FEM Coupling: FSI 44

4 Methodology **46**
4.1 Project Gantt Chart . . . 48
4.2 Design requirements . . . 49
4.3 Resources . . . 50

5 Material Selection Analysis **51**
5.1 Core . . . 51
5.2 Metal Supports . . . 52
5.3 Composite Surface . . . 54

6 CAD design **56**
6.1 Reversed engineering . . . 59
6.2 Compliance with the FIA regulations . . . 61

7 FEM analysis **63**
7.1 Regulation . . . 63
7.2 ANSYS simulations . . . 67
7.3 Plybook iteration . . . 78

8 CFD analysis **81**
8.1 ANSYS implementation . . . 81
8.1.1 Geometry . . . 82
8.1.2 Meshing . . . 83
8.1.3 Setup . . . 87
8.1.4 Solution . . . 89
8.1.5 Results . . . 90

9 Fluid–Structure Interaction (FSI) **95**
9.1 Fluid–Structure Interaction Implementation in Ansys Workbench . . 97
9.1.1 Structural Model . . . 97
9.1.2 Load Transfer . . . 97
9.1.3 Results . . . 98

10 Modal Response Analysis **99**
10.1 Modal response analysis workflow . . . 99
10.2 Modal response analysis results . . . 100

11 Optimization **104**
11.1 Objective 1: minimize total mass . . . 105
11.1.1 Maximum deformation per number of plyes . . . 106
11.1.2 Maximum deformation per configuration . . . 107
11.2 Multiobjective Optimization . . . 110
11.2.1 First Iteration: Coarse Screening . . . 110
11.3 Final Plybook . . . 111

12 Results and Conclusions **112**
12.1 CFD Comparison between Deformed and Non-Deformed Rear Wing . 117
12.2 Performance advantage . . . 118

13 Conclusions **120**
13.1 Key Achievements 120
13.2 Performance Quantification 120
13.3 Technical Contributions 120
13.4 Future Research Directions 121

14 Anexo A: Materials datasheets **125**

15 Anexo B: Granta Analysis export results **138**

16 Anexo C: SDG alignment **164**

List of Figures

1 Flujo de trabajo del proyecto 2
2 Modelo CAD final. 3
3 Tendencia deformación vs. número de capas 5
4 Desplazamiento DRS vs. ángulo θ 5
5 FSI: desplazamiento DRS 20 mm. 7
6 Coeficiente de seguridad según el criterio de Tsai-Wu 8
7 Deformación cortante equivalente 8
8 Project workflow 12
9 Final CAD model. 13
10 Deformation trend vs. number of plies 15
11 DRS displacement vs. angle θ 15
12 FSI: DRS displacement 20 mm. 17
13 Safety factor per Tsai-Wu criterion 18
14 Equivalent shear strain 18
15 Track layouts: Monza (left) and Monaco (right) 29
16 Rear wing configurations: Monaco (left, high downforce) vs. Monza (right, low drag). 30
17 Equilibrium of lateral forces 31
18 Lateral force-vertical force (left), Lateral force-slip angle 32
19 3D representation of vertical force, lateral force and slip angle 32
20 Forces in a Formula 1 car 33
21 Comparison of mechanical properties of metallic and composite materials 35
22 Composite components in the Boeing 787 35
23 Composite components in the Airbus A380 36
24 Schematic of a composite sandwich structure with honeycomb core [SAVA08]. 37
25 Composite gearbox used in Formula 1 37
26 Composite chassis 38
27 Collar's triangle of forces. 43
28 McLaren rear wing deflection at high speed. 44
29 FSI approaches 44
30 Workflow 47
31 Monza circuit layout 49
32 Young's modulus vs. specific density for foam materials. 52
33 Shear strength vs. specific density for foam materials. 52
34 Young's modulus vs. specific density for metallic materials. 53
35 Shear strength vs. specific strength for metallic materials. 53
36 Specific strength vs. specific density for composite materials. 54
37 Specific stiffness vs. specific density for composite materials. 54
38 Rear wing design for different teams in the 2025 season 56
39 Mclaren rear wing comparison between mexico and brazil during the 2025 races 57
40 Rear wing components 58

41 Formula 1 rear wing with the drs open and the drs closed. 59
42 Mclaren MCL 39 59
43 Measurements from the Mclaren MCL 39 rear view 60
44 Measurements from the Mclaren MCL 39 lateral view 60
45 CAD model designed 61
46 Detail view of the CAD model designed 61
47 CAD design inside reference volume 62
48 article 3.15.9 part 1 on ANSYS 63
49 article 3.15.9 part 2 on ANSYS 64
50 Article 3.15.10 part 1 on ANSYS 65
51 Article 3.15.10 part 2 on ANSYS 65
52 article 3.15.11 part 1 on ANSYS 66
53 article 3.15.11 part 2 on ANSYS 66
54 article 3.15.11 part 3 on ANSYS 67
55 ANSYS workbench workflow 67
56 ACP block 68
57 ROHACELL used as core 69
58 Woven (left) vs unidirectional (right) 70
59 Model in SPACECLAIM 70
60 ACP mesh 71
61 ACP mesh detail 1 71
62 ACP mesh detail 2 72
63 ACP variable thickness display 73
64 ACP normal direction verification 73
65 ACP normal direction verification detail view 74
66 Mechanical block 74
67 Mechanical meshing 75
68 Mechanical meshing detail 76
69 Structural block 76
70 Fixed sections 77
71 Fixed sections detail view 77
72 Monza layout 81
73 CFX block 82
74 CFD model in Spaceclaim 83
75 CFD mesh 84
76 CFD mesh control: Skewness 85
77 Skewness values 85
78 CFD setup 88
79 CFD residuals 89
80 CFD forces results 90
81 Pressure distribution view 1 91
82 Pressure distribution view 2 91
83 Streamline view 1 92
84 Streamline front view 93
85 Streamline plane Y=0 view 1 93
86 Streamline plane Y=0 view 2 94

87 ANSYS workflow 95
88 One way (left) vs two way (right) 96
89 FSI block 97
90 Mapped pressure distribution from CFX to structural surfaces 98
91 FSI results 98
92 Modal analysis workflow integrating ACP composite definitions with Mechanical modal solver. 99
93 Response mode 1 101
94 Response mode 2 101
95 Response mode 3 102
96 Response mode 4 102
97 Response mode 5 103
98 Response mode 6 103
99 Optimization conections 104
100 Maximum deformation: 4-ply configurations. 106
101 Maximum deformation: 6-ply configurations. 106
102 Maximum deformation: 8-ply configurations. 106
103 Configuration A: Deformation vs. ply count. 107
104 Configuration B: Deformation vs. ply count. 107
105 Configuration C: Deformation vs. ply count. 108
106 Configuration D: Deformation vs. ply count. 108
107 Deformation trends across configurations and thicknesses. 109
108 Maximum DRS displacement vs. ply angle θ (1st iteration). 110
109 FSI: DRS displacement 20 mm. 113
110 Mode 1: Fundamental bending (64.872 Hz). 114
111 Mode 2: 1st torsion (148.39 Hz). 114
112 Mode 3: 2nd bending (189.38 Hz). 114
113 Mode 4: 1st chordwise bending. 115
114 Mode 5: 2nd torsion. 115
115 Mode 6: 3rd bending. 115
116 Safety factor per Tsai-Wu criterion 116
117 Equivalent shear strain 116
118 Longitudinal streamlines: non-deformed (left) vs. deformed (right), 2D view. 117
119 Longitudinal streamlines: non-deformed (left) vs. deformed (right), 3D view. 118

List of Tables

1 Deformación máxima del DRS en cada configuración 4
2 Laminados finales optimizados. 6
3 Cumplimiento de requisitos. 6
4 Resultados de pruebas de rigidez según FIA Artículo 3 (desplazamientos máximos). 6
5 Frecuencias naturales. 7
6 Resumen de masas por componente 9
7 Comparación resultados aerodinámicos: alerón deformado vs. rígido. . 10
8 Ganancias Monza 10
9 Maximum DRS deformation for each configuration 14
10 Final optimized layups. 16
11 Requirements compliance. 16
12 Stiffness test results per FIA Article 3 (maximum displacements). . . 16
13 Natural frequencies. 17
14 Component weights summary 19
15 Aerodynamic results comparison: deformed vs. rigid wing. 20
16 Monza gains 20
17 Final optimized layups. 55
18 Final optimized layups. 68
19 Weight of each surface 78
20 Weight of the Rohacell core 78
21 Maximum allowable displacement 79
22 Main wing layup 79
23 DRS layup 79
24 Flap layup 79
25 Maximum displacement margin comparison in mm 80
26 Mesh convergence study 86
27 Grid Convergence Index (GCI) results 87
28 Natural frequencies. 100
29 Maximum DRS deformation for each configuration 105
30 Final optimized plybook for DRS rear wing assembly. 111
31 Final optimized layups. 112
32 Design requirements compliance summary. 112
33 Stiffness test results per FIA Article 3 (maximum displacements). . . 112
34 Natural frequencies. 113
35 Component weights summary 117
36 Aerodynamic results comparison: deformed vs. rigid wing. 118
37 Aeroelastic deformation performance gains 119

List of Symbols and Abbreviations

CFRP Carbon Fiber Reinforced Polymer

CAD Computer-Aided Design

CFD Computational Fluid Dynamics

DRS Drag Reduction System

FEM Finite Element Method

FIA Fédération Internationale de l'Automobile

F1 Formula 1

FSI Fluid-Structure Interaction

RH Rohacell (foam core material)

ud unidirectional

3 State of the Art

3.1 Introduction

This study investigates the aeroelastic tailoring of advanced composite materials, extensively used in motorsport for their exceptional specific strength and stiffness. The research focuses on optimizing a Formula 1 rear wing laminate layup to achieve targeted aeroelastic deformation under aerodynamic loading while maintaining regulatory compliance.

Composite wings enable precise control of stiffness distribution through strategic ply orientation and stacking sequence design. By engineering the laminate layup, it becomes possible to achieve passive aeroelastic flexing that simultaneously maximizes cornering downforce while minimizing straight line drag penalties.

Aeroelastic behavior is characterized through coupled *Fluid–Structure Interaction (FSI)* simulations, integrating Computational Fluid Dynamics (CFD) with Finite Element Analysis (FEA). This methodology captures the mutual dependence between aerodynamic forces and structural response, essential behavior that traditional decoupled analyses cannot accurately predict, in which the rear wing is deformed under aerodynamic loading. This project focuses on exploiting composite laminate technology and aeroelastic tailoring to optimize Formula 1 wing design, addressing the complex interplay between aerodynamic loads, structural flexibility, and vehicle performance.

The 2025 Formula 1 calendar comprises 25 races, each hosted on a unique circuit. Some, such as Monza in Italy or Baku in Azerbaijan, feature long straights combined with high-speed corners, while others, such as Monaco or the Hungaroring in Hungary, consist predominantly of short straights and low-speed turns. For each circuit, cars must be specifically configured to maximize performance, because a high-drag, high-downforce setup will get a bad result in a high speed circuit. Figure 15 presents the track layouts of Monza (left) and Monaco (right).

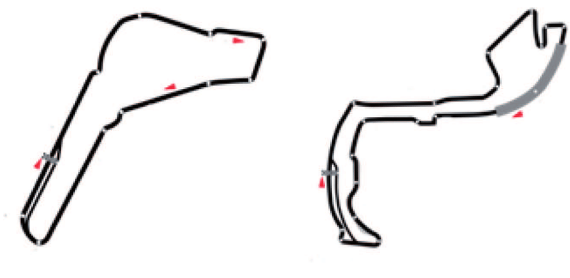

Figure 15: Track layouts: Monza (left) and Monaco (right)

Circuits with long straights and high-speed corners generally demand low drag and moderate downforce to achieve maximum top speed, whereas layouts dominated by slow corners and short straights require high downforce to optimize cornering. To achieve the best trade-off, teams adjust both aerodynamic components and suspension systems to minimize lap times. While high downforce improves tire grip and allows higher cornering speeds without loss of traction, it also increases drag, thereby reducing straight-line velocity.

Figure 16 illustrates how rear-wing configurations vary between circuits for teams like Ferrari, Red Bull and Mclaren between the races of Monaco and Monza. At Monaco, shown in the left side, where the layout consists almost entirely of low-speed corners and short straights, teams adopt maximum-downforce setups to improve cornering grip. This is reflected in the average lap speed, with the fastest lap of the 2024 Monaco Grand Prix, set by Charles Leclerc, averaging 189.5 km/h. In contrast, Monza, characterized by long straights and high-speed chicanes, is the most common low-drag circuit. Here, teams prioritize drag reduction over cornering grip, as demonstrated by Max Verstappen's fastest lap in the 2024 Monza Grand Prix, averaging 264.6 km/h. It can be seen how the front area surface from the wing is increased when the design aims to increase downforce.

Figure 16: Rear wing configurations: Monaco (left, high downforce) vs. Monza (right, low drag).

3.2 Aerodynamic Forces on a Rear Wing

One of the main challenges in Formula 1 aerodynamic design is achieving the optimal balance between downforce and drag. As noted by Savage [SAVA08], a Formula 1 car is driven at the limit, where the longitudinal force is almost sufficient to overcome the cornering force, meaning the car is always on the verge of spinning out of control.

3.3 Equilibrium of forces

Figure 17 illustrates lateral force equilibrium during cornering (top view, anti-clockwise turn) of a two-wheel model. The inertial (centrifugal) force $F_y = m \cdot a_y$ acts outward at the center of mass G, tending to push the vehicle beyond the desired trajectory. Tyre *cornering forces* F_{yF} (front) and F_{yR} (rear), generated through *slip angle* α, provide the counteracting centripetal force to maintain steady-state turning radius R:

$$\sum F_y = F_{yF} + F_{yR} - m \cdot \frac{V^2}{R} = 0$$

The tyres thus balance inertial loading while suspension geometry distributes vertical load transfer between inner/outer wheels.

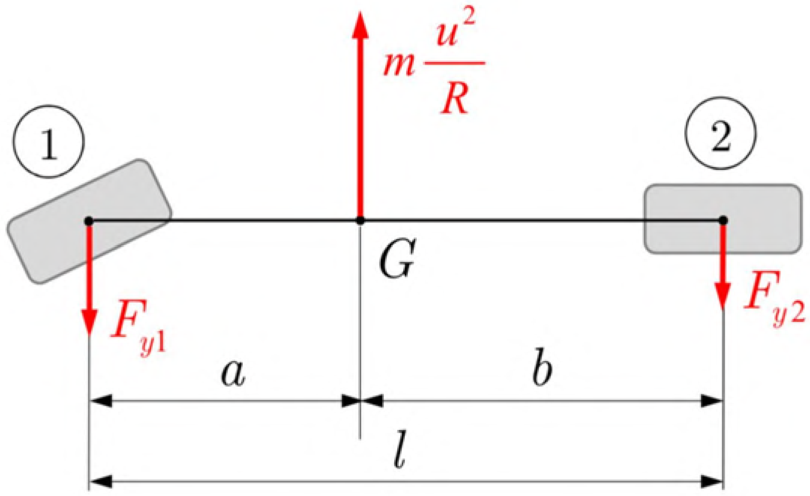

Figure 17: Equilibrium of lateral forces

Figures 17 and 18 demonstrate the tyre force limitations governing cornering performance. As vehicle speed increases, required tyre *cornering force* F_y grows proportionally to centripetal acceleration ($F_y = m \cdot V^2/R$). However, F_y exhibits *load sensitivity*: maximum lateral force increases sublinearly with vertical load F_z due to decreasing friction coefficient $\mu_y = F_y/F_z$.

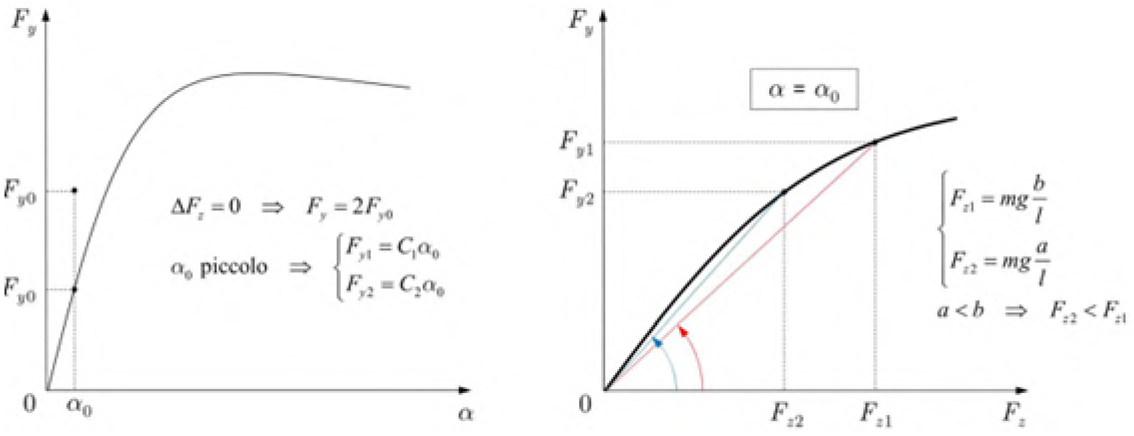

Figure 18: Lateral force-vertical force (left), Lateral force-slip angle

Figure 19 shows that higher F_z shifts the *slip angle* α peak rightward while increasing peak F_y, but at diminishing returns. During lateral load transfer, total axle cornering force decreases despite constant total F_z, creating a grip deficit. Figure 18 shows a 3D representation of the vertical force, lateral force and slip angle dependency.

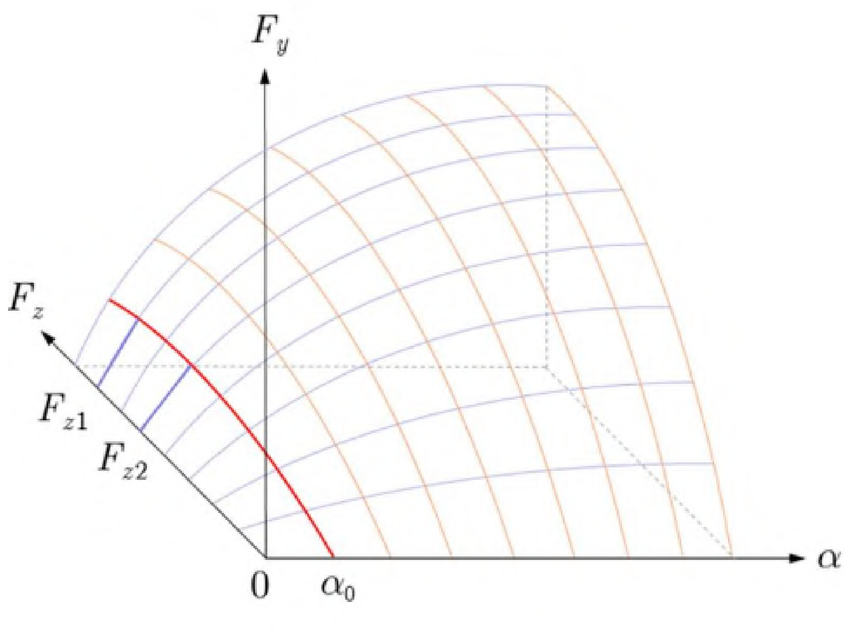

Figure 19: 3D representation of vertical force, lateral force and slip angle

Rear wing *downforce* directly addresses this limitation by augmenting F_z across all four tyres, enabling higher sustainable F_y and thus faster cornering speeds. The aeroelastic design optimizes this F_z increase while respecting FIA deflection limits.

The rear wing of a Formula 1 car generates aerodynamic forces that significantly influence stability, downforce, and overall performance. Primarily, it produces *lift*, which has the same value but opposite direction of the downforce and *drag*, with their balance optimized for specific speed regimes. Figure 20 shows the equilibrium of forces of a formula 1 car, in which the drag force goes against the power force and the downforce acts against the grip force of the tyres.

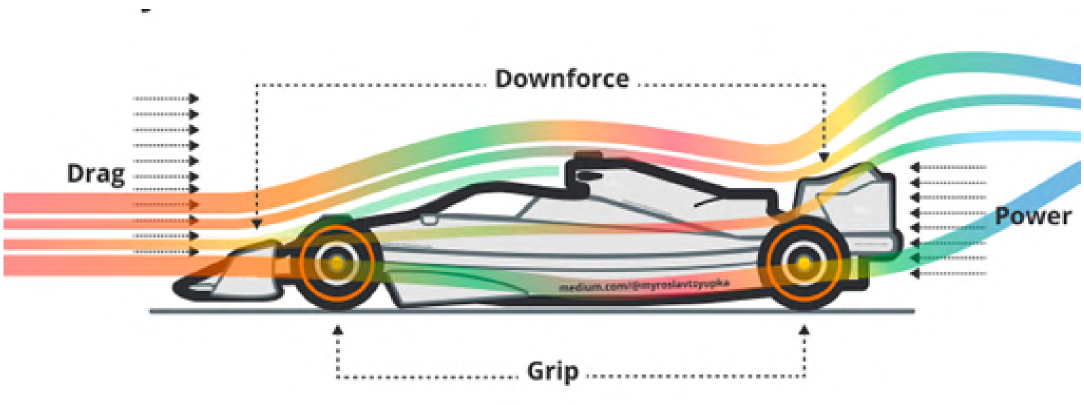

Figure 20: Forces in a Formula 1 car

3.3.1 Lift (Downforce)

Downforce is a critical aerodynamic force that enhances vehicle grip by increasing normal load on tires, thereby enabling higher cornering speeds without slip. In Formula 1, rear wings generate up to 40 % of total downforce, producing from 800 to 1500 kg at 320 km/h via 3-4 elements. The lift force L acts perpendicular to the incoming airflow and is given by:

$$L = \frac{1}{2}\rho v^2 C_L A,$$

where ρ is air density, v is vehicle speed, C_L is the lift coefficient (negative for downforce), and A is the wing's reference area. A rear wing with a positive angle of attack relative to the airflow creates negative lift, also called downforce, pressing the rear tires onto the track for better traction during cornering.

3.3.2 Drag

Drag force represents the primary aerodynamic penalty of rear wing downforce generation, acting parallel to the freestream airflow and directly opposing propulsive thrust. In Formula 1, rear wings contribute 30–50% of total vehicle drag, creating a fundamental performance trade-off: increased downforce enhances cornering grip but reduces straight-line acceleration and top speed. Drag force D is defined as:

$$D = \frac{1}{2}\rho v^2 C_D A.$$

Wings inherently increase drag due to their shape and angle, but modern designs, like multi-element airfoils use vortex generators or endplates to mitigate induced drag while maximizing C_L/C_D ratio.

3.3.3 Lift-to-Drag Ratio

Performance is quantified by the aerodynamic efficiency:

$$\epsilon = \frac{C_L}{C_D}.$$

Typical rear wings achieve $\epsilon > 2$ at high speeds ($v > 50$ m/s), trading some drag for substantial downforce, common values of this coeficients are $C_L \approx -2.0$, $C_D \approx 0.8$.

3.4 Composites in Advanced Engineering

Composite materials are hybrid systems created by combining two or more distinct constituents in order to exploit the advantageous properties of each component. For a material to be classified as a composite, the constituents must be present in significant proportions, typically exceeding 5% by weight. In contrast, alloys are not considered composites, since their multiphase microstructures result from solidification or heat treatment processes rather than the deliberate combination of separate materials [SAVA08].

At the microscopic scale, composites consist of at least two chemically distinct phases separated by an interface, which plays a critical role in determining the overall mechanical performance. The continuous phase, referred to as the *matrix*, is typically ceramic, metallic, or polymeric. In motorsport and aerospace applications, polymeric matrices dominate, especially thermosetting resins such as epoxy, which provide excellent adhesion, high stiffness, and good thermal stability. The matrix binds the reinforcement together, maintaining fibre alignment along the primary stress directions. It transfers externally applied loads to the fibres, enabling the composite to withstand tensile, compressive, flexural, and shear stresses. In addition, the matrix isolates the fibres from one another so that they act as discrete load-bearing elements.

The second phase, known as the *reinforcement*, is generally stiffer, stronger, and harder than the matrix. Its inclusion enhances the properties of the overall system, providing high specific stiffness and strength, along with the ability to engineer tailored anisotropic mechanical behavior. Common reinforcements include carbon fibres, which are dominant in Formula 1 for their superior strength-to-weight ratio; glass fibres, valued for their lower cost and good impact resistance; and aramid fibres, such as Kevlar, which are employed for their toughness and damage tolerance. These combined characteristics make composites a cornerstone of modern structural engineering, offering performance levels unattainable with conventional monolithic materials [SAVA08].

Figure 21 shows a comparison of the mechanical properties of metallic and composite materials.

Material	Density (g cm^3)	Tensile strength, σ (MPa)	Tensile modulus, E (GPa)	Specific strength (σ/ρ)	Specific modulus
Steel	7.8	1300	200	167	26
Aluminium	2.81	350	73	124	26
Titanium	4	900	108	204	25
Magnesium	1.8	270	45	150	25
E glass	2.10	1100	75	524	21.5
Aramid	1.32	1400	45	1060	57
IM carbon	1.51	2500	151	1656	100
HM carbon	1.54	1550	212	1006	138

Figure 21: Comparison of mechanical properties of metallic and composite materials

Composites are widely employed in aerospace engineering for both primary and secondary structures, including rocket motor casings, engine nacelles, and flap track panels. Their adoption has increased dramatically in modern aircraft: the Boeing 777, launched in 2000, incorporated approximately 11% composites, while the Boeing 787, introduced in 2007, employs nearly 50%, corresponding to around 32,000 kg of advanced laminates. Such extensive use of composites directly improves fuel efficiency and overall performance [RANA16]. Figure 22 illustrates the composite components in the Boeing 787.

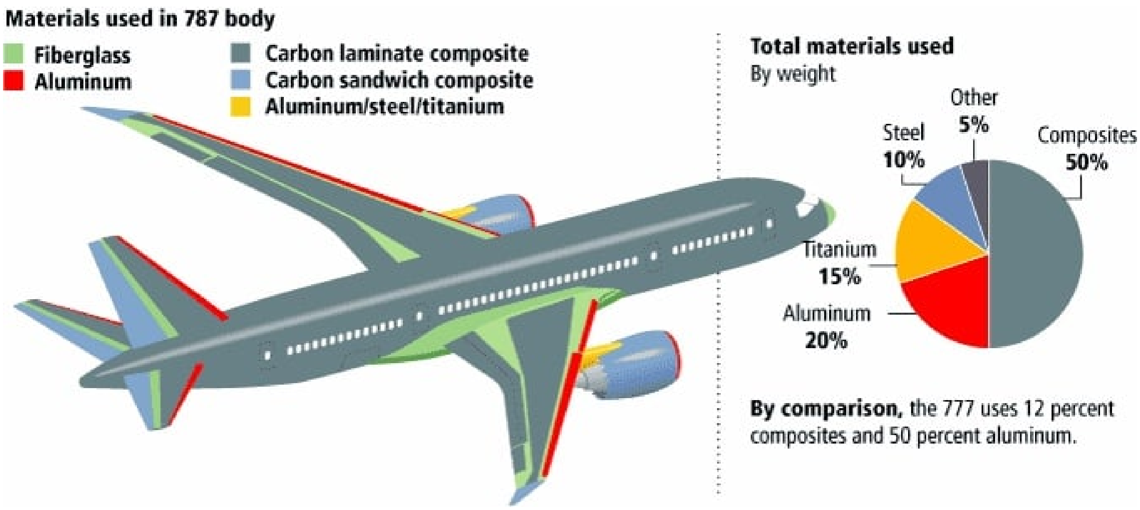

Figure 22: Composite components in the Boeing 787

A similar trend is observed in the Airbus A380, which entered production in 2005 and remained in service until 2021. Figure 23 highlights the composite structures integrated into the A380, reflecting the industry-wide move toward lightweight, high-performance materials in large commercial aircraft.

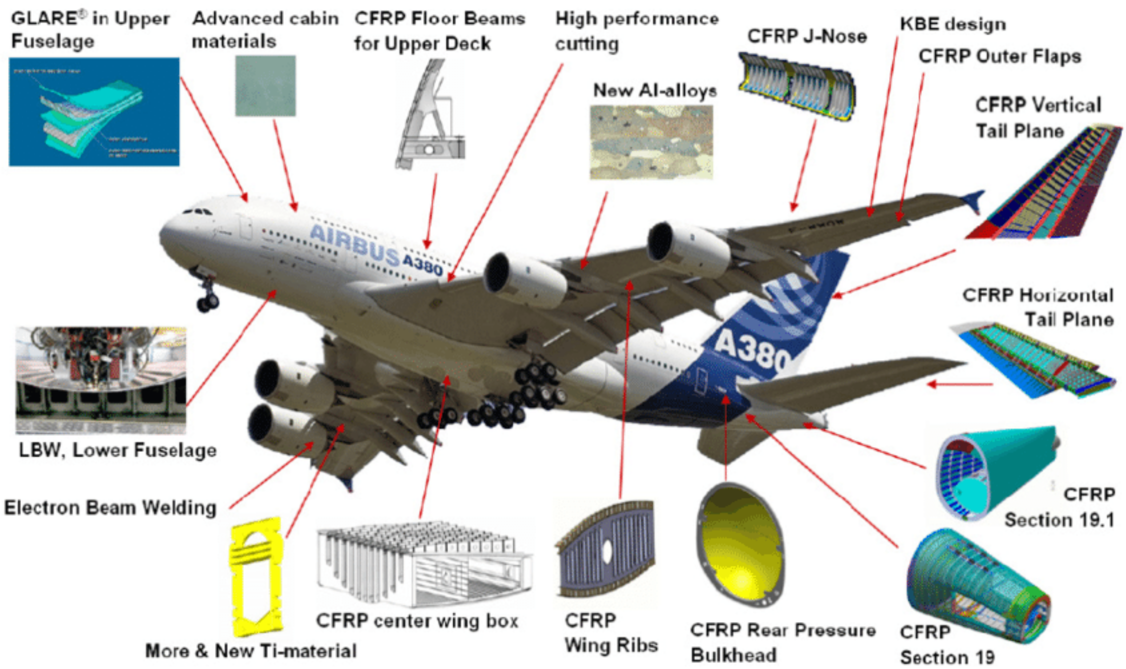

Figure 23: Composite components in the Airbus A380

Composite structures are carefully designed with precise fiber placement and orientation, supported by a minimum amount of polymer matrix. This is commonly achieved through *prepregs*, intermediate products consisting of reinforcement impregnated with resin and ready for use in the lay-up process. Structural components are fabricated by stacking multiple prepreg plies and curing them under controlled temperature and pressure.

Sandwich structures, consisting of composite skins bonded to lightweight honeycomb cores, are frequently employed to further increase stiffness-to-weight ratios. most common are nomex , which is aramid paper impregnated with resin and aluminum honeycomb.Figure 24 shows a schematic view of a composite sandwich structure with honeycomb core.

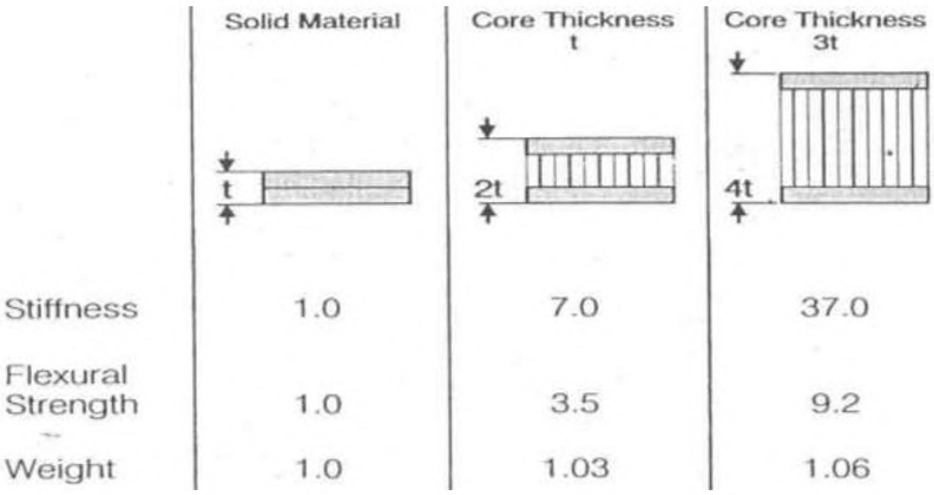

Figure 24: Schematic of a composite sandwich structure with honeycomb core [SAVA08].

According to Savage [SAVA08], the introduction of fiber-reinforced composite chassis in Formula 1 marked one of the most significant engineering breakthroughs in motorsport, enabling lighter, faster, and safer racing cars. Today, composites are widely employed in top categories such as Formula 1 and GT racing, particularly in chassis structures, wings, and other aerodynamic components. Figure 25 illustrates a composite Formula 1 gearbox, while Figure 26 shows a composite chassis, also referred to as the monocoque or survival cell.

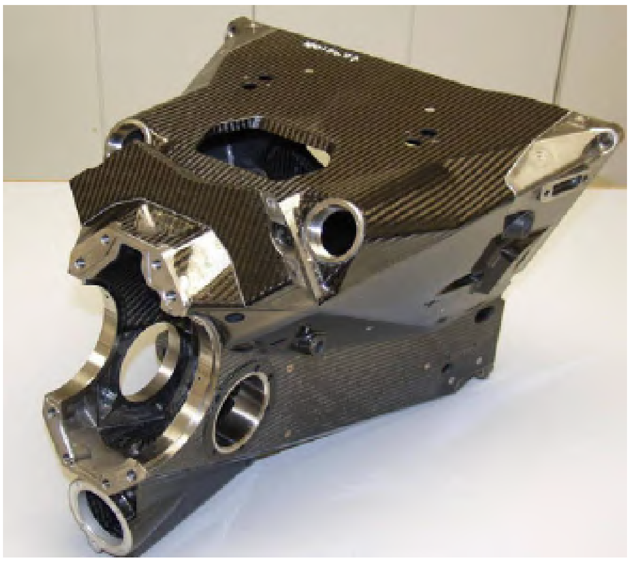

Figure 25: Composite gearbox used in Formula 1

Figure 26: Composite chassis

The anisotropic nature of composites allows engineers to tailor stiffness in specific directions, improving both handling and aerodynamic efficiency. In addition, composites deliver excellent crashworthiness and fatigue resistance, making them essential in the design of modern high-performance racing vehicles.

3.4.1 Carbon Fibers

Carbon fibers are predominantly produced from three precursor feedstocks: rayon, polyacrylonitrile (PAN), and pitch. PAN-based fibers dominate the market due to their favorable processing and mechanical properties. By oxidising and pyrolysing a highly drawn textile fibre such as polyacrylonitrile (PAN), preventing it from shrinking in the early stages of the degradation process, and subsequently hot-stretching it, it is possible to convert it to a carbon filament with an elastic modulus that approaches the value we would predict from a consideration of the crystal structure of graphite, although the final strength is usually well below the theoretical strength of the carbon-carbon chain [MIRA01]. In general, the modulus of carbon fibers increases with higher heat treatment temperature (HTT) and the application of tension during processing, as their morphology evolves toward a more graphitic crystalline structure. However, strength tends to peak around 1500 °C (with $E_{11} \approx 270$ GPa) and then decline due to surface flaws, known as “Reynolds’ sharp cracks,” originating from the spinning process of precursor fibers [SOUT05]. Prior to sale, fibres are usually surface-treated by chemical or electrolytic oxidation methods in order to improve the quality of adhesion between the fibre and the matrix in a composite. To mitigate this, advanced manufacturing techniques such as air-spinning have been introduced, producing smoother surfaces and leading to a new class of “ultra-high strength” fibers [CHOU80].

Commercially, PAN-based carbon fibers are grouped by modulus levels determined by their HTT regime. Standard modulus fibers (1000–1400 °C), such as Toray T300 and Hexcel AS4, are widely used across aerospace, marine, and automotive applications, though in Formula 1 they are mostly reserved for non-structural bodywork or tooling [SOUT05]. Intermediate modulus fibers (1400–1800 °C), such as Toray T800 and Hexcel IM7, are now extensively used in F1 structural components due to their high strength-to-weight ratio. High and ultra-high modulus fibers (above 1800 °C), including Toray M46J and M55, offer exceptional stiffness but suffer from brittleness and high cost, making them suitable mainly for niche applications such as satellites and sports equipment [MIRA01].

A subcategory of ultra-high strength fibers, such as Hexcel IM9 and Toray T1000, combine high modulus with improved strain-to-failure (>2%), providing superior impact resistance and damage tolerance. These properties are especially relevant to driver safety in motorsport, as they allow the survival cell and chassis to sustain impact damage while maintaining structural integrity [CLYN19].

3.4.2 Other Polymeric Fibers

Besides carbon, three other polymeric fibers are relevant in motorsport composites: aramids (Kevlar), Zylon, and highly oriented polyethylene filaments. Kevlar, characterized by high toughness and low density, has been traditionally used for its excellent impact and abrasion resistance. Although largely replaced by tougher epoxies and advanced carbon fibers in most F1 applications, Kevlar remains mandatory in front wing endplates and other forward aerodynamic appendages, primarily to reduce the risk of tire damage from sharp composite fragments. Nomex, another aramid, is widely used as honeycomb core material [CLYN19].

Zylon, composed of rigid-rod chain molecules of PBO, offers exceptional tensile strength and is used as an epoxy/Zylon appliqué armor panel in the monocoque survival cell. Its role is to prevent penetration and protect drivers from sharp-force impacts. Polyethylene-based fibers, though less common, have also been explored for impact-critical applications [MIRA01].

3.4.3 Laminate Optimization Techniques

Laminate optimization is a key aspect of composite design, involving the selection of ply orientations, stacking sequences, and materials to achieve target mechanical performance. Traditional approaches rely on established design rules and simplified analytical models derived from experience. Modern methods, as discussed by Albazzan et al. [ALBA19], extend these principles by optimizing nonconventional laminates using lamination parameters.

Current optimization strategies address the challenges of nonlinear, non-convex, and high-dimensional problems that involve both discrete and continuous variables. Computational techniques such as topology optimization, genetic algorithms, and gradient-based methods systematically explore the design space to identify optimal ply orientations, thicknesses, and material combinations. These approaches enable precise tailoring of stiffness and flexibility to satisfy specific performance requirements [ALBA19].

Optimized laminates must balance multiple competing objectives, including stiffness, weight, and aeroelastic behavior. In aerospace and motorsport, minimizing weight is critical for efficiency and performance, while maintaining structural integrity and controlling aeroelastic deflections ensures safety and aerodynamic effectiveness. Typical optimization goals include maximizing fundamental frequency, buckling load, and effective stiffness [PEET17]. Increasing fundamental frequency reduces dynamic response amplitudes for excitations below this frequency, while higher buckling loads prevent premature failure under compression. Maximizing stiffness generally corresponds to minimizing peak strain, thereby enhancing structural reliability. Often, multiple objectives are considered simultaneously, requiring designers to evaluate trade-offs between dynamic and load-bearing performance [ALBA19].

Lamination parameters provide a compact representation of laminate stiffness matrices. These parameters allow designers to maximize dynamic performance (fundamental frequency) or load-carrying capability (buckling load and equivalent stiffness) and explore trade-offs using Pareto-optimal solutions. Studies often compute natural frequencies and critical buckling coefficients using finite element frameworks, linking lamination parameters to nodal stiffness matrices to enable repeated analyses across different laminate configurations [SHAR17,KAME07].

3.4.4 Frequency Optimization

Maximizing the fundamental frequency is a common objective in the dynamic optimization of composite structures, as higher frequencies indicate greater stiffness and improved vibration resistance [KAME07]. Bert [BERT77] proposed a closed-form solution for simply supported thin rectangular laminated plates using classical lamination theory, demonstrating that careful selection of fiber orientations in symmetric and balanced laminates can maximize the fundamental frequency.

3.4.5 Buckling Optimization

Determining the buckling load of a composite plate under in-plane compression is crucial, as buckling can lead to premature failure [LIND10]. Lamination parameters are often used as design variables instead of directly specifying ply number, orientations, and thicknesses. This approach provides a more compact design representation and reduces the likelihood of converging to local optima [KAM93,KARA11]. Lamination parameter-based optimization has proven effective for enhancing load-carrying capacity, particularly in aerospace and motorsport applications where structural reliability and weight reduction are both essential.

3.4.6 Multi-Objective Optimization

In multi-objective optimization, different performance metrics can lead to distinct optimal laminate designs. Researchers have therefore explored frameworks that maximize both dynamic performance and load-carrying capacity. Kam and Chang [KAM93] performed a layerwise optimization study to maximize both the fundamental frequency and buckling load of thick laminated plates, using the finite element method combined with a weighted-sum approach. Their work analyzed the effects of aspect ratio, side-to-thickness ratio, and number of layers on symmetric and antisymmetric laminates under uniaxial compression[FUKU93].

While Pareto-optimal solutions have been widely studied, lamination parameters have not always been used for parametrization [FUKU93], limiting the ability to represent stiffness properties continuously and compactly. A multi-objective framework using lamination parameters allows simultaneous optimization of fundamental frequency, buckling load, and effective stiffness, producing Pareto-optimal solutions across multiple panel aspect ratios and loading conditions. Miki's lamination diagram [MIKI85] provides a visualization of the feasible design space for such multi-objective problems.

3.4.7 Lamination Parameters

The lamination parameters, introduced by Tsai and Hahn [TSAI18] and further studied by Miki [MIKI93] and Fukunaga [FUKU93], provide a compact means to represent laminate configurations. Instead of defining ply numbers, thicknesses, and fiber orientations directly, lamination parameters describe the overall in-plane and bending stiffness properties of a laminate.

Liu and Toropov [LIU13] formulated an optimization problem minimizing weight while constraining buckling, strength, and lamination parameter feasibility. In their wing-box benchmark study, lamination parameters enabled efficient representation of in-plane and flexural stiffness, simplifying the optimization compared to classical approaches where ply angles and layer thicknesses are directly specified.

Another advantage of using lamination parameters is the convexity of the design space, which significantly reduces the risk of local optima, except in cases such as forced vibration response [SERH19]. In practical applications, symmetric laminates are often assumed, and thin skins of torsion boxes can be modeled as membranes.

Using classical laminate theory [JONE18], which neglects transverse shear and normal stresses, Lamination parameters summarize the effect of ply orientation, the number of plies at each angle, and the overall bending and twisting stiffness of the laminate. While lamination parameters are continuous variables, actual stacking sequences are discrete, typically consisting of integer numbers of plies at standard angles such as $0°$, $\pm 45°$, and $90°$. Lamination parameters provide a compact representation of the stiffness contribution of a composite laminate. For a laminate with N plies, the bending lamination parameters are defined as: For a symmetric laminate, the coupling between bending and extension is zero (B=0), so only extension and bending stiffness are considered

3.4.8 Bending Lamination Parameters

$$\xi_1^D = \frac{1}{N} \sum_{k=1}^{N} \cos(2\theta_k), \tag{1}$$

$$\xi_2^D = \frac{1}{N} \sum_{k=1}^{N} \cos(4\theta_k), \tag{2}$$

$$\xi_3^D = \frac{1}{N} \sum_{k=1}^{N} \sin(2\theta_k) \cdot \sin(4\theta_k), \tag{3}$$

where θ_k is the orientation angle of the k-th ply relative to the reference axis.

3.4.9 Extension Lamination Parameters

Similarly, the extension (in-plane) lamination parameters are defined as:

$$\xi_1^A = \frac{1}{N} \sum_{k=1}^{N} \cos(2\theta_k), \tag{4}$$

$$\xi_2^A = \frac{1}{N} \sum_{k=1}^{N} \cos(4\theta_k), \tag{5}$$

$$\xi_3^A = \frac{1}{N} \sum_{k=1}^{N} \sin(2\theta_k) \cdot \sin(4\theta_k). \tag{6}$$

3.5 Aeroelastic Modeling

3.5.1 Aeroelasticity

Carbon fiber, the primary material in Formula 1 chassis and aerodynamic surfaces, exhibits inherent anisotropy. This property allows high stiffness along one direction while maintaining flexibility in another. By carefully tailoring the orientation of each carbon ply, engineers can design components that respond predictably under complex multi-directional loads.

FIA load tests for wing flexibility are typically static, applying vertical forces at specified points. Teams are aware of these loading vectors and design components to comply. However, during real-world racing, aerodynamic forces act in multiple directions, particularly longitudinally, causing structural deformations that alter airflow, a phenomenon known as *aeroelasticity*. This is a central challenge in advanced aerodynamic design. Aeroelastic phenomena can be visualized using Collar's triangle of forces (Figure 27), illustrating the interaction between aerodynamic, elastic, and inertial forces. Dynamic effects are typically represented in the inner domain of the triangle.

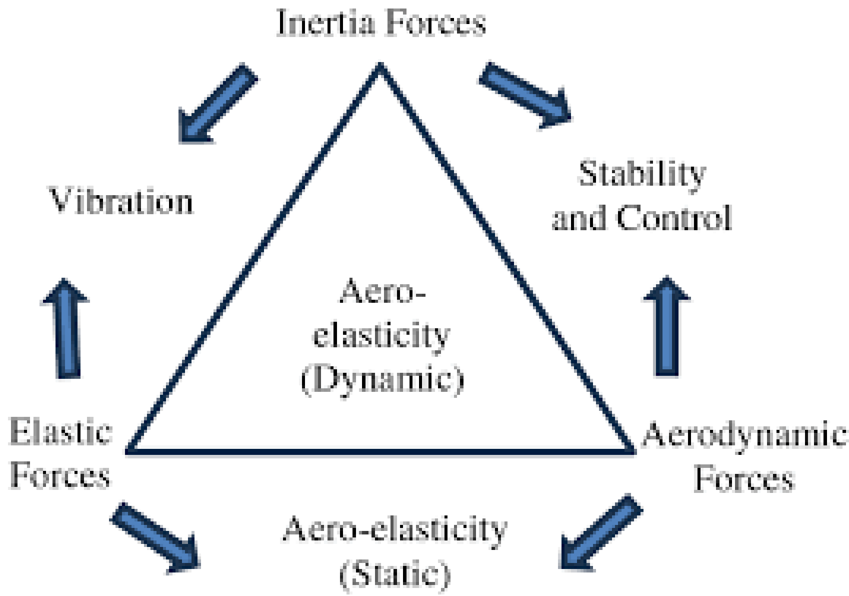

Figure 27: Collar's triangle of forces.

Static aeroelasticity involves quasi-steady, unidirectional structural deflections under aerodynamic loading without inertial effects. **Dynamic aeroelasticity**, in contrast, entails oscillatory structural responses that can result in instabilities such as flutter, buffeting, or divergence.

Although originally studied in aerospace, aeroelastic principles are applied in civil and transportation engineering to improve structural stability, ride comfort, and aerodynamic performance.

3.5.2 Aeroelasticity in Motorsport

Aeroelasticity has been a critical focus in Formula 1, particularly in the 2024–2025 season. Teams have historically exploited controlled wing flexibility to optimize downforce and reduce drag. In response, the FIA implemented stringent static load tests to prevent excessive deflection and maintain aerodynamic fairness.

Some teams, like McLaren, have leveraged passive aeroelastic effects to gain performance advantages. For instance, during the 2024 Baku Grand Prix, onboard footage from Oscar Piastri's car revealed rear wing deflection at high speed. This behavior acted as a "mini-DRS," reducing drag on straights without activating the official DRS system (Figure 28). As aerodynamic loads decrease during braking or cornering, the wing returns to its original configuration, restoring maximum downforce.

Figure 28: McLaren rear wing deflection at high speed.

Even at high speeds, no aerodynamic surface is perfectly rigid. F1 wings must pass FIA static tests while remaining flexible enough under racing loads to optimize performance.

3.6 CFD–FEM Coupling: FSI

FSI approaches are generally classified as *monolithic* (strongly coupled) or *partitioned* (loosely coupled). Monolithic methods solve fluid and structural dynamics simultaneously within a single system, improving accuracy for tightly coupled problems but requiring specialized solvers [MICH04]. Partitioned methods, in contrast, solve fluid, structural, and mesh movement equations sequentially. The fluid solver first applies boundary conditions from extrapolated structural displacements, followed by the structural solver using updated fluid tractions. This approach leverages existing validated solvers, though convergence may be challenging for light structures in dense or incompressible fluids. Figure 29 shows the two methods mentioned.

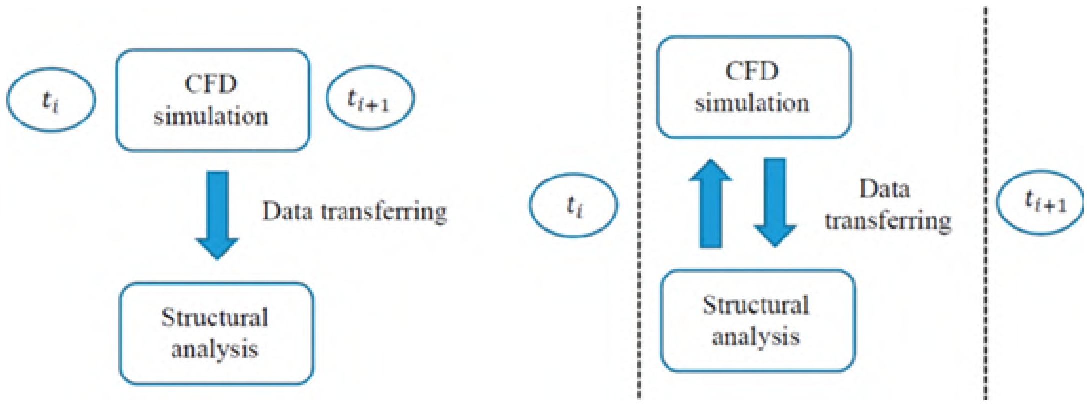

Figure 29: FSI approaches

In this study, the partitioned strategy is implemented using ANSYS *System Coupling*, which integrates multiple solvers into a coordinated multidisciplinary analysis. Coupling variables, data transfer regions, iteration schemes, and convergence criteria are defined to ensure robust interaction between solvers. Once the system converges, results from both individual and coupled analyses are evaluated to assess aeroelastic behavior [BANG22].

4 Methodology

This chapter describes the workflow of the project, the project Gantt chart, the design requirements defined and the resources used. The methodology of this project is based on a multidisciplinary approach that integrates:

1. Material selection using Granta for supports, wing component cores, and fiber type
2. Reverse engineering of an F1 wing to obtain the geometry
3. CAD modeling of the wing
4. Computational fluid dynamics (CFD) analysis to evaluate aerodynamic performance and obtain the pressure map on the wing in the case study
5. Static structural analysis to verify compliance with regulations
6. Fluid-structure interaction (FSI) analysis to determine the value and manner of wing deformation due to aerodynamic loading
7. Modal frequency analysis to calculate natural frequencies
8. Multi-objective layup optimization to define the layup that optimizes design requirements

The objective is to capture the fluid–structure interaction (FSI) phenomena and to identify optimal lamination strategies that improve aerodynamic efficiency without compromising structural integrity or regulatory compliance. This integrated workflow allows for rapid iteration between aerodynamic performance prediction and structural sizing, ensuring that aero loads are accurately transferred to the FEA model. The workflow of the project is shown in figure 30.

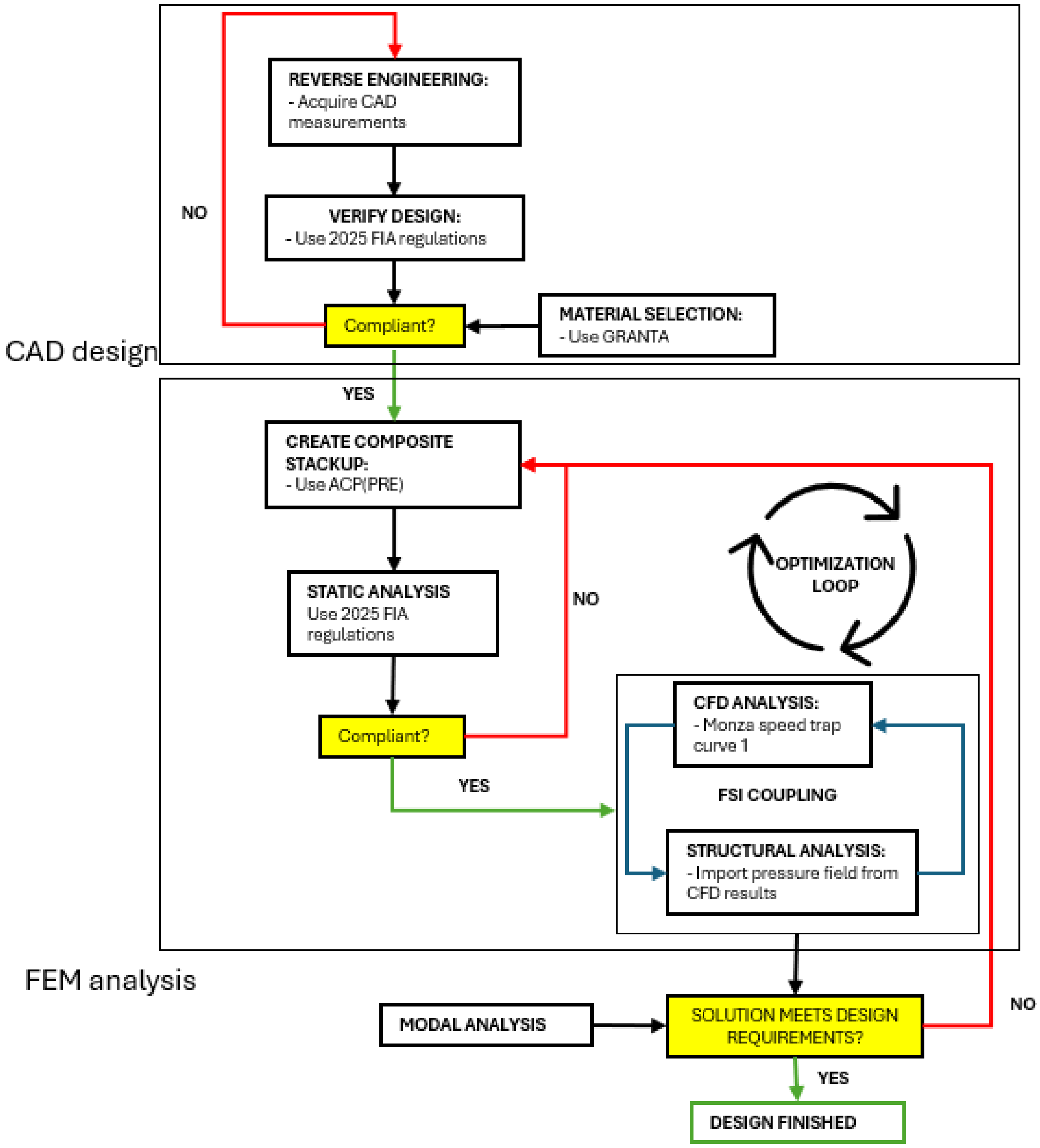

Figure 30: Workflow

4.1 Project Gantt Chart

This section presents the Gantt charts proposed for the project. The first phase, scheduled between September and November, focuses on acquiring the necessary knowledge and preparing the simulation framework. The second phase, running from December to February, is dedicated to the development of the coupled simulations and the optimization process, followed by a comprehensive analysis of the results.

Project Gantt Chart (September 2025– November 2025)

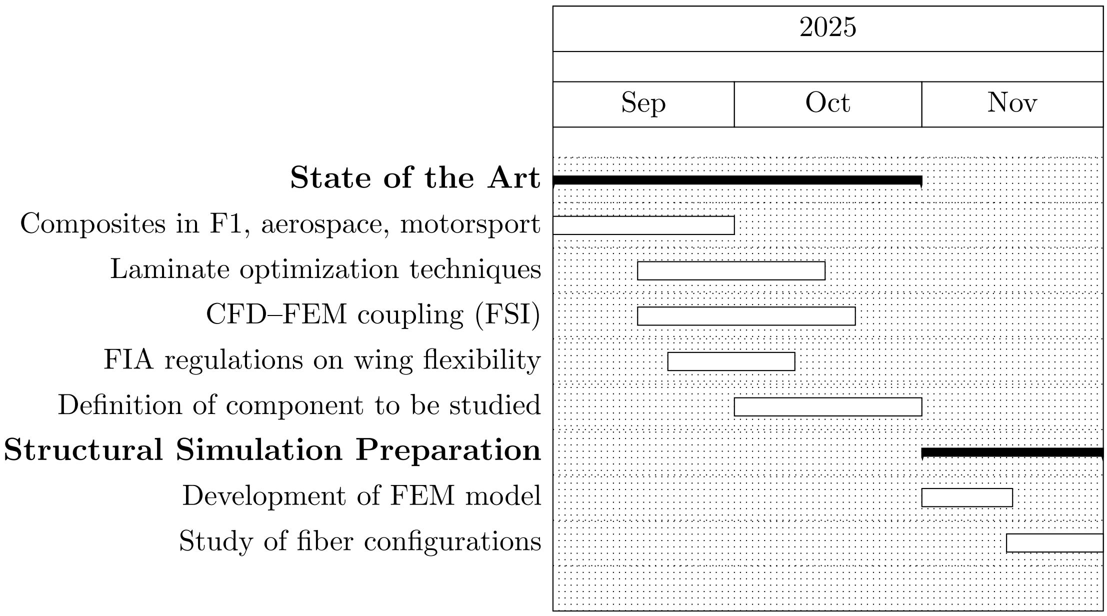

Project Gantt Chart (December 2025 – February 2026)

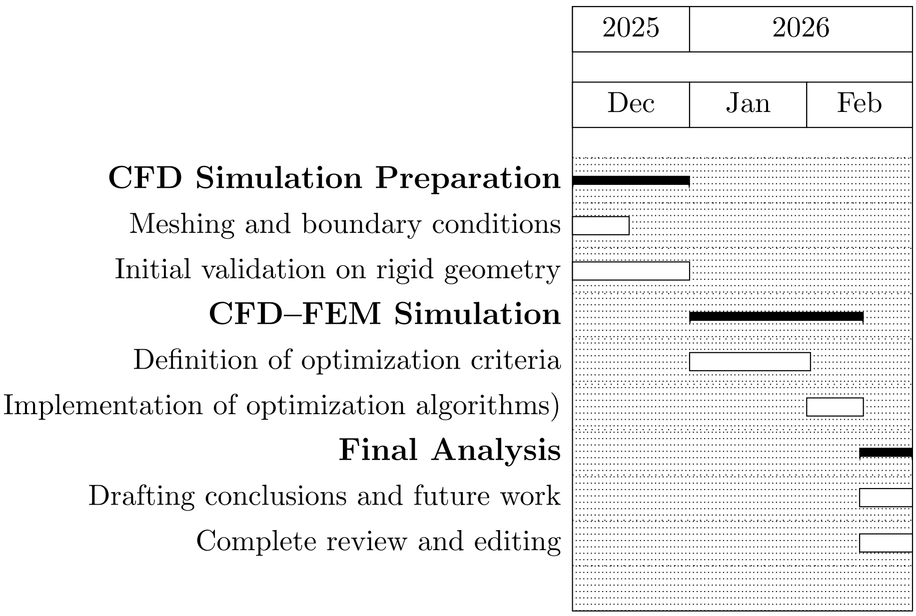

4.2 Design requirements

The rear wing design is governed by aerodynamic, structural, and regulatory constraints. The primary objective is to ensure sufficient stiffness and strength under aerodynamic loads while minimizing mass. To this end, the following design requirements are defined:

1. **Load cases:** Different load cases are analyzed:
   (a) The design must be compliant with the FIA 2025 season technical regulations, to validate this, the proposed design is subjected to the loading cases defined in the technical regulations.
   (b) To optimize the performance of the rear wing the loading case chosen corresponds to the end of the main straight of the Monza circuit, just before Turn 1, at the speed trap. The layout of the Monza circuit is shown in figure 31.

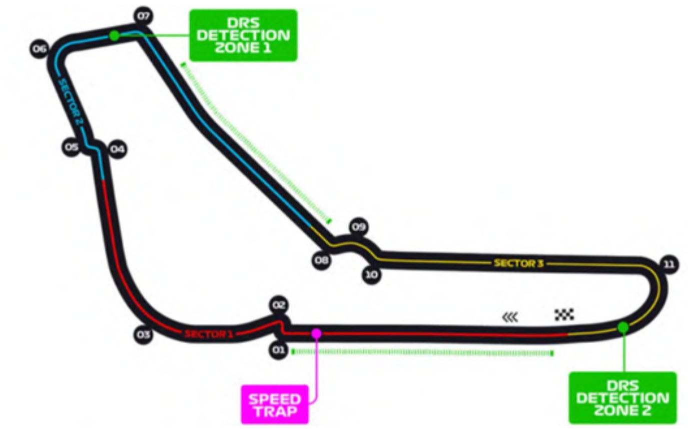

Figure 31: Monza circuit layout

2. **Structural targets:**
   The structural targets chosen for this design are the following:
   (a) Maximum static deflection according to regulation.
   (b) Maximum dynamic deflection of 18 mm.
   (c) first natural frequency $f_1 > 50$ Hz to avoid resonance with excitation frequencies from tyre hop (20-40 Hz), suspension modes (10-30 Hz), engine vibrations, kerb strikes, or aerodynamic buffeting, preventing fatigue cracks, loss of aero stability, or structural failure.
   (d) safety factor $SF > 1.5$, computed using composite failure criteria such as Tsai–Wu to account for material property scatter, manufacturing defects, load estimation errors, impact damage, and environmental degradation.
   (e) shear strain $\gamma_{\max} < 0.020$, keeping the laminate in an elastic, low damage regime, improving fatigue life and mantaining torsional rigity so the wing does not twist excssively under load.

3. **Performance constraints:** The total wing mass must remain below 1.25 kg, and each ply thickness is limited to 0.25 mm to ensure manufacturability and weight compliance.

4. **Regulatory compliance:** Verify compliance with FIA 2025 Technical Regulations, particularly Article 3.10 (Bodywork flexibility) and Appendix 3 (Load testing procedures).

4.3 Resources

The software packages that will be used in this project are ANSYS (for Computational Fluid Dynamics, Finite Element Analysis, CFD analysis, modal analysis and the ANSYS Composite PrepPost module), Solid Edge 2024 for the CAD design and Granta Edupack for the material selection.

5 Material Selection Analysis

This chapter presents the methodology and results of the material selection process for the main structural components: the core, the composite surface, and the metallic supports and attachments. The analysis was carried out using *ANSYS Granta EduPack*, a specialized software tool that facilitates systematic material selection based on mechanical, physical, and economic criteria. This tool enables cross-comparison among thousands of materials by visualizing performance indices and ensuring that the chosen materials meet both design and functional requirements.

The "Aerospace Engineering" materials database was employed, as materials used in Formula 1 applications often share similar properties with those used in the aerospace industry, such as high specific stiffness and strength, Each subsection details the selection criteria, analysis, and final material choice for each component.

5.1 Core

In composite sandwich structures, the *core* serves as the central layer between two thin, high-strength *skins*, typically made of carbon fiber or fiberglass. The core are usually low-density foams or honeycombs, which increases the panel's bending stiffness by separating the skins and raising the moment arm, following the structural relation $EI \propto h^3$ where h is total thickness.

Including a core material in the design increases structural stiffness while only slightly affecting the total mass. The core is CNC-machined to achieve the required airfoil geometry.

The selection criteria applied were:

- Density below $60\,\text{kg/m}^3$ to minimize weight.
- Young's modulus above $0.05\,\text{GPa}$ to ensure adequate rigidity and mechanical stability.

From an initial set of 135 foam candidates, *ANSYS Granta* recommended five optimal materials. Two key selection charts were used for the evaluation:

- Young's modulus vs. specific density, figure 32.
- Shear strength vs. specific density, figure 33.

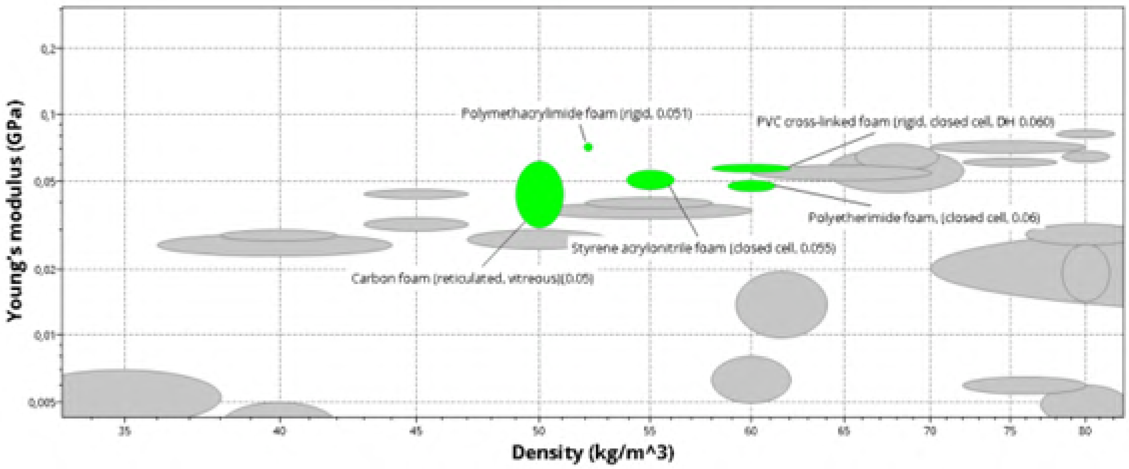

Figure 32: Young's modulus vs. specific density for foam materials.

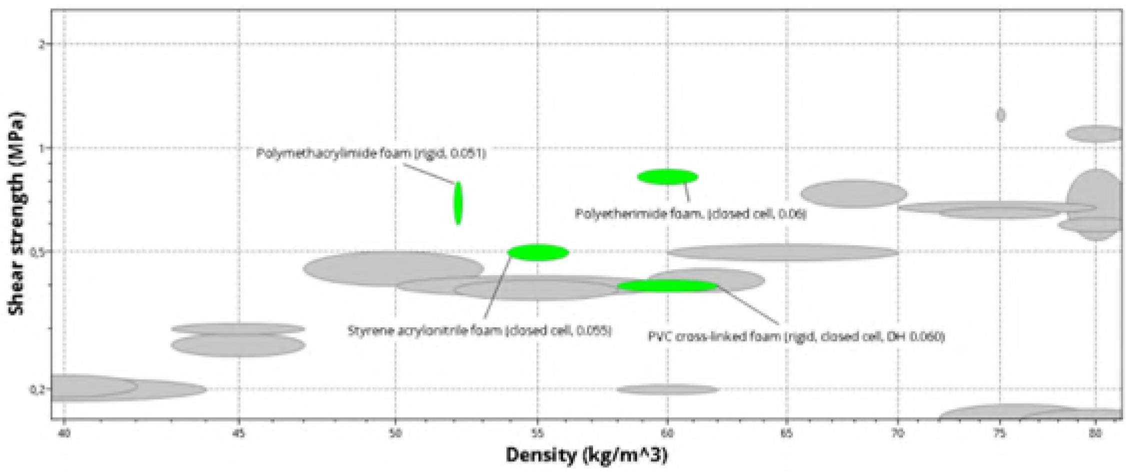

Figure 33: Shear strength vs. specific density for foam materials.

Based on these charts, five foams were identified as potential candidates. The final choice was **polymethacrylimide (PMI) foam**, commercially known as **Rohacell**, due to its excellent balance between stiffness and low density. Although the software suggested a grade with a density of 51 kg/m^3, further review of manufacturer data indicated that **Rohacell 31 IG** (density 31 kg/m^3) provided the desired combination of low weight, high shear strength, and sufficient stiffness.

5.2 Metal Supports

The metal supports connect the DRS and flap components to the main wing structure. These parts are small, machined elements that must exhibit high strength and stiffness while maintaining low mass.

The following criteria guided the material selection:

- Density lower than 3000 kg/m^3 to reduce weight.

- Material cost below 20 /kg to ensure cost efficiency.
- High specific strength and stiffness suitable for precision-machined components.

ANSYS Granta identified aluminum and magnesium alloys as the most suitable options. The final selection, **Aluminum Alloy 7055**, was chosen for its excellent strength-to-weight ratio, high fatigue resistance, and good machinability, characteristics that make it widely used in aerospace and motorsport applications.

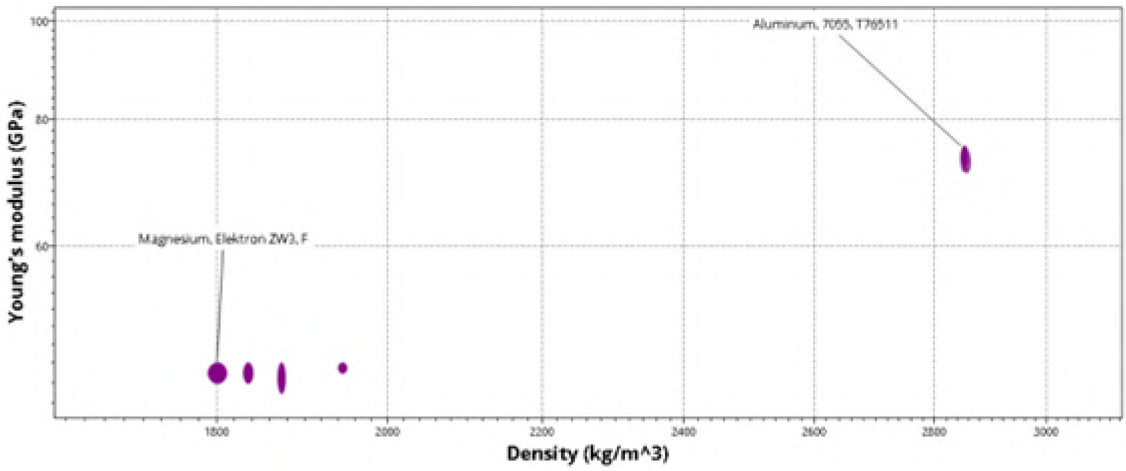

Figure 34: Young's modulus vs. specific density for metallic materials.

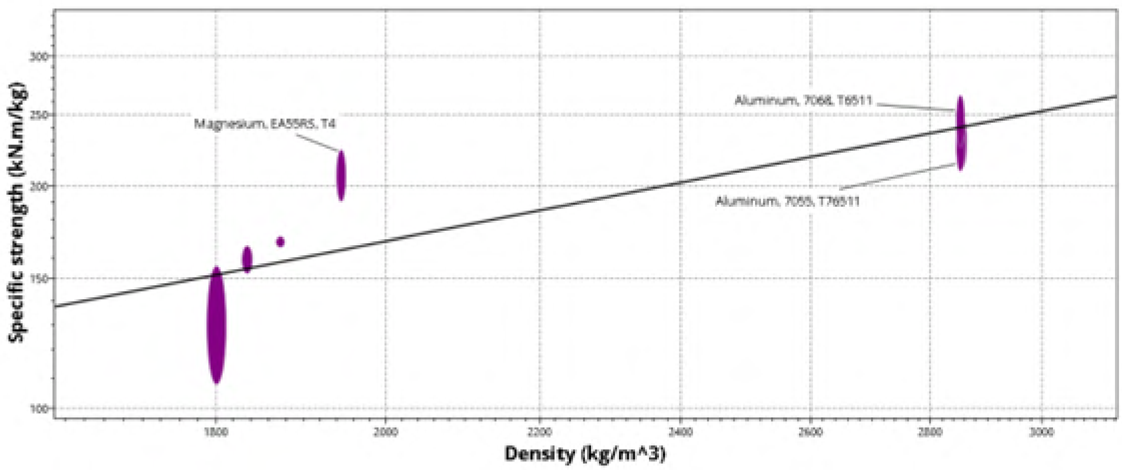

Figure 35: Shear strength vs. specific strength for metallic materials.

5.3 Composite Surface

For the composite surface, a **carbon fiber–reinforced polymer (CFRP)** with an epoxy matrix was selected due to its superior specific stiffness and strength. The software recommended a high-strength carbon fiber, leading to the final selection of **Toray T700S**, a composite commonly used in both motorsport and aerospace industries for its high performance, cost-effectiveness, and availability.

Figures 36 and 37 illustrate the comparison between candidate composites based on specific stiffness and specific strength.

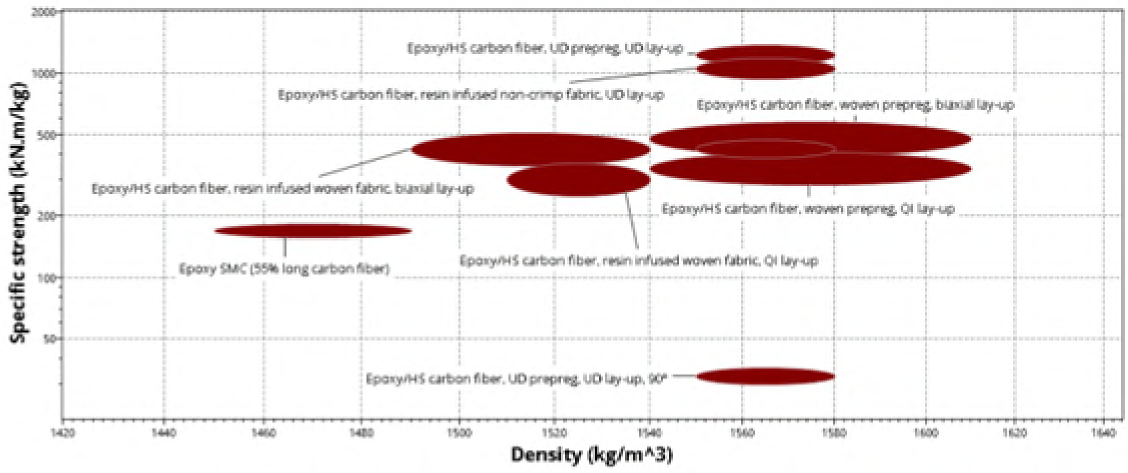

Figure 36: Specific strength vs. specific density for composite materials.

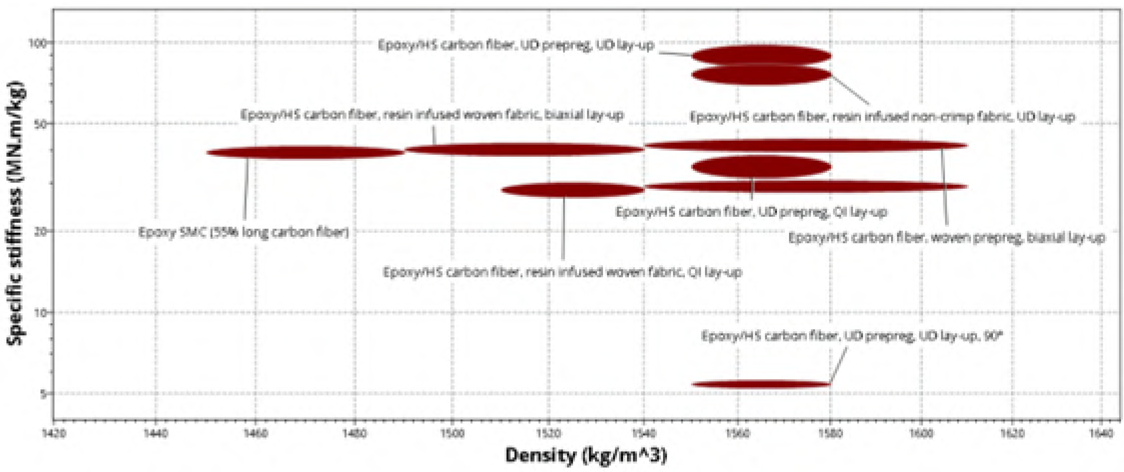

Figure 37: Specific stiffness vs. specific density for composite materials.

Table 31 shows the final materials used in each component and the layup definition.

Table 17: Final optimized layups.

Component	Layup	Thickness
DRS	Toray T700s	1.00 mm
Flap	Toray T700s	0.75 mm
Main wing	Toray T700s	0.75 mm
Core	Rohacell 71 foam	–
Supports	Aluminum 7055	–

6 CAD design

Each team in the Formula One World Championship interprets the rear wing rules differently. The rear wing is a critical aerodynamic component affecting both downforce (cornering) and drag (straight-line speed). Because of the trade-off between high downforce (for twisty circuits like Monaco, Hungaroring or Singapore) and low drag (for high-speed tracks, like Monza, Baku or Spa-Fracorchamps), teams bring multiple rear wing configurations. Within the dimensional and stiffness limits imposed by the FIA, teams are free to design the profile, endplates, beam wing, and flap geometry as they wish. This freedom allows different philosophies to emerge: while some designs favour compact, low-drag solutions to improve top speed, others opt for more aggressive profiles to maximise cornering grip. T-

Throughout the season, the FIA continuously monitors the flexibility and behaviour of the rear wings through load tests and onboard video analysis to ensure that no team exceeds the permitted level of deformation, often referred to as "flexi-wing" effects. In the 2025 Spanish Grand Prix in Montmelo, the FIA changed the maximum deflection allowed for the front wing under these new tests, the allowed movement from a 1000N force droped from 15mm to 10mm when applied on both sides, and 20mm to 15mm when applied on one side.

Figure 38 shows the rear wings designs for Alpine, Red Bull Racing, Williams Racing and Mclaren in the 2025 Italian Gran Prix. This photo is usefull to visualize the different aproaches that each team has followed to design their rear wing. It can be seen that Mclaren (low-right) has a design with more curvatures in the mainwing and in the flaps.

Figure 38: Rear wing design for different teams in the 2025 season

Over the course of a championship, Formula 1 teams can employ anywhere from three to eight distinct rear-wing designs, depending on their resources and development strategy. McLaren was reported to have introduced around eight different rear-wing solutions in the 2024 season, along with more than a dozen variations of the beam wing. Red Bull Racing used approximately five distinct designs, while Mercedes and Ferrari introduced around five to seven each. Smaller teams, constrained by tighter budgets, often limit themselves to three or four main wing configurations, which they adjust slightly with gurneys or flap trims to suit particular races.

Teams that field a larger number of rear-wing versions tend to be those pursuing continuous aerodynamic improvements throughout the year. McLaren, for example, has recently used this strategy to gain efficiency and competitiveness, bringing a new or revised wing at multiple rounds. In contrast, Red Bull's dominance in recent seasons has been achieved with a smaller number of optimised designs, focusing instead on refining existing geometries. This variation in development philosophy illustrates how differently teams interpret both the technical and strategic aspects of wing design under the cost-cap era.

Visually, these differences are easy to identify when comparing rear-wing assemblies between teams and even within the same team at different races. The endplate design, the curvature of the mainplane, and the interaction with the beam wing can vary significantly. For example, a McLaren or Ferrari rear wing at Monaco typically shows a deep chord and aggressive curvature, while their Monza-spec wings are much flatter, with trimmed flaps and reduced surface area. Mercedes and Red Bull also exhibit clear distinctions between their high-downforce and low-drag configurations, visible in the shape of the flap transition and the placement of the DRS actuator. These visual contrasts underline how tailored each design is to the aerodynamic profile required by a given circuit. Figure 39 shows the different designs of the rear wing that Mclaren designed for the Mexico Grand Prix (upper) and Brazil Grand Prix.

Figure 39: Mclaren rear wing comparison between mexico and brazil during the 2025 races

The proposed design consists of three primary composite components: the **main wing** (lower fixed section), the **DRS element** (central upper section), and the **flaps** (upper side sections), ilustrated in figure 40.

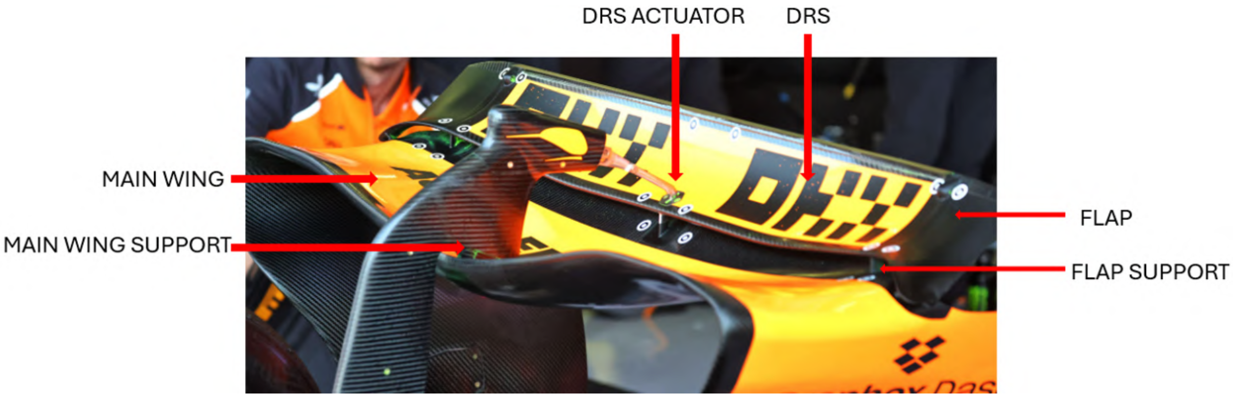

Figure 40: Rear wing components

The main wing forms the primary aerodynamic surface generating downforce, serving as the structural foundation to which all other components attach. It maintains consistent aerodynamic performance across all conditions. The DRS (Drag Reduction System) is a movable aerodynamic device installed on the rear wing of a Formula 1 car, designed to reduce aerodynamic drag and increase straight-line speed during overtaking maneuvers. The system allows the driver to open a flap on the rear wing, which alters the airflow and reduces downforce, thereby improving acceleration and top speed on straights.

According to the FIA Formula 1 Technical Regulations, Article 3.18.1, the DRS must comply with strict dimensional limits. Specifically, when the DRS is activated, the maximum gap allowed between the main plane and the flap must not exceed 85 mm. This regulation ensures that the system remains within safe and controlled limits, preventing excessive loss of downforce that could compromise car stability.

The DRS is actuated by a hydraulic or electric mechanism controlled by the driver via a button on the steering wheel. When activated, the system moves a flap on the rear wing, which is connected to the main plane by a pin. This pin allows the flap to rotate relative to the main plane, enabling the opening and closing motion of the DRS. The flap itself remains fixed to the wing structure, while the DRS moves independently, creating the gap that reduces drag. Figure 41 shows the same rear wing when the drs is open (lower) or closed (upper).

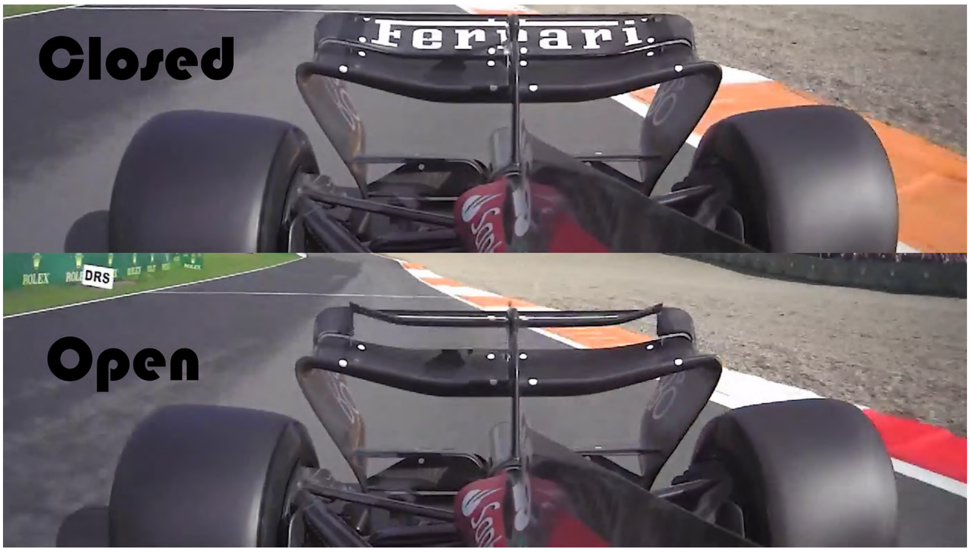

Figure 41: Formula 1 rear wing with the drs open and the drs closed.

6.1 Reversed engineering

For the development of the CAD model used in this project, a reverse engineering approach was applied based on the McLaren MCL39, which is shown in figure 42, the Formula 1 car driven by Oscar Piastri and Lando Norris and manufactured by McLaren Racing.

Figure 42: Mclaren MCL 39

This process involved the analysis of publicly available technical data, images, and reference dimensions in order to accurately reproduce the main geometric features of the vehicle. The objective of this approach was not to obtain an exact replica, but to generate a representative model suitable for design, analysis, and further development within the scope of this project.

Different views and angles were used to obtain the rear wing measurements. This methodology allowed for a more accurate estimation of the wing geometry by cross-referencing dimensions from multiple perspectives, reducing errors caused by perspective distortion. Figure 43 and figure 44 shows the measurements of the design.

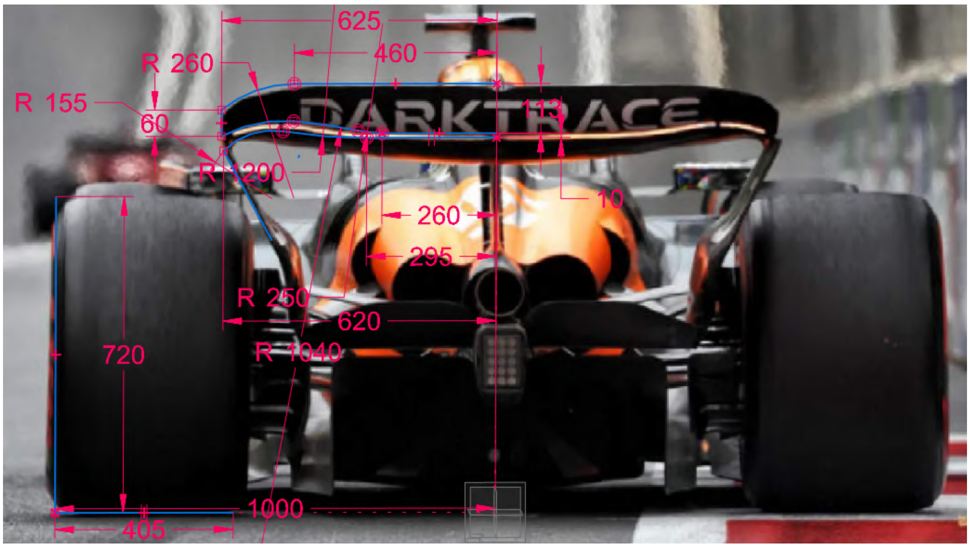

Figure 43: Measurements from the Mclaren MCL 39 rear view

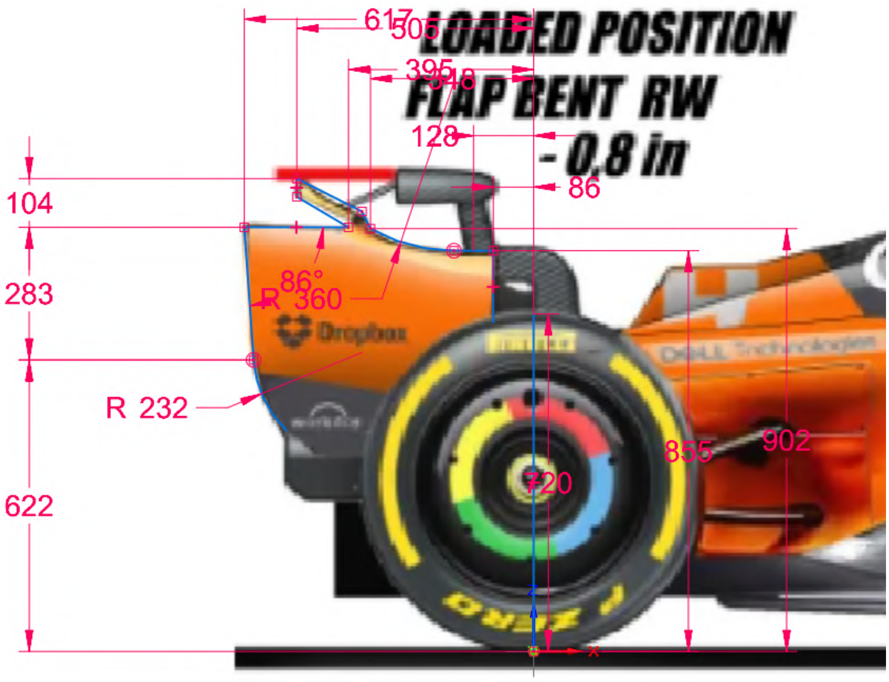

Figure 44: Measurements from the Mclaren MCL 39 lateral view

The final CAD model is shown in figure 45, in which the endplates are omitted. Their aerodynamic effect is represented by fixing the main wing at both sides, an assumption that adequately captures their influence for the purposes of this study. Including the endplates would significantly increase the complexity and computational time of the simulations, while having a negligible impact on the accuracy of the results obtained. In this figure, the main wing is shown in red, the DRS element is shown in blue, the flaps are shown in black, and the supports are shown in grey. Figure 46 shows a detailed view of the flap supports.

Figure 45: CAD model designed

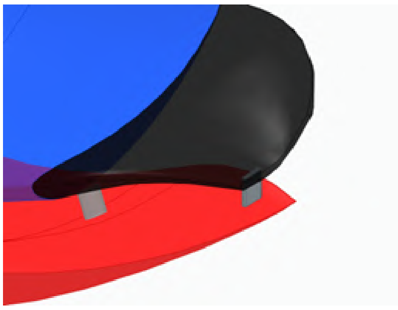

Figure 46: Detail view of the CAD model designed

6.2 Compliance with the FIA regulations

The FIA Technical Regulations for the 2025 season define a reference volume for the rear wing, as specified on pages 153 to 156. These regulations divide the rear wing into different components and strictly delimit the allowable volume for each of them, thereby constraining the design to remain within prescribed geometric boundaries. Based on these regulatory constraints, the model was developed in a CAD environment, and the rear wing geometry was introduced within the defined reference volume. This approach made it possible to verify that the proposed design fully complies with the dimensional limits imposed by the FIA, ensuring its legality with respect to the 2025 technical regulations. Figure 47 show the final CAD design positioned inside the reference volume, verifying that the geometry remains fully within the limits established by the regulations.

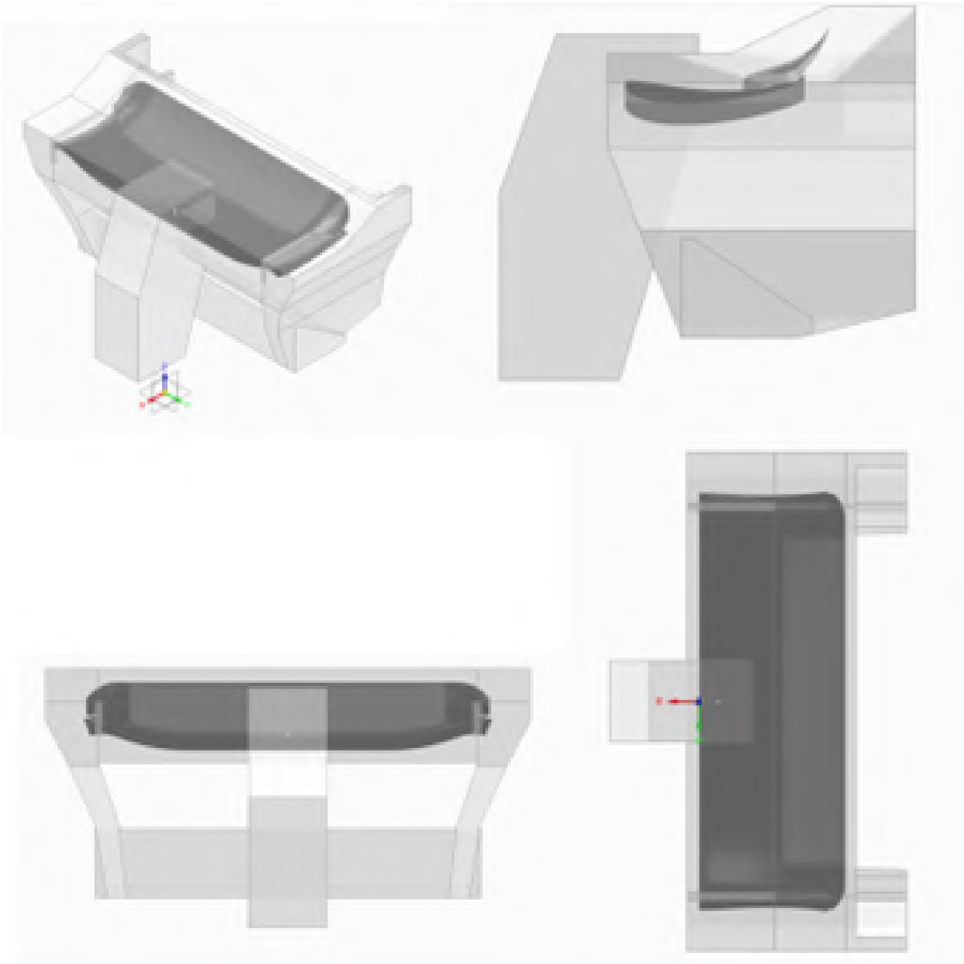

Figure 47: CAD design inside reference volume

7 FEM analysis

The finite element analysis (FEA) is performed using ANSYS. This analysis involves the definition of the carbon fibre laminate layup as well as the static load cases imposed by the FIA regulations. The FIA Technical Regulations define specific articles that constrain the allowable flexibility of the rear wing and prescribe the static loads that the structure must withstand. These regulations also establish different load cases that must be evaluated in order to ensure compliance with the rules and to verify the structural integrity of the rear wing under all required conditions.

7.1 Regulation

This section defines the relevant articles of the FIA Technical Regulations that establish the load cases for the rear wing and describes how these loads are applied within ANSYS Static Structural analyses.

- **3.15.9 Rear Wing Mainplane Flexibility**

  With this article, the FIA aims to replicate the aerodynamic forces experienced at high speeds and to prevent excessive structural flexibility that could lead to unintended aerodynamic advantages. Figure 48 and Figure 49 ilustrate how this load case is applied in ANSYS.

  a. Bodywork may not deflect more than 6mm along the loading axis and 1.0° in a Y-plane, when two loads of [0, 0, -1000]N each, are applied simultaneously to the Rear Wing Profiles. The loads will be applied at [XR=375, ±300, 910]

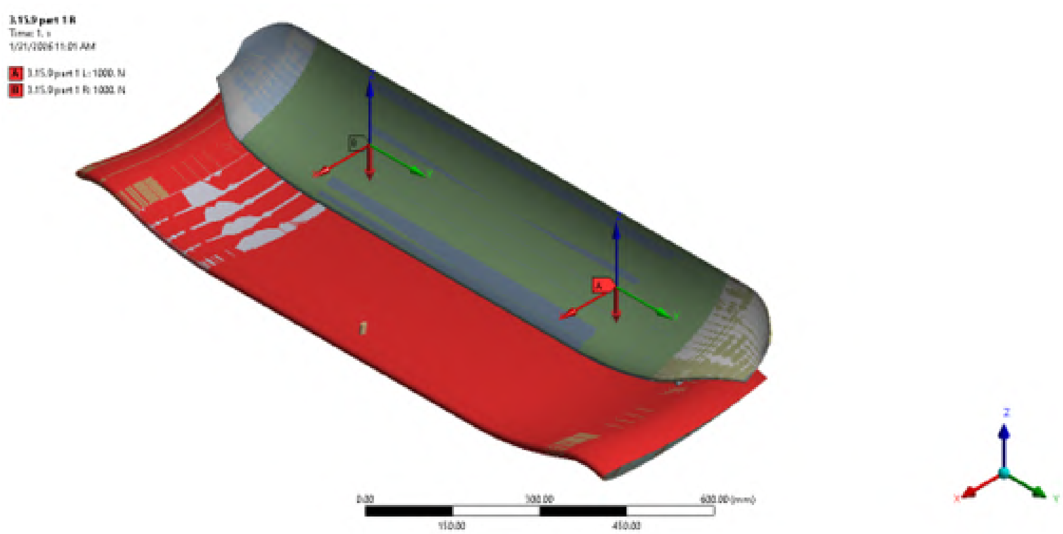

Figure 48: article 3.15.9 part 1 on ANSYS

b. Bodywork may not deflect more than 6mm along the loading axis and 1.0° in a Y-plane, when two loads of [324, 0, -940]N each, are applied simultaneously to the Rear Wing Profiles. The loads will be applied at [XR=325, ±300, 900]

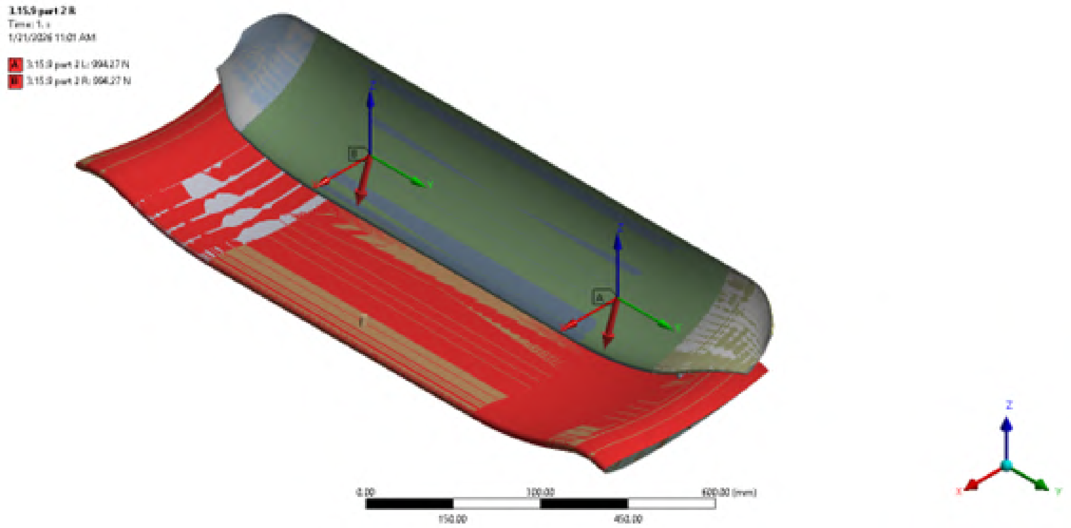

Figure 49: article 3.15.9 part 2 on ANSYS

- **3.15.10 Rear Wing Flap Flexibility**

  This regulation defines a stiffness requirement for the rear wing flap in order to limit its horizontal flexibility under aerodynamic loading.

  The RW Flap may deflect no more than 7mm horizontally when a 500N load is applied horizontally. The load will be applied in the plane Z=875 at one of three separate points which lie within 50mm of the car centre plane and 270mm either side of it. The loads will be applied in a rearward direction using a suitable 25mm wide adaptor which must be supplied by the relevant team. The deflection will be measured along the loading axis and relative to the forward part of the Rear Wing Mainplane at the same Y-station.

  Two simulations are performed, one at Y = 50 mm and another at Y = 270 mm, in order to evaluate the behaviour of the wing at both extremes of the specified interval. If the design satisfies the deflection limits at these two critical positions, it can be assumed that the rear wing complies with the regulation across the entire interval. Figure ?? and Figure ?? ilustrate how this load case is applied in ANSYS.

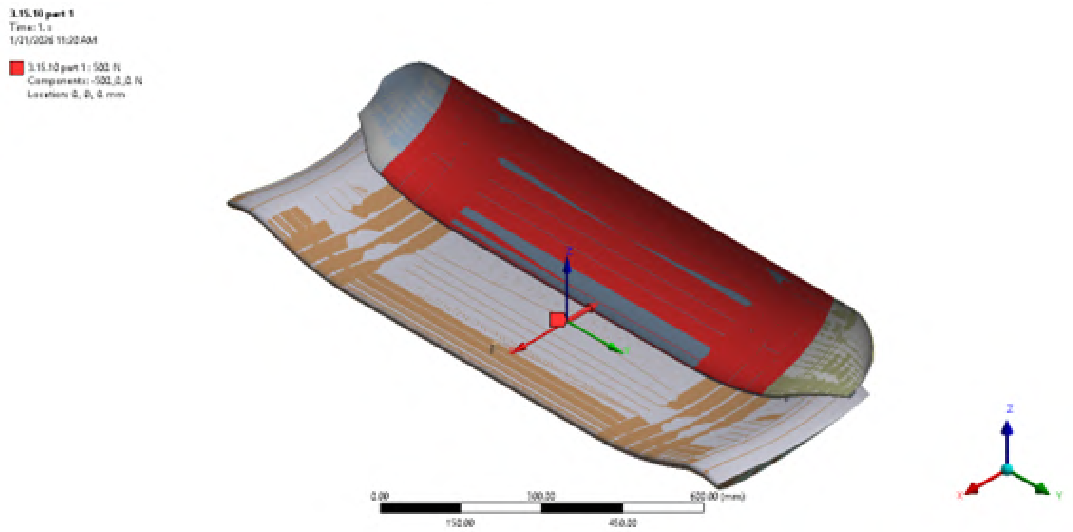

Figure 50: Article 3.15.10 part 1 on ANSYS

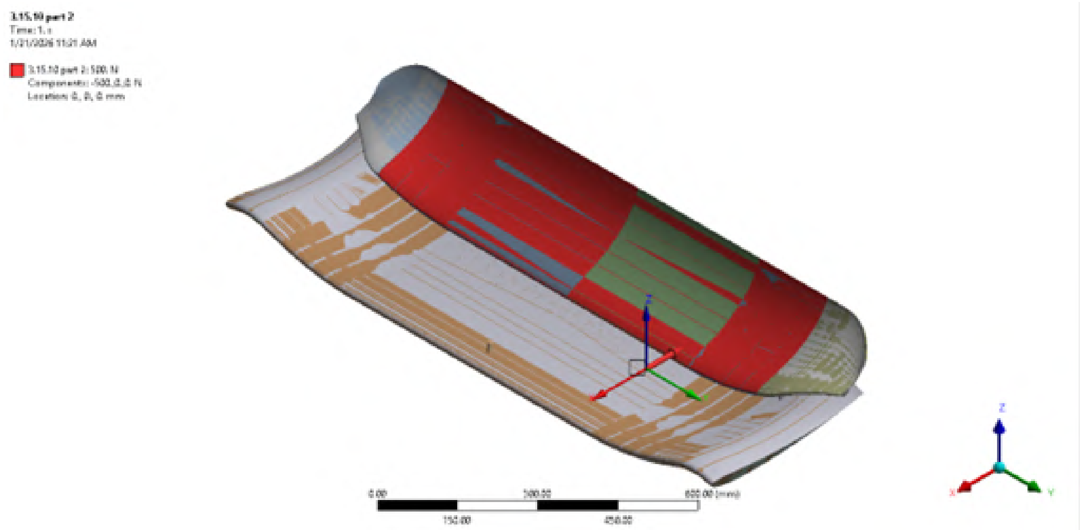

Figure 51: Article 3.15.10 part 2 on ANSYS

- **3.15.11 Rear Wing Mainplane Trailing Edge**

  This regulation establishes a stiffness requirement for the forward-most aerofoil element of the rear wing profiles in order to limit its deformation under aerodynamic loading. The force is applied in the trailing edge, which is the rear-most edge of an aerodynamic profile, where the upper and lower surfaces meet. It is the point at which the airflow leaves the surface after passing over the aerofoil. The force pushes the element upwards, trying to bend it, replicating downforce load.Figure 52, figure 53 and figure 54 show how this three loadcases are applied in the simulation.

  The forward-most aerofoil element of Rear Wing Profiles may deflect no more than 3mm along the line of load application, when

a 200N load is applied normal to the lower surface. The load will be applied in line with the trailing edge of the element at Y=0, Y=±125, or at Y=±375. The deflection will be measured relative to the forward part of the Rear Wing Mainplane at the same Y-station

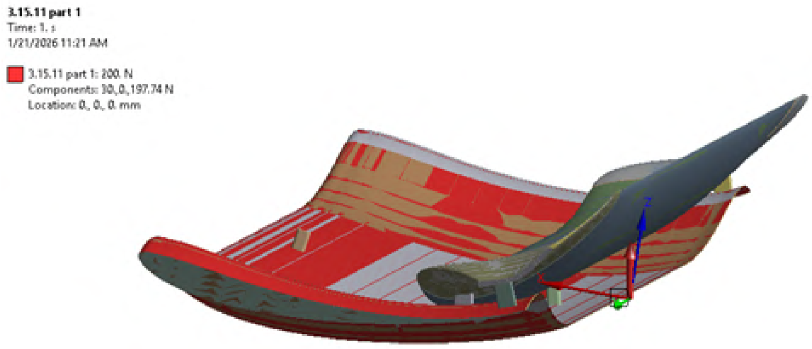

Figure 52: article 3.15.11 part 1 on ANSYS

Figure 53: article 3.15.11 part 2 on ANSYS

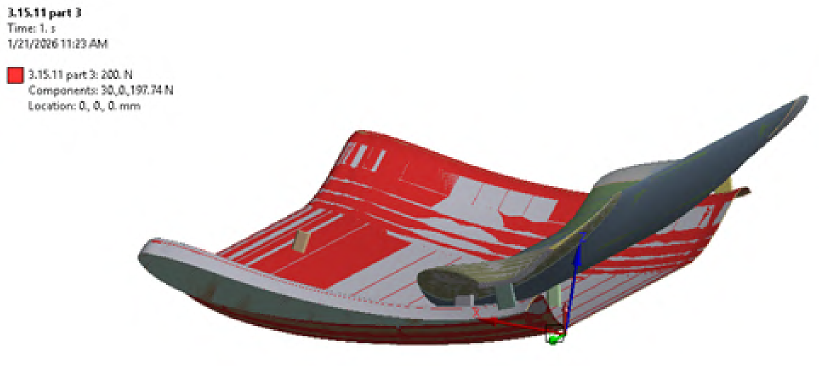

Figure 54: article 3.15.11 part 3 on ANSYS

7.2 ANSYS simulations

This section describes the simulation methodology adopted in this project. Figure 55 shows the workflow implemented in ANSYS Workbench, which is divided into three main blocks. Each block corresponds to a specific stage of the modelling and analysis process and is described in detail below.

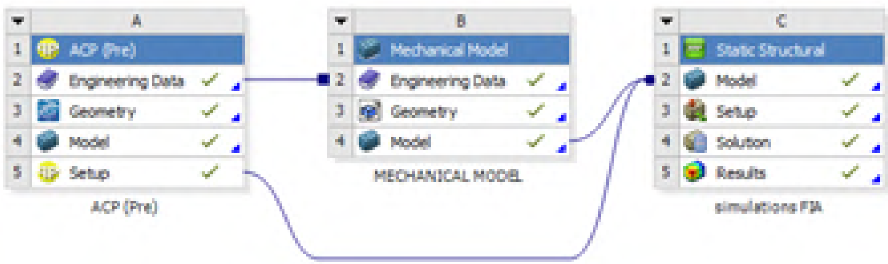

Figure 55: ANSYS workbench workflow

Block A: ACP (Pre)

ACP (ANSYS Composite PrepPost) is a dedicated ANSYS module specifically developed for the modelling and analysis of composite structures. ACP (Pre) is used in the preprocessing stage to define composite materials, laminate layups, ply orientations, stacking sequences, and thickness distributions. It enables an accurate representation of anisotropic composite behaviour and allows the composite definition to be seamlessly linked with structural solvers such as Static Structural for finite element analysis.

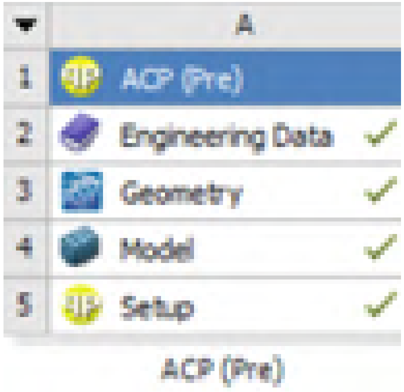

Figure 56: ACP block

- **Engineering Data**

  Engineering Data in ANSYS is the database where the material properties required for simulations are defined and managed. This section includes the mechanical, thermal, and physical properties of each material used in the model. For this project, the Engineering Data module contains the material definitions for the carbon fibre composites, the Rohacell core, and the metallic components. These properties are subsequently assigned to the corresponding plies, cores, and structural parts, ensuring that the numerical model accurately reflects the real mechanical behaviour of the materials involved. The materials used are shown in table 31, and are used in the following components:

Table 18: Final optimized layups.

Component	Layup	Thickness
DRS	$[woven(0°)/ud(0°)/ud(67°)/ud(0°)]_s$	1.00 mm
Flap	$[woven(0°)/ud(0°)/ud(0°)]_s$	0.75 mm
Main wing	$[woven(0°)/ud(0°)/ud(0°)]_s$	0.75 mm
Core	Rohacell 71 foam	–
Supports	Aluminum 7055	–

The rear wing is manufactured using a **Rohacell core**. Rohacell is a closed-cell polymethacrylimide (PMI) structural foam widely used as a core material in high-performance sandwich structures due to its high stiffness-to-weight ratio, excellent compressive and shear strength, and good thermal and chemical resistance. These properties make Rohacell particularly suitable for lightweight applications where structural efficiency and dimensional stability are critical. Rohacell is commonly used in aerospace components, motorsport structures, wind turbine blades, satellite panels, and high-end automotive and sporting goods, where minimizing weight while maintaining structural performance is essential. In composite structures, it is typically combined with carbon fibre skins to form sandwich panels that offer high bending stiffness with minimal mass.

Figure 57: ROHACELL used as core

For this project, two Rohacell grades were analysed: Rohacell 31 and Rohacell 71. These grades were selected because they have the lowest densities within the Rohacell product range, making them especially attractive for Formula 1 applications, where strict mass reduction is a key design objective.

Over the Rohacell core, layers of **carbon fiber–reinforced polymer** are applied, and the aim of this project is to determine the most optimal combination of fiber type, ply orientation, and laminate layup (plybook) in order to achieve the best balance between structural performance and weight efficiency. The carbon fiber selected for this design is Toray T700, a high-strength, standard-modulus fiber widely used in aerospace, motorsport, and high-performance automotive applications due to its excellent strength-to-weight ratio, good fatigue resistance, and reliable manufacturability. T700 provides sufficient stiffness without the brittleness associated with higher-modulus fibers, making it particularly suitable for sandwich structures with foam cores such as Rohacell, where damage tolerance and load redistribution are important. This fiber is commonly used in secondary aircraft structures, racing car body panels, control surfaces, and lightweight sandwich panels. Two types of carbon fiber architectures are considered in this project: unidirectional plies, which provide maximum stiffness and strength along the primary load directions, and woven fabrics, which offer improved handling, impact resistance, and multidirectional load distribution. By combining these fiber forms with optimized ply orientations, the laminate can be tailored to efficiently carry bending, shear, and in-plane loads while minimizing overall mass. Figure 58 shows the difference betweeen a woven CFRP and unidirectional CFRP.

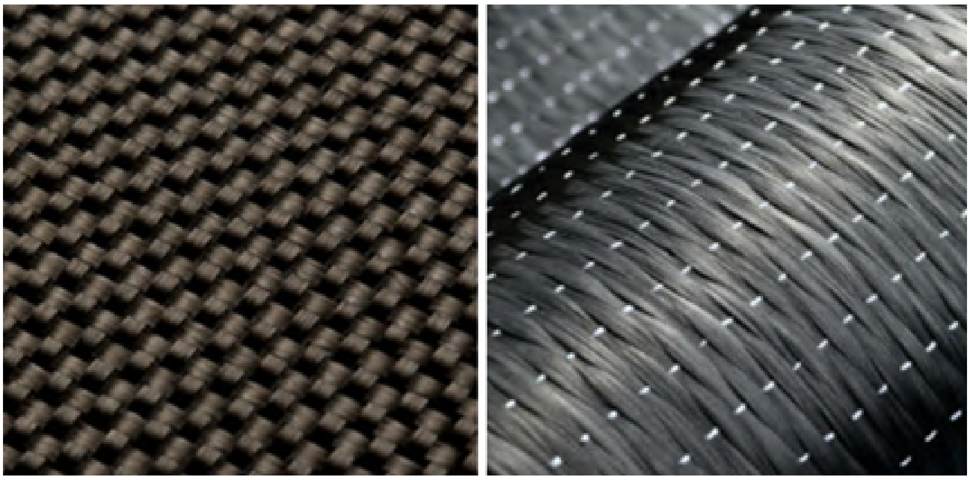

Figure 58: Woven (left) vs unidirectional (right)

- **Geometry**

  This section allows the modification of the geometry using ANSYS SpaceClaim. The complete rear wing geometry is imported as a STEP file, in which the rear wing is initially defined as a solid body rather than as a surface. Within SpaceClaim, the geometry is modified to convert the solid body into surface geometry, which is required for the correct definition of the carbon fiber laminates in the composite analysis. During this process, the metallic components are removed from the model, as these parts are manufactured from titanium and are not intended to be modelled as carbon fiber structures. Additionally, each surface is renamed to clearly identify its function and its corresponding subassembly, facilitating the assignment of materials, layups, and boundary conditions in later stages of the analysis. Figure 59 shows the SpaceClaim environment and the geometry tree, illustrating the naming convention used for each surface.

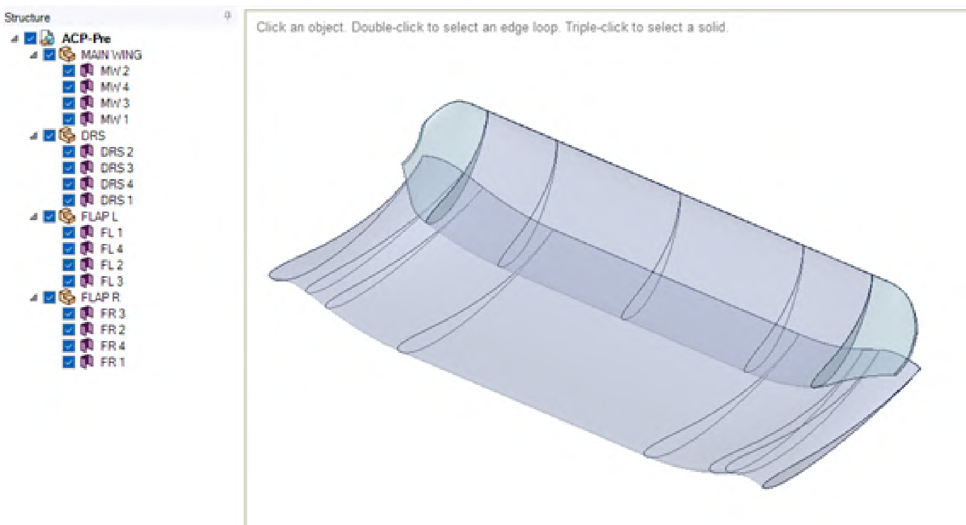

Figure 59: Model in SPACECLAIM

- **Model**

  This section defines the connections between the different surfaces and the generation of the finite element mesh. The meshing strategy adopted for the analysis is shown in figure 60 and a detail view is shown in figure 61. To create the mesh, face meshing is applied to the rear wing and DRS surfaces, allowing for a smooth and well-structured mesh along the aerodynamic surfaces. This approach ensures an adequate representation of the geometry and improves the accuracy of the results while maintaining reasonable computational efficiency.

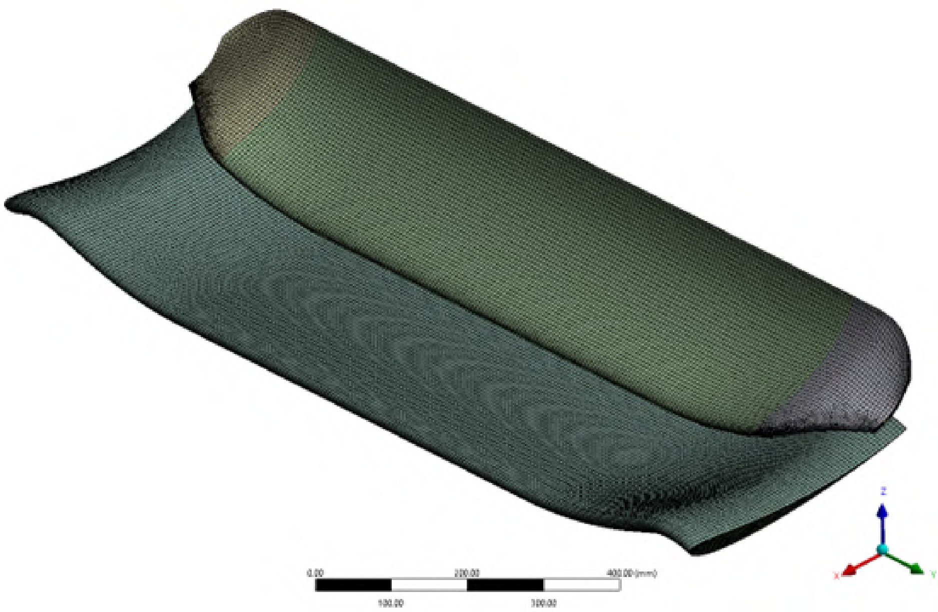

Figure 60: ACP mesh

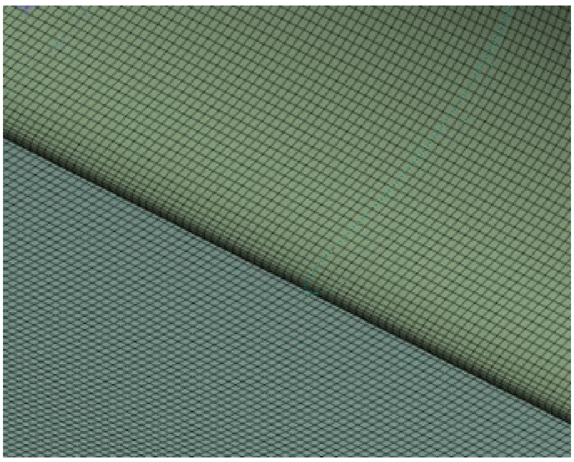

Figure 61: ACP mesh detail 1

Additional mesh refinement has been applied to all the edges of the rear wing and the DRS tip, where characteristic lengths are very small. This refinement increases the element density in these critical regions, allowing for a more accurate representation of the geometry and local stress gradients. figure 62 shows a detailed view of the lateral surface of the flap, where the applied edge refinement can be observed.

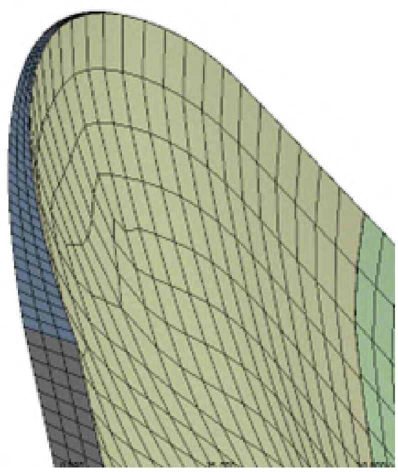

Figure 62: ACP mesh detail 2

- **Setup**

  In this section, the composite layup is defined by specifying the plybook, stacking sequence, and fiber orientations for each component. This step establishes the thickness and material distribution of the composite structure and is essential for accurately representing its mechanical behaviour. Figure 63 shows the model with a plybook applied, where the resulting thickness of each component can be observed.

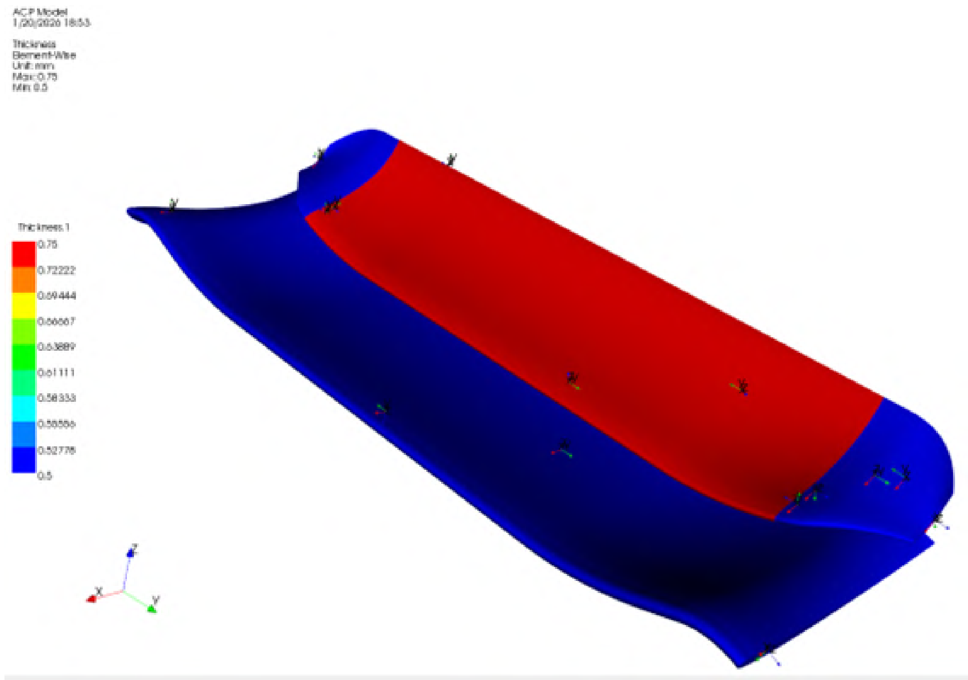

Figure 63: ACP variable thickness display

Figure 64 and figure 65 shows the layup verification, where it is confirmed that the surface normal is oriented towards the outside of the structure rather than towards the interior, where the Rohacell core is located. The orange arrows indicate the direction of the surface normal, which defines the stacking direction of the plies.

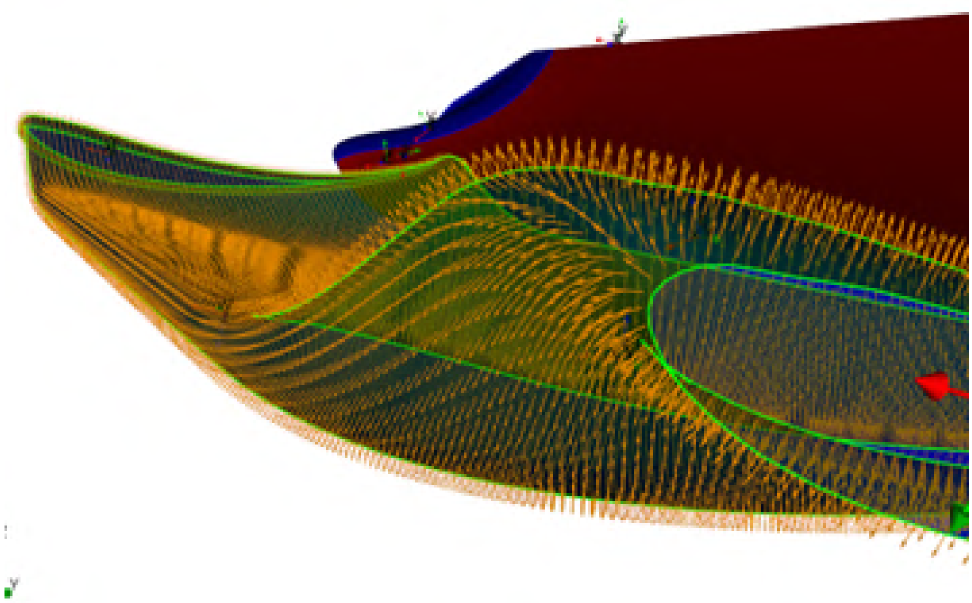

Figure 64: ACP normal direction verification

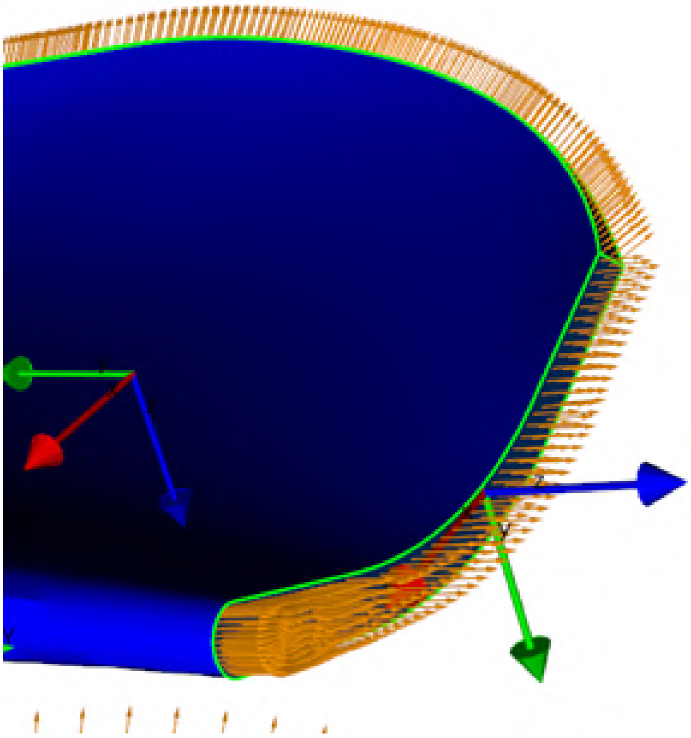

Figure 65: ACP normal direction verification detail view

Block B: Mechanical Model

Block B corresponds to the Mechanical model. This block is used to define the core components, including the Rohacell core, as well as the metallic supports and boundary conditions required for the analysis. It provides the structural framework on which the composite layup is applied.

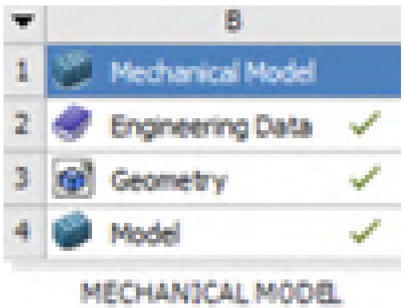

Figure 66: Mechanical block

- **Engineering Data**

  The Engineering Data definition is the same as that used in ACP (Pre), ensuring consistency in the material properties assigned throughout the analysis.

- **Geometry**

  This section receives the same STEP file used in ACP (Pre); however, the geometry is edited in SpaceClaim to represent the components as solid bodies rather than surfaces. This modification is necessary to correctly model the Rohacell core and the mechanical supports within the structural analysis.

- **Model**

  This part of the workflow is used to generate the mesh for the Rohacell core and the mechanical supports. The resulting mesh enables the accurate representation of the core behaviour and the interaction between the composite skins and the supporting structural components.

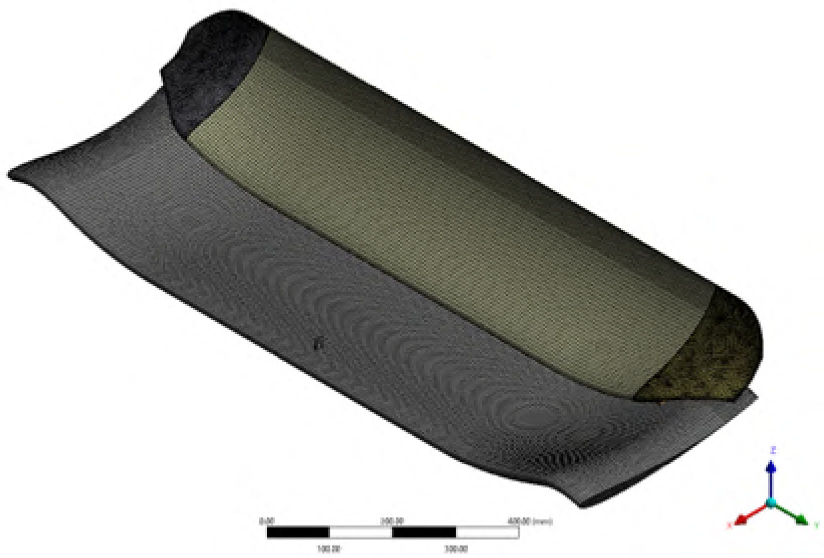

Figure 67: Mechanical meshing

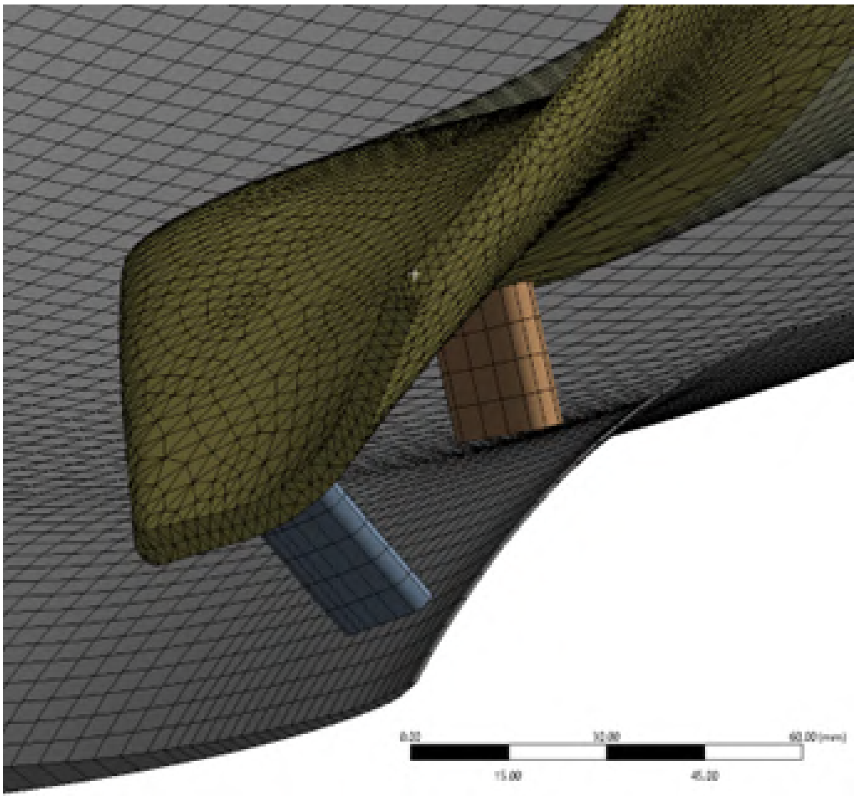

Figure 68: Mechanical meshing detail

Block C: static structural

Block C corresponds to the Static Structural analysis. In this block, the geometry and composite layup defined in ACP (Pre) are linked with the mechanical model, creating a fully coupled representation of the rear wing assembly. This integrated model is then used to perform the simulations and evaluate the structural response under the prescribed load cases.

Figure 69: Structural block

This section presents the results of the simulations described previously and outlines the iterative methodology applied to optimise the plybook configuration. In all load cases, the boundary conditions remain the same. The rear wing is fixed at the two surfaces that connect the main wing to the endplates, as well as at the main wing support. Figure 70 shows the surfaces considered as fixed, which are indicated by blue arrows. Figure 71 provides a detailed view of the fixed surface at the main wing support.

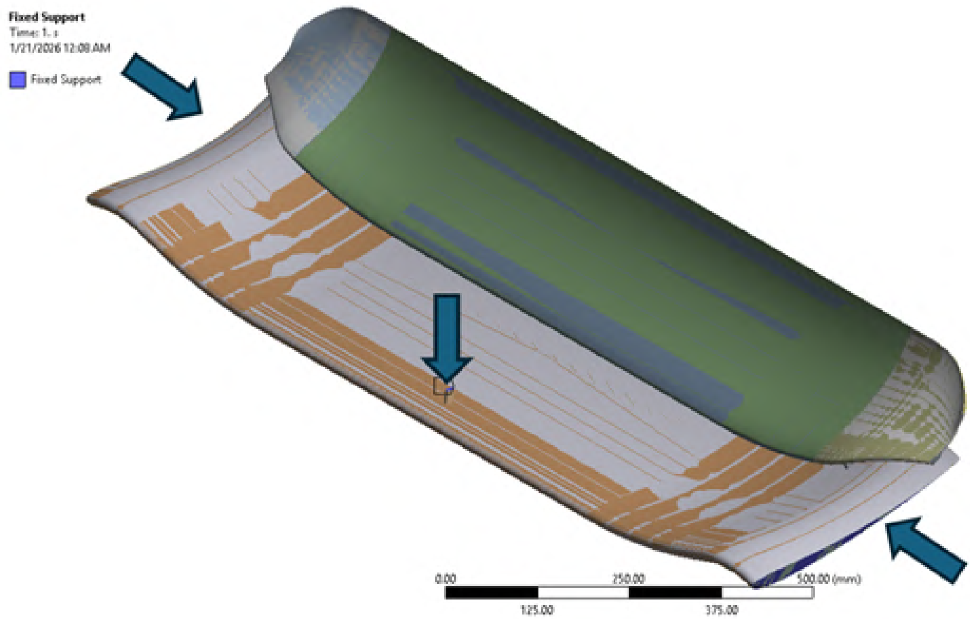

Figure 70: Fixed sections

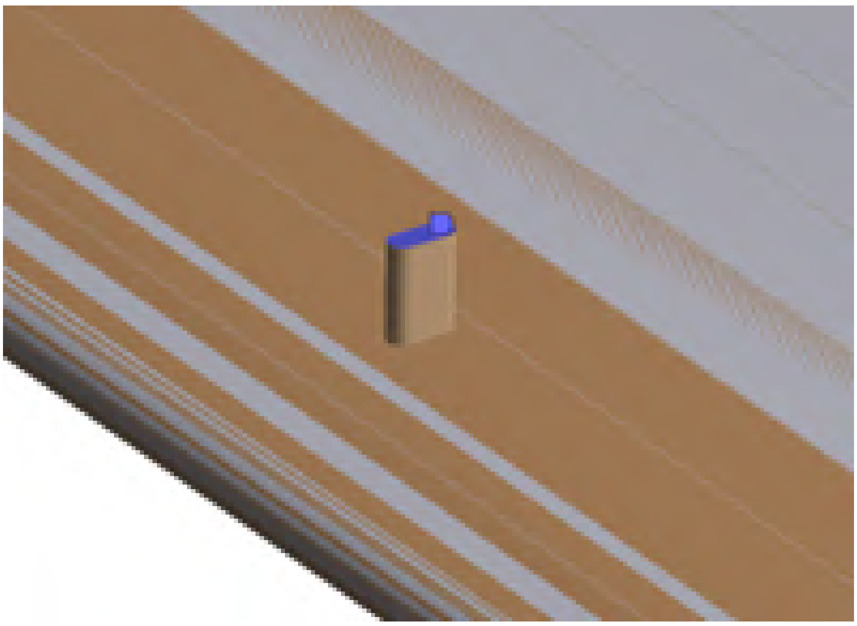

Figure 71: Fixed sections detail view

7.3 Plybook iteration

The workflow consists of defining an initial plybook, simulating all the load cases imposed by the regulations, and iteratively optimising the number of plies and their orientations. The objective is to achieve the minimum possible weight while maintaining deflections within the regulatory limits, thereby maximising structural performance and minimising mass.

Table 19 presents the weight of each carbon fiber layer for every component, calculated as the sum of all the surfaces that comprise each respective component.

Table 19: Weight of each surface

Surface	Volume/layer (mm^3)	Weight/layer (g)
MAIN WING	668.68	159.35
MW1	1054.60	157.14
MW2	668.68	159.35
MW3	1054.60	157.14
MW4	103.6	80.22
DRS	366.47	0.55
DRS1	5305.70	79.5
DRS2	45.69	8.74
DRS3	336.47	0.55
FLAP LEFT	5305.70	79.5
FL1	45.69	8.74
FL2	20.95	0.74
FL3	336.47	0.55
FL4	543.28	8.05
FLAP RIGHT	20.95	0.74
FR1	336.47	0.55
FR2	543.28	8.05
FR3	20.95	0.74

Table 20 shows the weight difference for each component using Rohacell when comparing the high-density grade (RH71) with the lower-density grade (RH31).

Table 20: Weight of the Rohacell core

Component	RH71 weight (g)	RH31 weight (g)	Difference (g)
DRS	316.40	135.00	181.41
MAIN WING	660.70	281.90	378.80
FLAP	20.44	8.73	11.72

A safety factor of 1.5 is applied to all simulations. Table 21 presents the maximum allowable displacement for each simulation, taking the safety factor into account.

Table 21: Maximum allowable displacement

Test	**Target (mm)**	**Achieved (mm)**
3.15.9 part 1	6.0	4.0
3.15.9 part 2	6.0	4.0
3.15.10 part 1	7.0	4.67
3.15.11 part 1	3.0	2.0
3.15.11 part 2	3.0	2.0
3.15.11 part 3	3.0	2.0

Tables 22, 23 and 24 shows the selected plybook and core material for each configuration and the main wing, the drs and the flap respectively. The columns A, B, and C correspond to different plybook definitions, where the layups are modified to evaluate their influence on the maximum displacement. Each plybook is symmetrical, meaning the component consists of a Rohacell core machined using a 5-axis CNC to achieve the desired geometry, followed by the application of the defined layup across the entire surface. For example, layup A consists of an RH71 core followed by a UD 0° layer and a woven layer oriented at 0° on top, with the woven 0° layer left as the outer visible surface.

Table 22: Main wing layup

	A	**B**	**C**
Core	RH71	RH71	RH71
Layup	[Woven 0, UD 0]	[Woven 0, UD 0, UD 45]	[Woven 0, UD 0, UD 45, UD 0]

Table 23: DRS layup

	A	**B**	**C**
Core	RH71	RH31	RH31
Layup	[Woven 0, UD 0]	[Woven 0, UD 0]	[Woven 0, UD 0]

Table 24: Flap layup

	A	**B**	**C**
Core	RH71	RH31	RH31
Layup	[Woven 0, UD 0]	[Woven 0, UD 0]	[Woven 0, UD 0]

Table 25 presents the results of the simulations for each configuration, showing the maximum displacement obtained in the element evaluated by each regulatory article.

Table 25: Maximum displacement margin comparison in mm

		A	B	C
Mainplane	3.15.9 part 1	4.15	4.18	3.62
	3.15.9 part 2	3.81	3.08	3.91
DRS	3.15.10 part 1	4.10	3.98	3.71
	3.15.10 part 2	1.27	0.82	0.71
Mainplane	3.15.11 part 1	3.15	0.45	0.30
	3.15.11 part 2	3.27	0.42	0.38
	3.15.11 part 3	0.50	0.46	0.39

- **Iteration 1: Configuration A**

  This configuration uses rohacell 71 as core for all the components.The results of Iteration 1 indicate that there is still a margin to increase deflection in DRS but the deflection of the main wing has to be reduced , suggesting that the stiffness of the drs must be decrease whereas the stiffness of the maingwing must be increased.

- **Iteration 2: Configuration B**

  To increase the stiffness of the rear wing, an additional layer of carbon fibre is added to its layup. Conversely, to reduce the stiffness of the DRS and flap, the core material is changed from Rohacell RH71 to the lower-density RH31. This configuration allows the study of the trade-off between weight reduction and structural performance across different components of the rear wing assembly. Using the data from figures ?? and ??, it is possible to calculate that by changing the main wing core from the high-density Rohacell (RH71) to the lower-density RH31 and adding one additional ply to the layup, the overall weight of the component decreases. This iteration is therefore used to evaluate how much displacement can be gained from this configuration change and to study the trade-off between weight savings and the resulting structural stiffness.

- **Iteration 3: Configuration C**

  In Iteration 3, the number of layers of the main wing is adjusted to control its stiffness. The analysis of Article 3.15.9 shows that the main wing displacement reaches 105 percent in configuration b so the rear wing receives another layer of carbon fiber.

8 CFD analysis

This section presents the procedure followed and the results obtained from the CFD analysis of the rear wing. The study focuses on the aerodynamic behaviour of the rear wing in a high speed straight condition, representative of a typical high speed circuit on the Formula 1 calendar. The Autodromo Nazionale di Monza has been selected for this analysis, as it is widely regarded as one of the fastest circuits in the championship, characterized by long straights and low downforce rear wing configurations.

The specific case investigated corresponds to the end of the main straight, just before Turn 1, at the speed trap. The layout of the Monza circuit is shown in figure 72. In this section, Formula 1 cars usually reach speeds in the range of 340 to 360 km/h, depending on the car, season and race conditions. The chosen simulation condition corresponds to a recorded speed of 353.1 km/h, equivalent to 98.1 m/s, achieved by Oscar Piastri driving the McLaren MCL39 during the 2025 season. This velocity represents a realistic and performance relevant condition, suitable for assessing the rear wing's efficiency in a typical high speed race scenario.

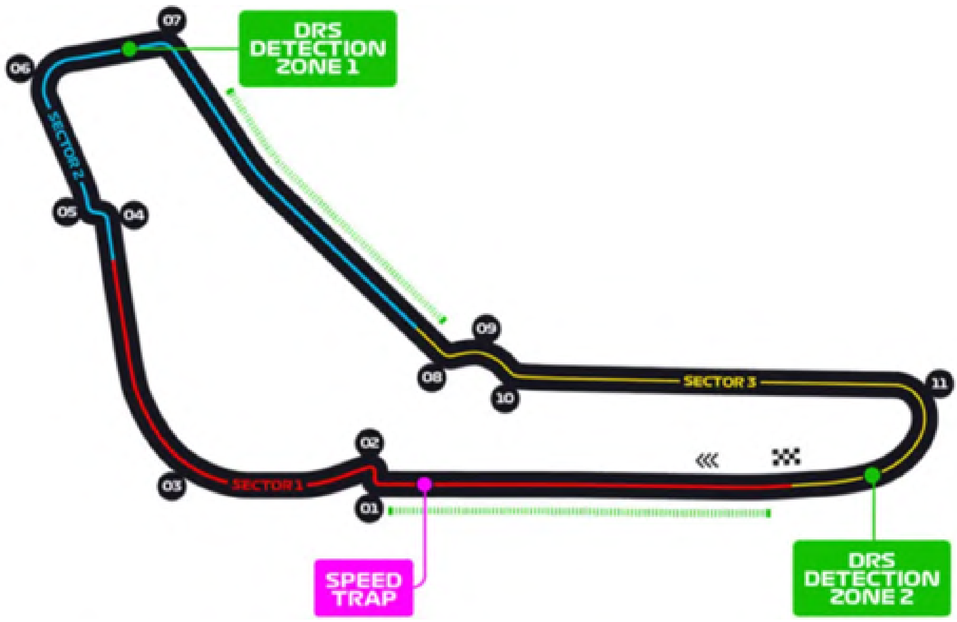

Figure 72: Monza layout

8.1 ANSYS implementation

The computational domain was created using **ANSYS Fluid Flow (CFX)**, a widely used solver for high-fidelity steady-state and transient CFD simulations. The overall structure and topology of the block, designed to capture the flow around the rear wing accurately, is shown in figure 73.

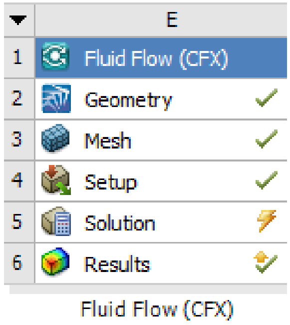

Figure 73: CFX block

In this section, each subsection of this CFX block is described in detail.

8.1.1 Geometry

The geometry was prepared in ANSYS SpaceClaim to generate a wind tunnel domain that encloses the rear wing of the Formula 1 car. Inside this domain, the focus is on the flow around the wing and the loads on its surface, so the model used in CFX corresponds to the inverse geometry of the solid rear wing.

This approach allows the analysis of the pressure distribution on the wing's surface, as well as the behaviour of the airflow in the region surrounding the rear wing. The wind tunnel dimensions were chosen to ensure that the far field boundaries are located sufficiently far from the wing while still resolving the fine flow features near the wing with a reasonable number of computational cells.

Figure 74 shows the domain as it appears in SpaceClaim after the subtraction. The geometry clearly represents the internal airflow volume, with the rear wing represented as a boundary surface where no-slip and wall functions are applied, while the rest of the domain represents the air flowing through the virtual wind tunnel.

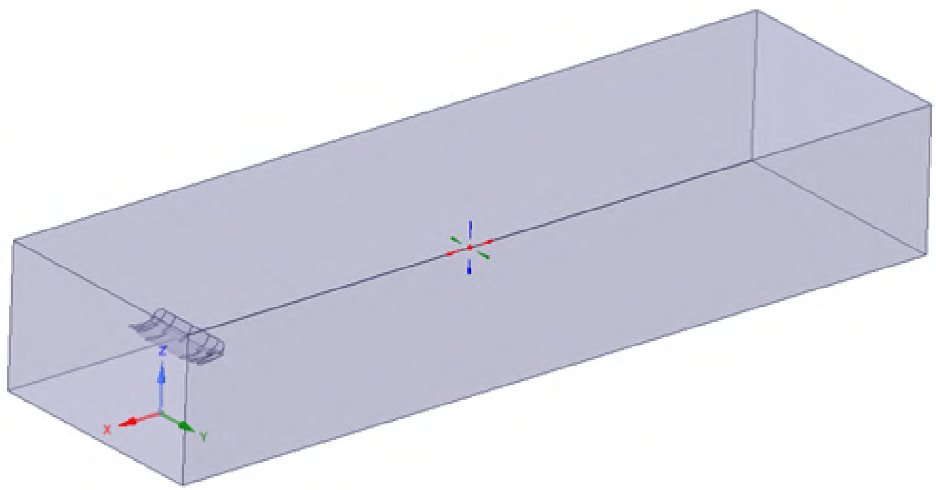

Figure 74: CFD model in Spaceclaim

8.1.2 Meshing

The meshing is performed using a patch conforming method with tetrahedrons. This approach is chosen because it provides a good balance between geometric accuracy and mesh quality, especially when dealing with curved surfaces and sharp edges.

In addition, a boundary layer inflation layer is implemented starting from the surface of the rear wing and extending toward the walls of the wind tunnel. This inflation consists of several prism layers adjacent to the wing surface, where the mesh cells are highly refined and grow progressively in size away from the wall. The purpose of this refinement is to resolve the steep velocity gradients in the boundary layer accurately, while maintaining a coarser mesh in regions far from the wing surface such as the outer parts of the tunnel. This strategy reduces the total number of elements and the overall computational size, which in turn reduces the simulation time without sacrificing the accuracy of the solution near the region of interest.

Figure 75 shows a cross-sectional view of the mesh at the center plane y=0 of the rear wing, where the inflation layers near the wing surface are clearly visible. The figure also illustrates the mesh quality in the surroundings of the wing, highlighting the smooth transition from the refined boundary layer region to the coarser mesh in the far-field areas of the domain.

The fine mesh observed on the rear wing surface is a consequence of the boundary layer refinement. Since large velocity gradients develop close to the wall, the mesh is locally refined with several inflation layers to capture these effects accurately. This results in much smaller elements near the wing surface, while the mesh becomes progressively coarser away from the wall.

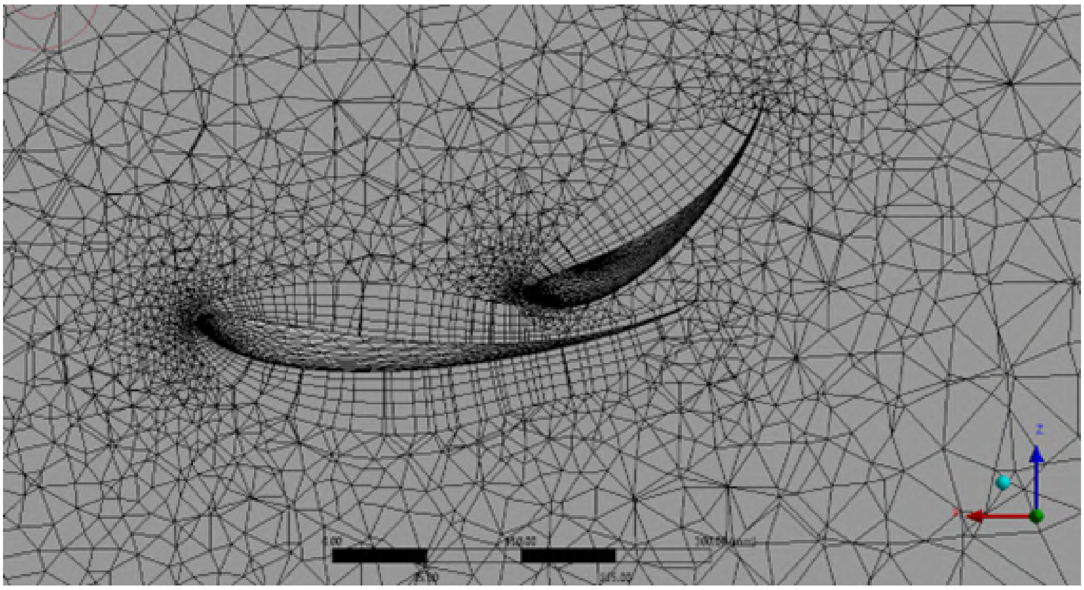

Figure 75: CFD mesh

Meshing validation: Skewness

To verify the **quality of the mesh**, a mesh control based on the skewness metric is implemented. Skewness is a standard mesh quality parameter used in CFD that measures how much a computational cell deviates from an ideal geometric shape, such as an equilateral triangle in two dimensions or a regular tetrahedron in three dimensions. It is defined on a scale from 0 to 1, where values close to 0 correspond to nearly ideal, well-shaped elements, while values closer to 1 represent highly distorted cells. Low skewness is preferred because it enhances numerical accuracy, solution stability and convergence behaviour. Skewness values below 0.5 are generally considered good.

Figure 76 shows the skewness distribution on the section plane located at the center plane y=0, highlighting regions where the mesh quality is highest and where more distorted elements are present.

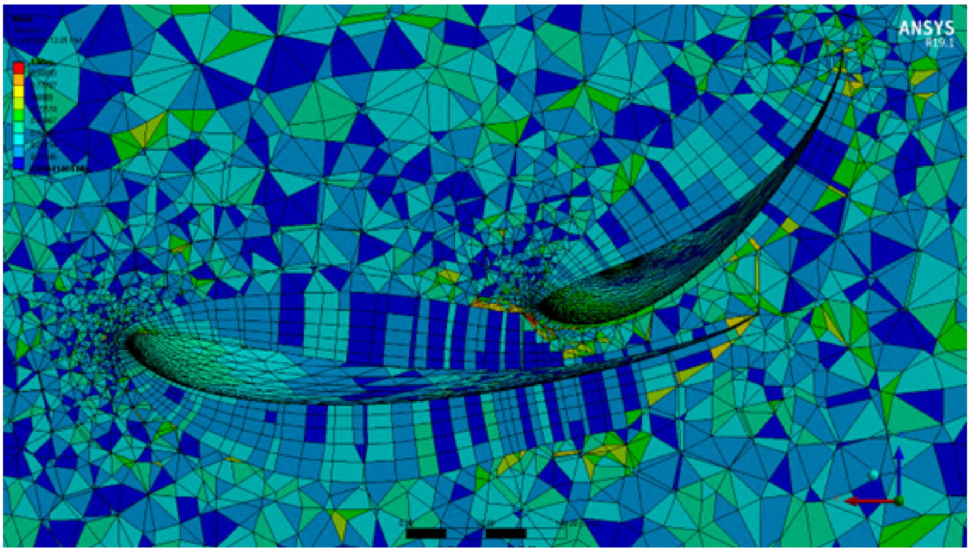

Figure 76: CFD mesh control: Skewness

Figure 77 presents the histogram of skewness values across the entire mesh, demonstrating that the majority of elements fall within the range from 0.15 to 0.45. This distribution indicates that the mesh is of high quality overall, with a large proportion of well-shaped cells and very few highly distorted elements, which validates its suitability for the subsequent CFD analysis of the rear wing.

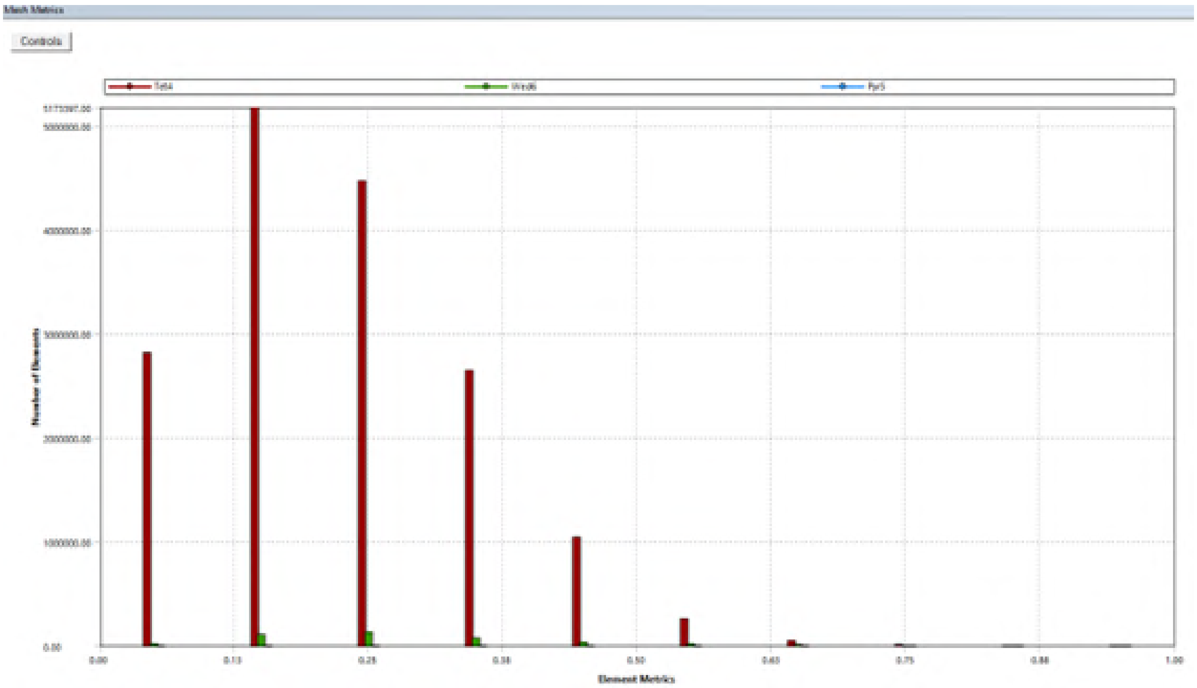

Figure 77: Skewness values

Meshing validation: grid convergence index

The objective of the grid convergence study is to verify that the numerical discretization error is within the asymptotic range of convergence, ensuring that the computed solution is independent of mesh resolution. Mesh sensitivity analyses are conducted by systematically refining the computational grid and evaluating key aerodynamic quantities such as drag force, downforce, and lift-to-drag ratio. The Grid Convergence Index (GCI), developed by Roache [ROAC98] and based on Richardson extrapolation [YOUN91], provides a rigorous, quantitative measure of discretization uncertainty.

Three successively refined meshes are generated with nominal characteristic sizes h_1, h_2, and h_3 (coarse, medium, and fine, respectively), where the characteristic mesh size is defined as:

$$h \approx (N^{-1})^{1/d}$$

with N representing the total number of cells and $d = 3$ for three-dimensional simulations.

The grid refinement ratios are computed as:

$$r_{21} = \frac{h_2}{h_1}, \quad r_{32} = \frac{h_3}{h_2}$$

For a given output quantity ϕ (lift-to-drag ratio L/D), the relative errors between solutions are:

$$\varepsilon_{21} = \phi_2 - \phi_1, \quad \varepsilon_{32} = \phi_3 - \phi_2$$

The apparent order of convergence p is then determined from:

$$p = \frac{\ln \left| \frac{\varepsilon_{32}}{\varepsilon_{21}} \right|}{\ln(r_{21})}$$

The Grid Convergence Index for each mesh pair is calculated as:

$$\mathrm{GCI}_{21} = F_s \frac{|\varepsilon_{21}|}{r_{21}^p - 1} \times 100\%, \quad \mathrm{GCI}_{32} = F_s \frac{|\varepsilon_{32}|}{r_{32}^p - 1} \times 100\% \tag{7}$$

where $F_s = 1.25$ is the safety factor recommended for three-mesh studies to ensure statistical confidence.

Table 26 presents the results of the mesh convergence study, in which three meshes are studied, in order to know if the results are affected by the quality of the mesh.

Table 26: Mesh convergence study

	Fine (20 mm)	**Medium (30 mm)**	**Coarse (40 mm)**
Element size (mm)	20	30	40
Elements	1,683,693	654,853	388,654
Nodes	3,152,451	1,321,330	840,331
Lift force (N)	6,821	6,826	6,833
Drag force (N)	1,616	1,617	1,619
Lift-drag ratio	4.2209	4.2214	4.2205

Table 27 shows the results of the grid convergence index study. The computed GCI values are all lower than 0.01 (1%), which confirms that the solution lies within the asymptotic range of convergence and is effectively independent of further mesh refinement. This low level of discretization uncertainty validates the fine mesh as representative of the continuum solution for subsequent aerodynamic and structural analyses.

Table 27: Grid Convergence Index (GCI) results

	Refinement ratio	
	$r_{1,2}$	$r_{3,2}$
e (%)	1.37	1.19
p	1.069	1.069
r^p	1.40	2.04
GCI (%)	0.23	0.63

Formula 1 cost cap

In Formula 1, the cost cap was introduced in 2021 to limit annual team spending, with the initial limit set at approximately €123 million. Aerodynamic development is also restricted by testing regulations, including 1,200 wind tunnel hours per year for each team, which further limits the amount of numerical and experimental iteration possible.

Formula 1 teams do not have a fixed maximum number of CFD simulations, but their activity is limited by the amount of computational resource allocated to them, expressed in Allocation Unit hours (AUh). As a result, the number of simulations that can be performed depends on the complexity and duration of each case, since a single high-fidelity run may consume a significant fraction of the available compute budget. This makes mesh design particularly important, because achieving a highly optimized mesh is possible, but it usually requires additional computational time; therefore, a compromise between mesh quality and computational cost is necessary.For this reason, this design does not try to achieve the best mesh possible, but aims for achieving a good quality mesh refined enough to capture the important flow features accurately, especially near the rear wing and in the boundary layer, while still remaining efficient enough to fit within the available simulation resources.

8.1.3 Setup

The computational domain is set up with the following boundary conditions:

- At the **inlet boundary**, the type is set to Inlet with a boundary velocity of 98.1 m/s, representative of the car speed at the end of the main straight, where the analysis is focused. The inlet velocity is assumed uniform and normal to the inlet face.

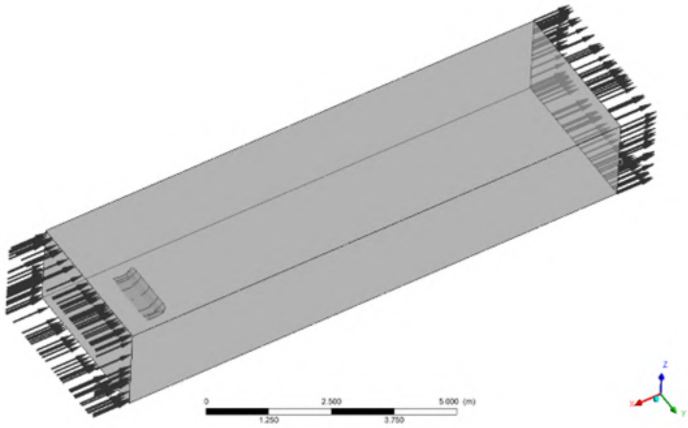

Figure 78: CFD setup

- The **top wall** and the **side walls** of the wind tunnel are defined as Free Slip Wall boundary conditions. This setting allows the flow to slide along these surfaces with zero tangential shear stress, so that the wall does not slow down the flow artificially.

- The **surface of the rear wing** is defined as a No-Slip Wall, with a physical wall boundary condition. This means that the velocity of the flow at the wing surface is set to zero relative to the wall, and the wall roughness and thermal conditions are set according to standard isothermal wall assumptions.

- At the **outlet boundary**, the type is set to Outlet with a relative pressure fixed at 0 Pa. A blending factor of 5 per cent is used for the pressure outlet, which means that the solver uses a small proportion of the backflow pressure to stabilize the solution, while maintaining a predominantly fixed pressure condition.

- The **ground surface** is also defined as a No-Slip Wall, with a zero velocity condition relative to the ground. This accounts for the interaction between the wing wake and the ground, as well as the influence of the ground plane on the overall flow field and pressures around the lower part of the wing.

For the convergence control, the maximum number of iterations is set to 100 and the residual target is set to RMS 0.0001. This low residual target ensures that the solution is sufficiently converged and that the solver stops only when all main equations (mass, momentum, turbulence) have reached a small, steady level, confirming that a stable and accurate steady-state solution has been achieved.

8.1.4 Solution

The residuals plot, shown in figure 79 shows that all main equations (mass, momentum, energy, turbulence) converge steadily to level below 10e-4, indicating that the solver has reached a stable and well-resolved numerical solution. This confirms that the mesh, boundary conditions and model setup capture the physics of the flow around the rear wing in a consistent and robust manner.

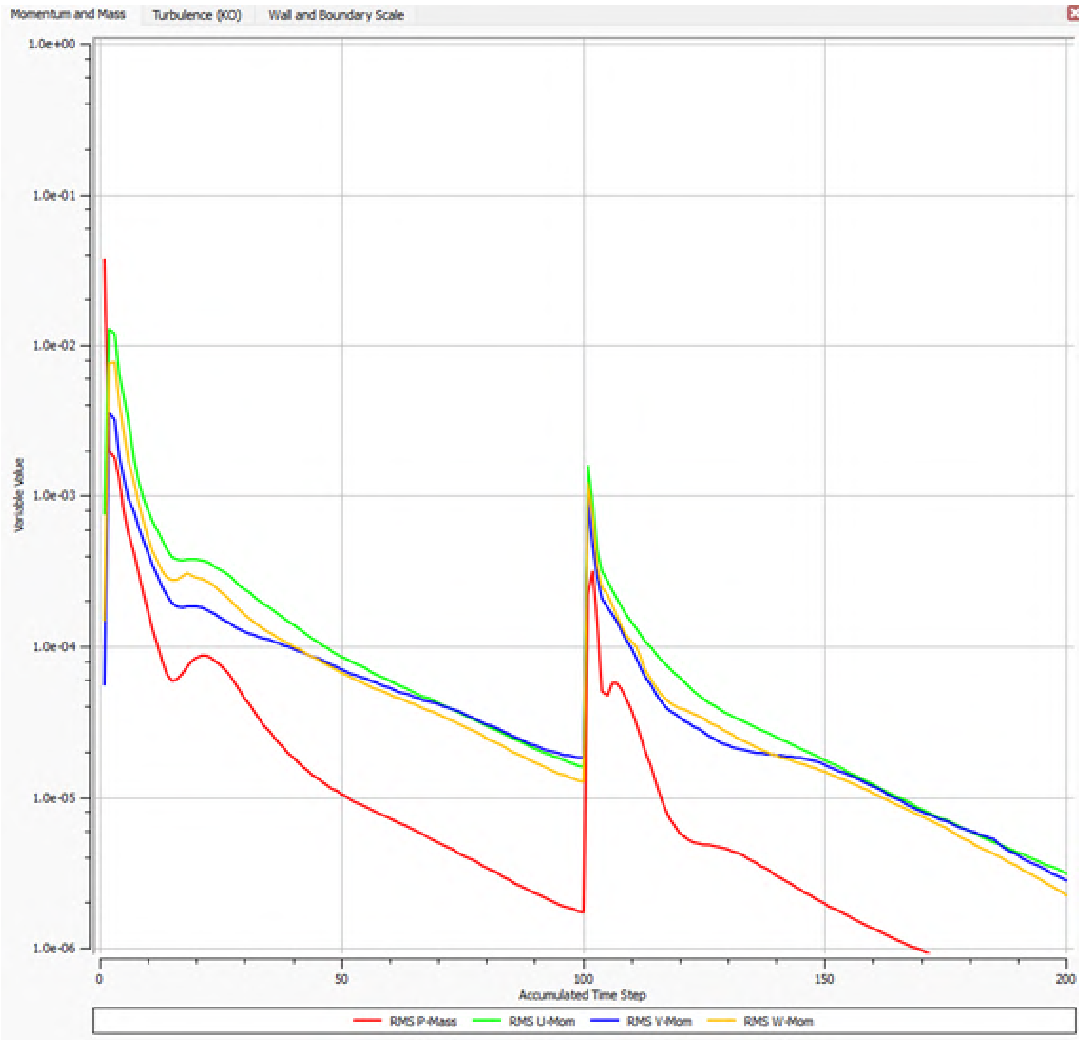

Figure 79: CFD residuals

8.1.5 Results

Forces

Figure 80 shows the convergence history of the aerodynamic forces acting on the rear wing. The plot demonstrates that both the drag and lift components reach a stable, converged state after sufficient iterations, confirming the numerical reliability of the solution.

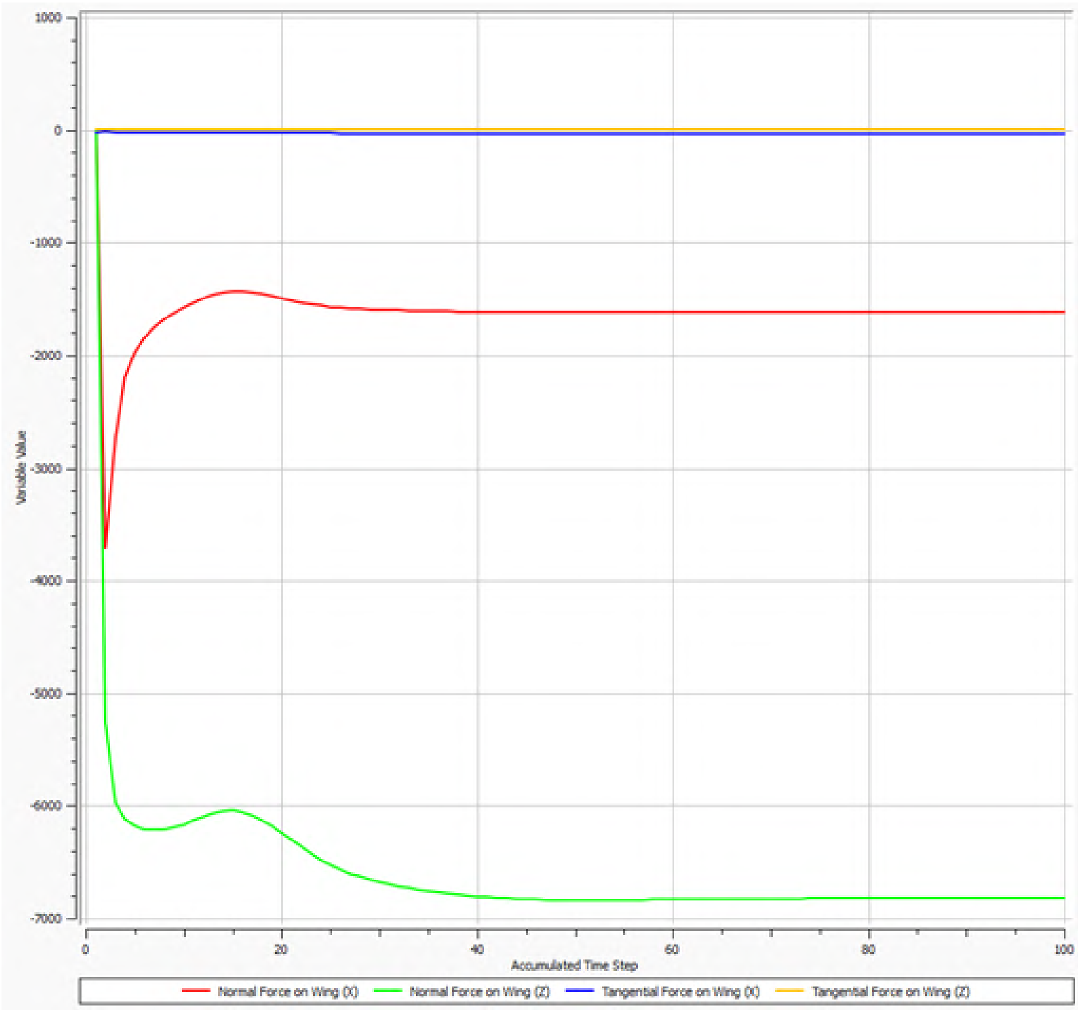

Figure 80: CFD forces results

The converged results indicate that the rear wing generates a drag force of 1616 N and a downforce (negative lift) of 6821 N at the reference speed of 98.1 m s. This yields an aerodynamic efficiency ratio of downforce-to-drag of 4.22, which represents a good compromise for a high-speed straight configuration such as the Monza main straight.

Pressure Distribution on the Wing

The pressure distribution plots on the wing surface are shown in figure 81 and figure 82.

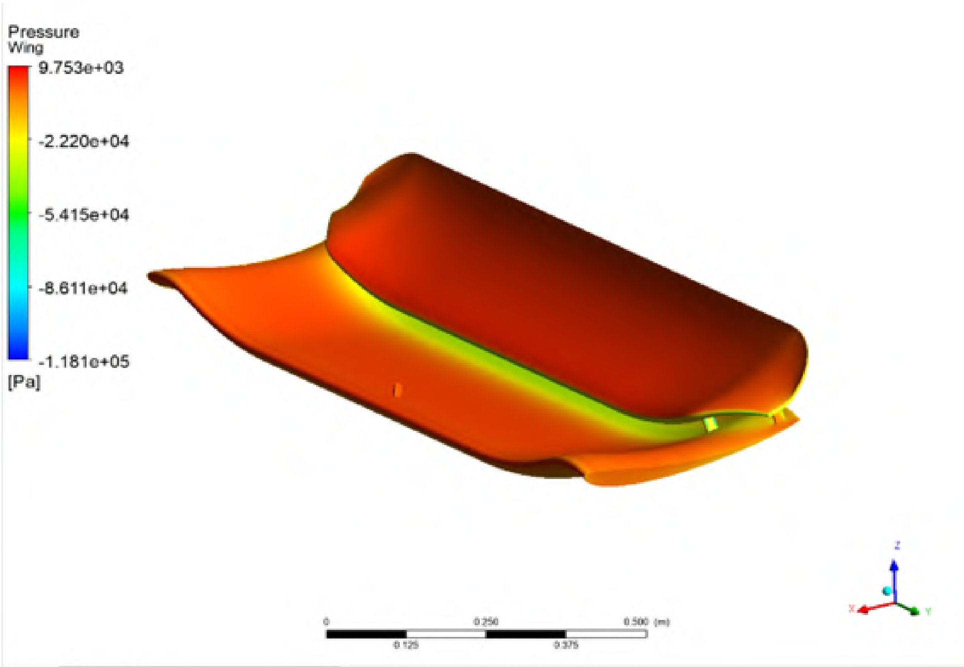

Figure 81: Pressure distribution view 1

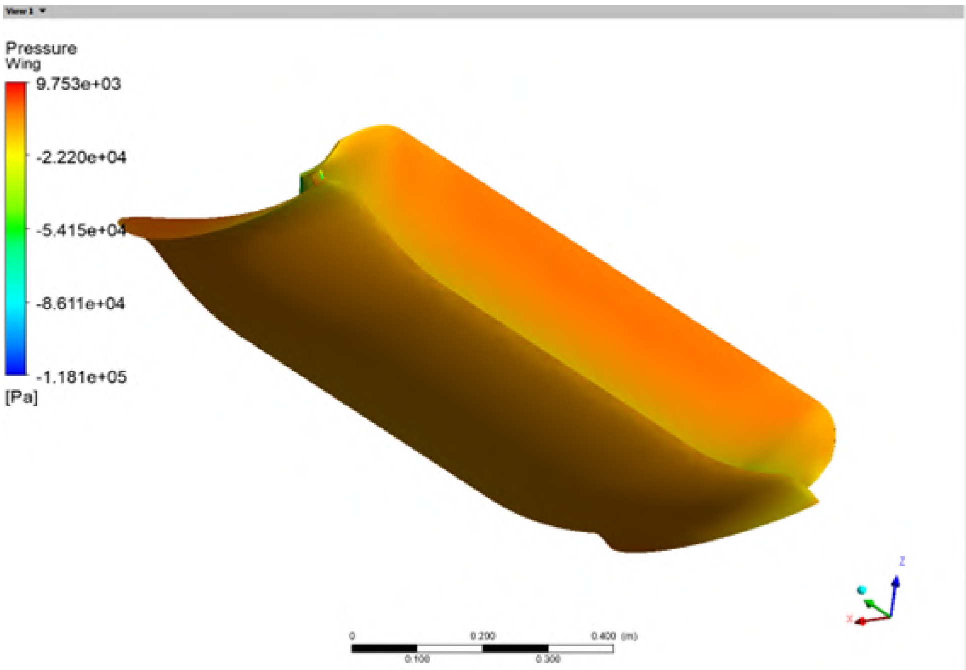

Figure 82: Pressure distribution view 2

The pressure distribution plots clearly show the classic behavior of a highly loaded rear wing working in a low-downforce, high-speed setup, with a clear contrast between a region of higher pressure on the lower surface and an extended low pressure region on the upper surface:

- On the **lower surface** (pressure side), a region of high pressure is observed, especially in the mainplane and flap, contributing significantly to the overall downforce of the wing.
- On the **upper surface** (suction side), a large area of low pressure appears, particularly over the flap and mainplane, where the flow accelerates strongly.
- The **pressure gradient** is steepest near the leading edge and along the flap, indicating regions of high aerodynamic loading.
- Near the trailing edge, the pressure gradually recovers, but the suction persists, confirming that the wing is still generating a substantial amount of downforce even in a low-drag configuration.

Flow Structures and Streamlines

The three dimensional streamlines around the wing, shown in figure 83, ilustrate that the incoming flow remains largely attached over the main surfaces of the rear wing, particularly over the pressure side, with a clean acceleration over the suction side near the trailing edge. In the longitudinal views, the wake behind the wing is well defined and relatively thin, indicating an efficient generation of downforce with limited separation. Controlling the wake behind a Formula 1 rear wing is essential because it has a direct influence on both aerodynamic performance and the flow development downstream of the car. A properly designed rear wing generates vortices that help organize the airflow and manage the wake structure, allowing the wing to produce downforce more efficiently. These vortices also add energy to the flow near the wing tips and in the wake region, which helps delay flow separation and reduce the extent of the low-energy turbulent region behind the wing.

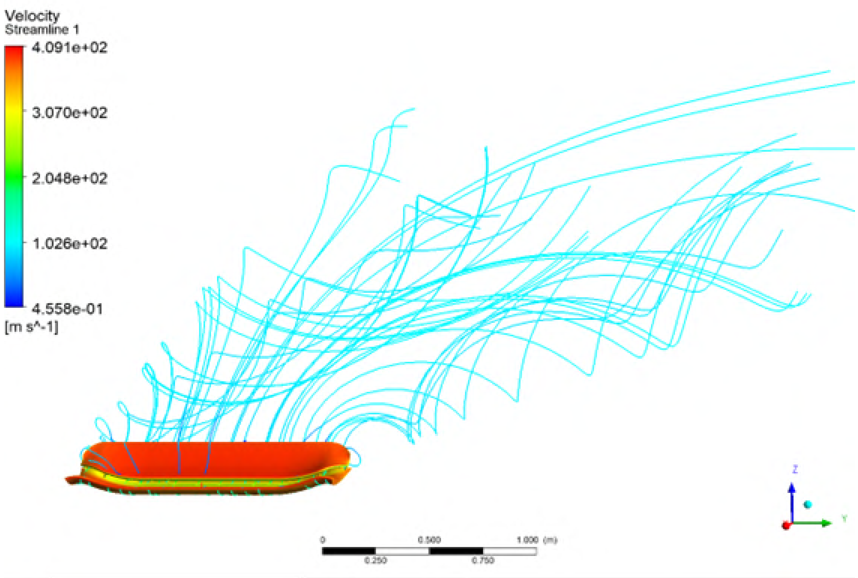

Figure 83: Streamline view 1

The front view figure 84 reveals two strong tip vortex structures shed from the lateral extremities of the wing, a typical feature of highly loaded lifting surfaces; these vortices roll up downstream and dominate the far wake behaviour.

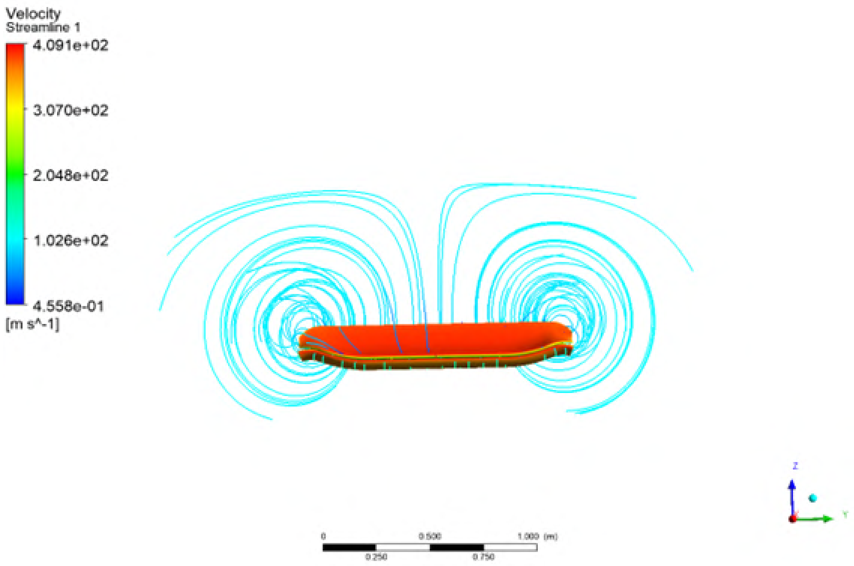

Figure 84: Streamline front view

In the central plane visualisations, figure 85 and figure 86, the streamline patterns confirm that the flow is mostly attached over the mid span region, with a smooth curvature of the streamlines and an organised wake developing behind the wing. This suggests that the selected angle of attack and profile design allow the wing to operate within an efficient aerodynamic regime under the Monza high speed condition.

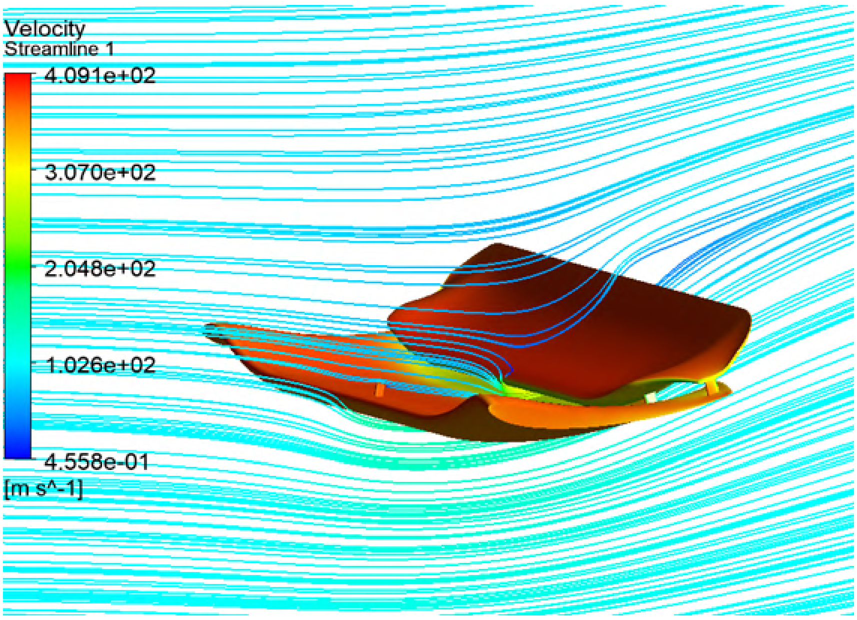

Figure 85: Streamline plane Y=0 view 1

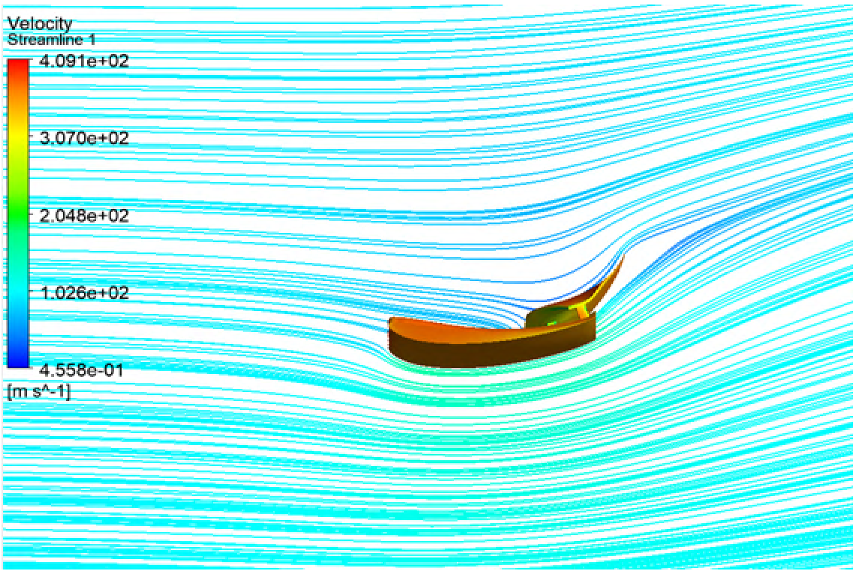

Figure 86: Streamline plane Y=0 view 2

9 Fluid–Structure Interaction (FSI)

The Fluid-Structure Interaction (FSI) analysis couples the structural and fluid domains to capture aeroelastic deformation effects on the composite spoiler under aerodynamic loading. Implemented in ANSYS Workbench, this multiphysics simulation integrates ANSYS Fluid Flow (CFX) for computational fluid dynamics (CFD) with ANSYS Mechanical for finite element analysis (FEA). The solvers operate independently but exchange data like pressure and force from fluid to structure, and displacement from structure to fluid through Workbench's data transfer framework. This partitioned approach leverages each solver's domain-specific numerical strengths while accurately resolving coupled aeroelastic phenomena such as camber variation and angle-of-attack changes due to deformation [BANG22]. Interface data transfer conserves virtual work, ensuring physical consistency and energy balance across domains, with conservative force mapping and consistent displacement interpolation at wet surfaces.

The complete Ansys Workbench workflow is shown in figure 87. For the fluid–structure interaction analysis, a Static Structural block is added that receives input from three sources: the ACP-Pre composite layup definition (ply orientations, thicknesses, and material properties), the Mechanical APDL structural model (including Rohacell core and titanium supports), and the Fluid Flow (CFX) aerodynamic solution (pressure and shear stress distributions). This integrated setup enables accurate load transfer from the aerodynamic analysis to the structural model while maintaining full fidelity of the composite laminate definition.

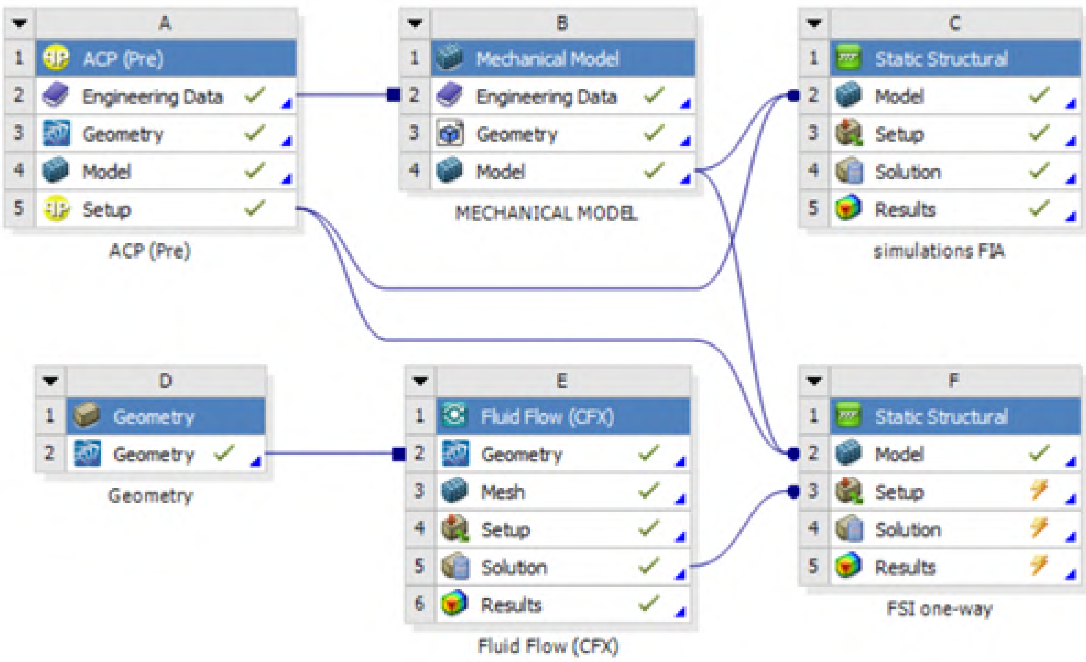

Figure 87: ANSYS workflow

FSI analysis are classified into two coupling approaches based on interaction strength and computational requirements, which are shown in figure 88:

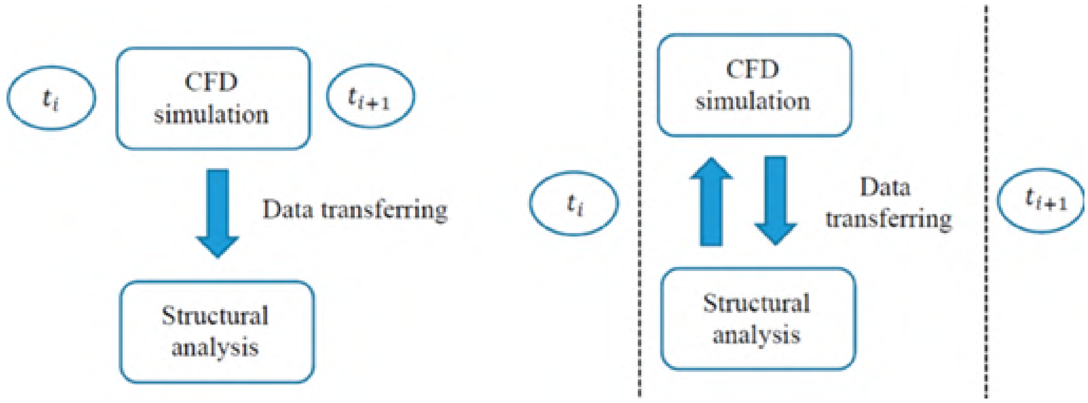

Figure 88: One way (left) vs two way (right)

One-way FSI

Employs unidirectional coupling between CFD simulations and Structural simulations. This method is suitable for weakly coupled problems where structural deformations minimally affect the surrounding flow field. The mechanical model does not modify the fluid flow, but the fluid flow modifies the mechanical model. This computationally efficient method is around 10 faster than two way FSI, saving computational cost.

Two-way FSI

Addresses strongly coupled interactions through bidirectional, iterative coupling controlled by ANSYS System Coupling. In this method, transient structural displacements deforms the fluid volume mesh and prompting pressure recalculation until force-displacement convergence per timestep. This approach captures feedback effects like flow field alterations from camber increase or flutter onset, essential for highly compliant structures.

For this study, one-way FSI was selected given the spoiler's high stiffness-to-weight ratio and steady cruise conditions (Mach < 0.3). Achieving faster simulation times and accurate results.

9.1 Fluid–Structure Interaction Implementation in Ansys Workbench

The FSI analysis workflow is implemented within the Ansys Workbench environment using a one-way coupled approach, where aerodynamic loads from the CFX solution are mapped onto the structural model for static analysis.

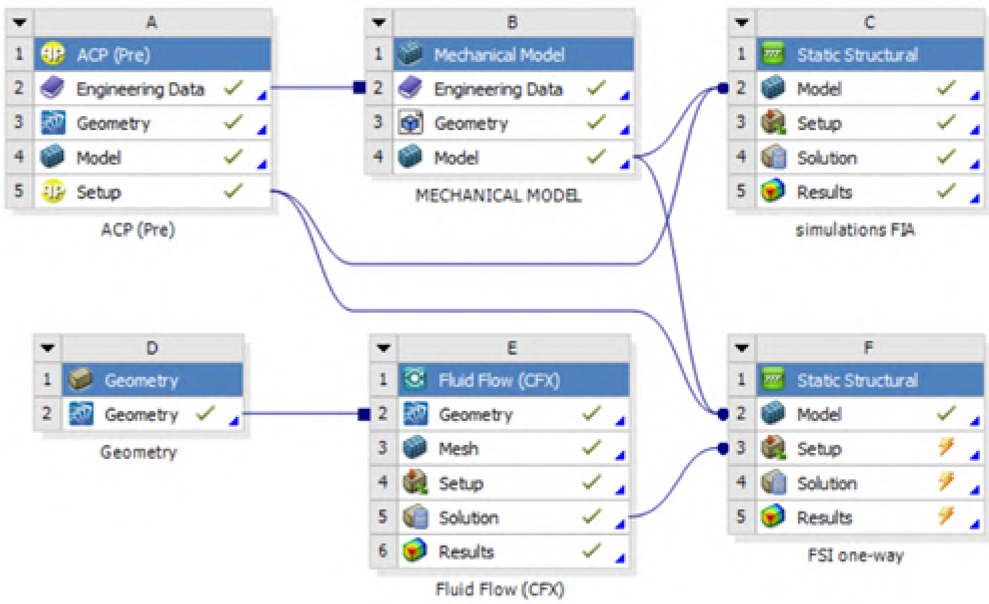

Figure 89: FSI block

9.1.1 Structural Model

The mechanical APDL model receives the composite layup definition directly from Ansys ACP-Pre, including all ply orientations, thicknesses, and material properties. The model incorporates the Rohacell foam core for sandwich panels and titanium alloy supports at the mounting points, reflecting the actual manufacturing stack-up of a Formula 1 rear wing assembly.

9.1.2 Load Transfer

The static structural setup receives aerodynamic pressure and shear stress data from the Fluid Flow (CFX) analysis corresponding to the Monza high-speed straight condition (98.1 m/s). These distributed loads are mapped onto the composite surfaces of the rear wing using Ansys surface-to-surface load transfer. The pressures act as static body forces for the structural analysis, with conservative load combination applied to capture peak aerodynamic loading.

Figure 90 shows the pressure stress data from the CFX analysis corresponding to the CFD case.

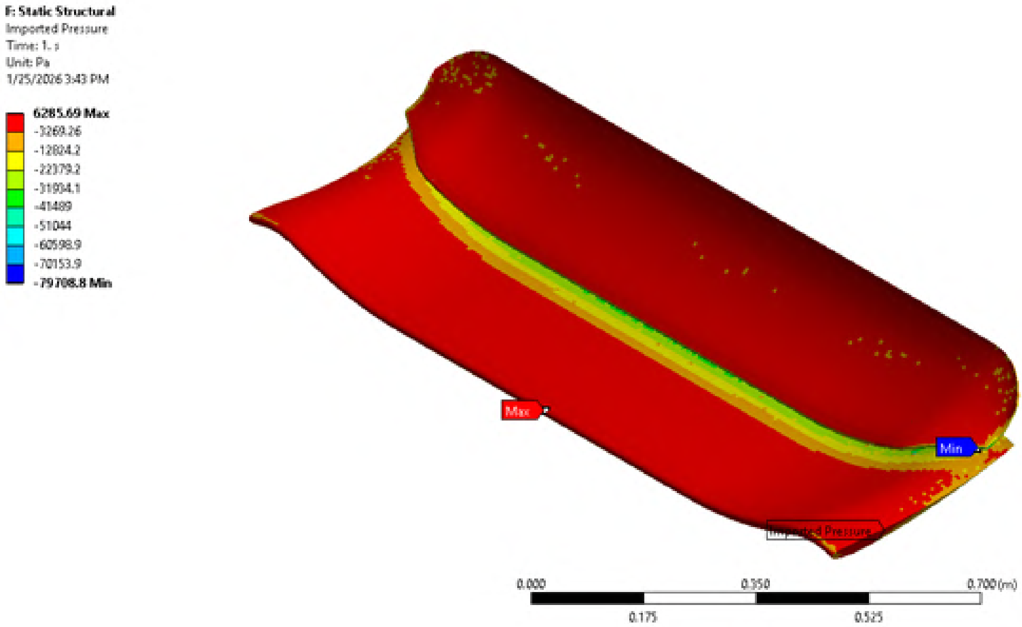

Figure 90: Mapped pressure distribution from CFX to structural surfaces

9.1.3 Results

The result of the FSI analysis is shown in figure 91, in which the maximum displacement corresponds to the center plane of the DRS, with a maximum displacement of 26.26 mm. This value needs to be lower than 20 mm to achieve the design target.

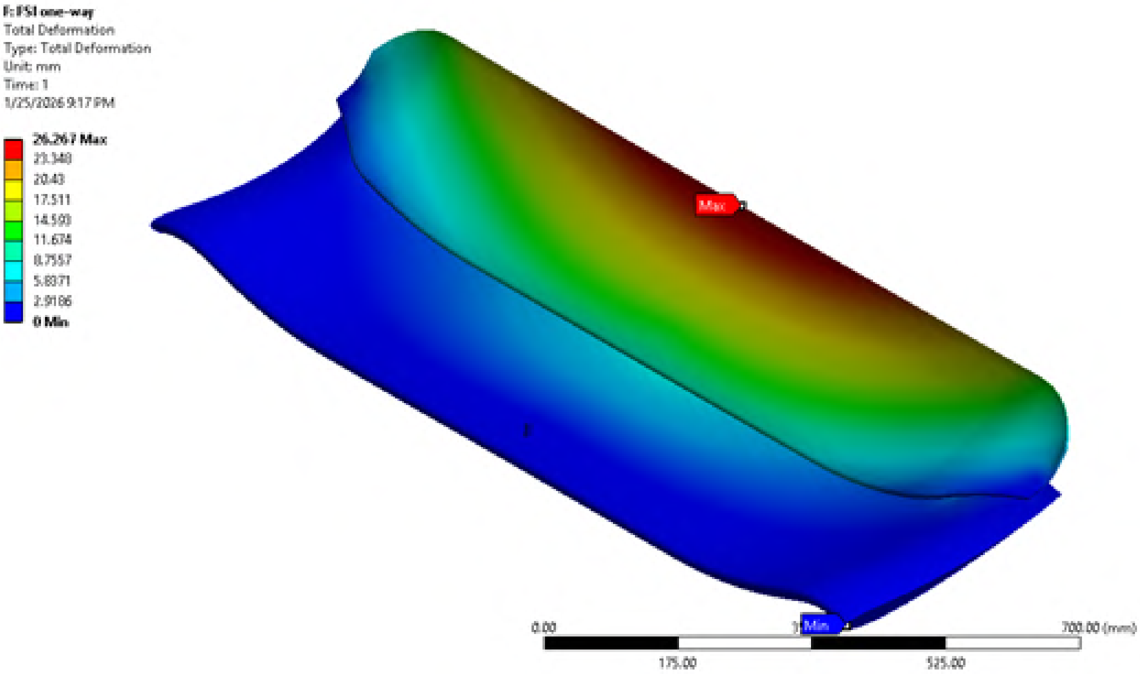

Figure 91: FSI results

10 Modal Response Analysis

This chapter presents the modal response analysis used to characterize the dynamic behavior of composite laminates. Modal analysis is critical for aeroelastic design because it identifies natural frequencies and mode shapes that determine flutter boundaries and aeroelastic stability margins.

10.1 Modal response analysis workflow

Figure 92 shows the workflow where the modal analysis block receives the ACP-preprocessed composite model with the stacking sequence, ply orientations and orthotropic properties, and also receives the Mechanical model setup with the geometry, mesh and boundary conditions.

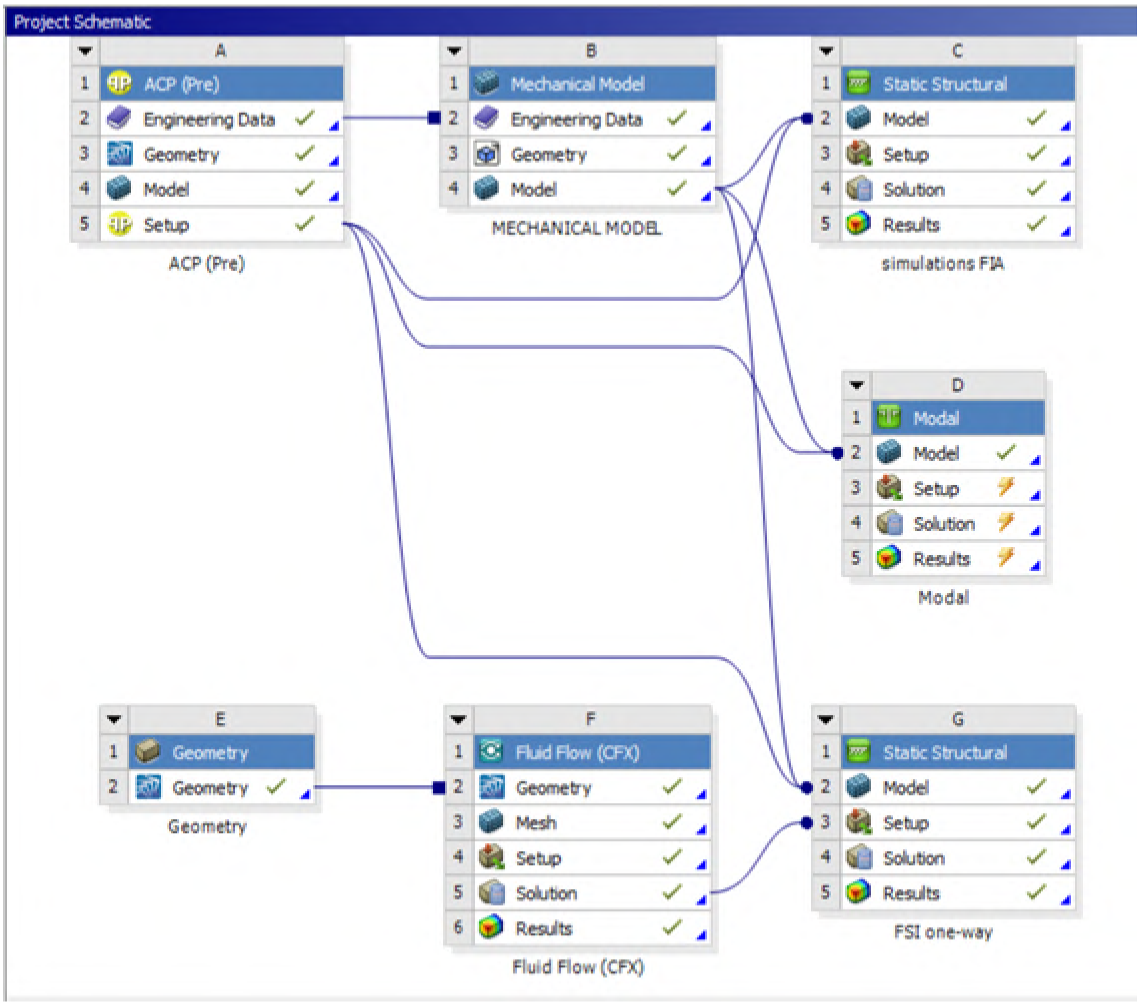

Figure 92: Modal analysis workflow integrating ACP composite definitions with Mechanical modal solver.

10.2 Modal response analysis results

The natural frequency f_n represents the oscillation rate at which a structure vibrates when disturbed from equilibrium, governed by the fundamental relation:

$$f_n = \frac{1}{2\pi}\sqrt{\frac{k}{m}} = \frac{1}{2\pi}\sqrt{\frac{k}{m}}$$

where k is structural stiffness and m is modal mass. For a structure like a F1 rear wing with a fixed root and a free tip, the first bending mode frequency scales with:

$$f_1 \propto \sqrt{\frac{EI}{mL^4}}$$

with EI flexural rigidity, m mass per unit length, and L span. This L^4 dependence explains why short, stiff F1 wings achieve high frequencies (74.78 Hz) despite downforce loading.

The first 6 natural modes are analyzed because these modes provide insight into the dynamic behavior, capturing mainly all of the structural energy under operational loading, the frequency of each mode is shown in table 34.

Table 28: Natural frequencies.

Mode	Description	f (Hz)
1	1st bending	64.872
2	1st torsion	148.39
3	2nd bending	189.38
4	1st transverse bending	236.79
5	2nd torsion	247.47
6	3rd bending	286.02

Mode 1 (1st bending, 74.78 Hz) corresponds to the fundamental vertical deflection of the wing, with maximum displacement at the tip while the root remains fixed. This mode is the most critical for aeroelastic flutter as it dominates the low-frequency dynamic response during high-speed operation. The frequency of the fist bending mode is superior to the minimum design target of 50 Hz.

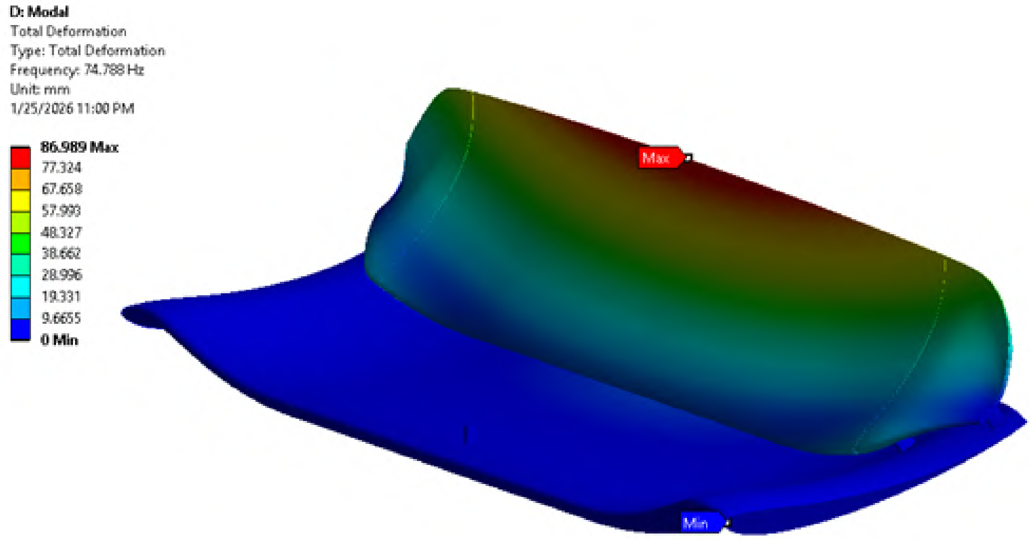

Figure 93: Response mode 1

Mode 2 (1st torsion, 158.66 Hz) exhibits twisting motion where the leading edge moves upward while the trailing edge moves downward, creating a change in angle of attack along the span. Modes 1 and 2 are critical for the design due to their strong coupling potential in classical flutter instability.

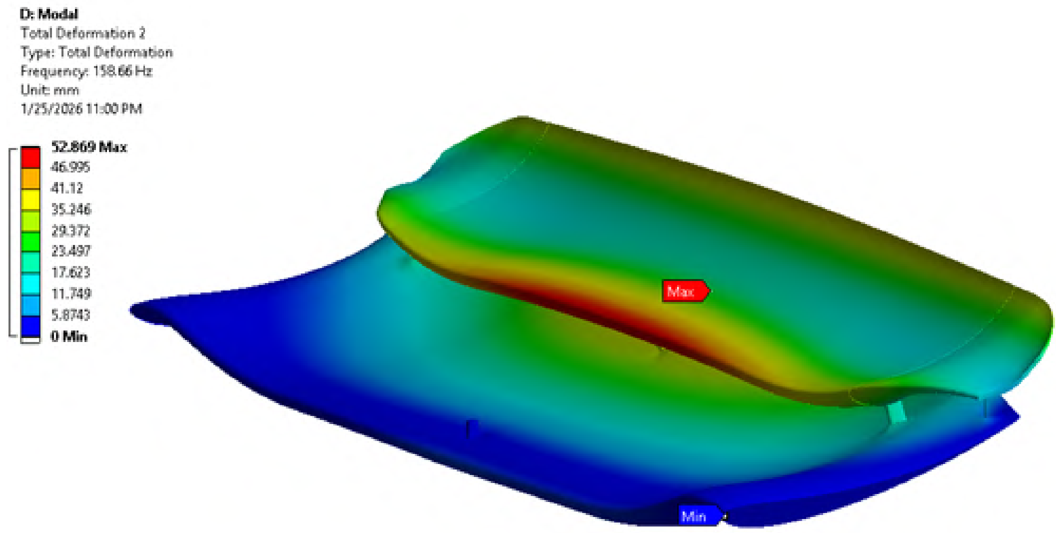

Figure 94: Response mode 2

Mode 3 (2nd Bending, 200.76 Hz) represents the first harmonic of vertical bending, with a nodal line approximately at mid-span separating two half-sine deflection curves.

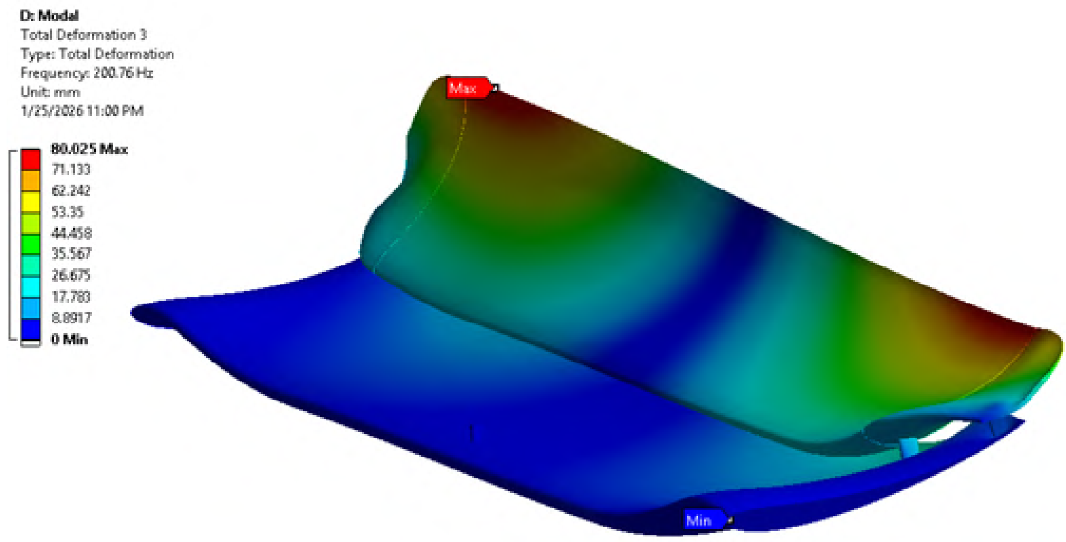

Figure 95: Response mode 3

Mode 4 (1st Chordwise Bending, 236.79 Hz) corresponds to streamwise deflection along the chord, critical for assessing leading/trailing edge structural integrity under aerodynamic pitching moments.

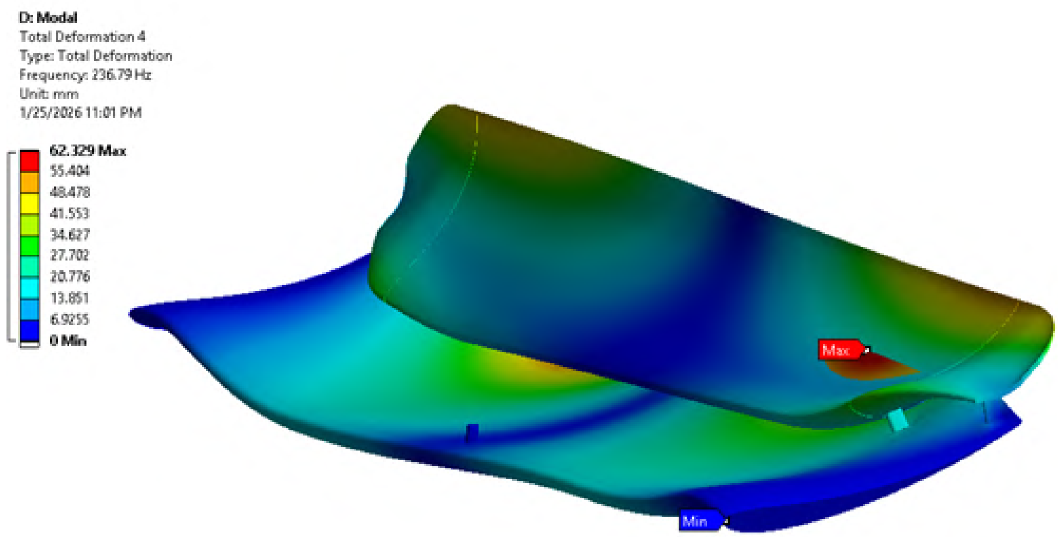

Figure 96: Response mode 4

Mode 5 (2nd Torsion, 247.47 Hz) shows the second torsional harmonic with two nodal lines along the span, contributing to higher-order aeroelastic coupling under yaw loading.

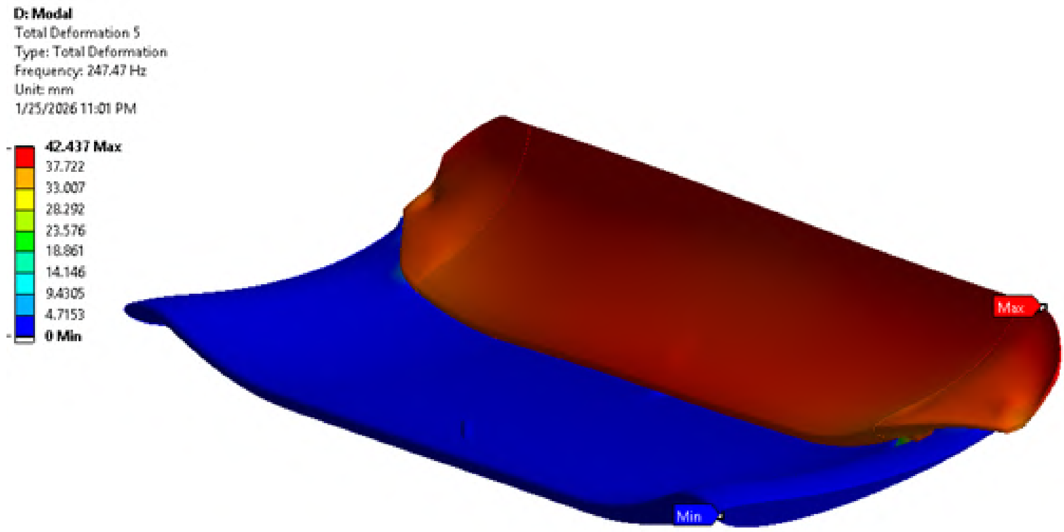

Figure 97: Response mode 5

Mode 6 (3rd Bending, 286.02 Hz) represents the second harmonic of vertical bending with two nodal lines, completing characterization of primary elastic deformation mechanisms.

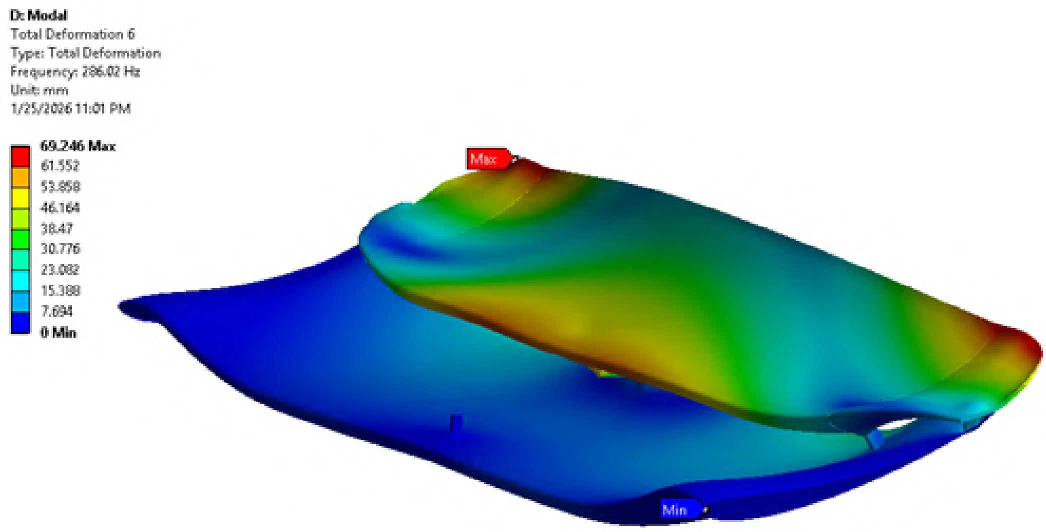

Figure 98: Response mode 6

11 Optimization

This chapter presents the optimization study evaluating the influence of ply angle θ and number of plies n on the maximum deformation of the DRS mechanism under the reference loading case. The objective was to identify laminate configurations achieving the target deformation while minimizing mass.

- **Objective 1**: Minimize the total rear wing mass minimizing the number of CFRP layers.
- **Objective 2**: Achieve maximum DRS displacement $\approx$ 20 mm.
- **Constraint**: minimum 4-ply configuration to validate the FIA technical regulations.
- **Variable**: number of layers and ply angles.

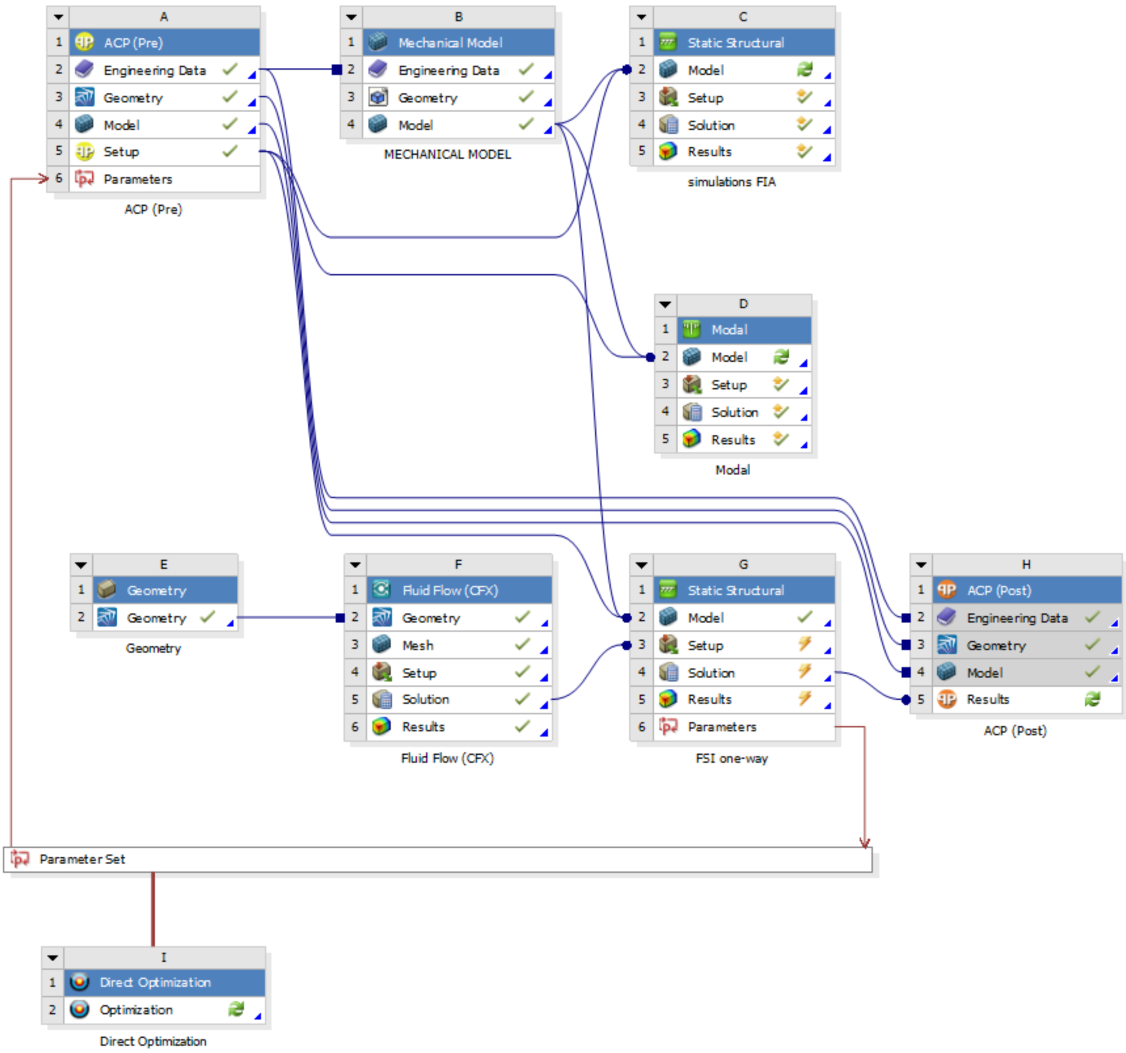

Figure 99: Optimization conections

Figure 99 shows the conections made between blocks to do the multiobjective optimization. ANSYS DesignXplorer was employed with direct optimization methodology, automatically generating a parameter set from ACP-predefined variables and executing design of experiments (DOE). The variable layer angle was parameterized while importing the one-way coupled FSI load case for aeroelastic response evaluation.

11.1 Objective 1: minimize total mass

The goal is to know how many layers of CFRP are needed to achieve the desired maximum displacement, and minimize the number of layers in order to minimize the total weight. Twelve stacking sequences were analyzed: four configurations with 4 plies, four with 6 plies, and four with 8 plies. Each configuration was systematically extended to higher ply counts while maintaining ply angle relationships, creating quasi-symmetric laminates. The study systematically evaluates four fundamental angle configurations across three thickness levels.

Table 29 compares the maximum deformation and mass of the 12 layups proposed in the first optimization stage.

Configuration	**Deformation**	**Mass**
4 plies		
1 [woven 0 ud 0,ud 45, ud 0]	22.92 mm	316.2 g
2 [woven 0, ud 0, ud 45, ud 0]	22.49 mm	316.2 g
3 [woven 0, ud 0, ud 90, ud 0]	17.95 mm	316.2 g
4 [woven 0, ud 0, ud 45, ud -45]	21.09 mm	316.2 g
6 plies		
5 [woven 0, ud 0, ud 45, ud 0, ud -45, ud 0]	19.98 mm	474.3 g
6 [woven 0, ud 0, ud 45, ud 0, ud 45, ud 0]	21.26 mm	474.3 g
7 [woven 0, ud 0, ud 0, ud 90, ud 0, ud 0]	17.61 mm	474.3 g
8 [woven 0, ud 0, ud 45, ud 90, ud 45, ud 0]	16.85 mm	474.3 g
8 plies		
9 [woven 0, ud 0, ud 45, ud 0, ud 0, ud 45, ud 0, woven 0]	17.96 mm	632.4 g
10 [woven 0, ud 45, ud 0, ud 45, ud 45, ud 0, ud 45, woven 0]	17.62 mm	632.4 g
11 [woven 0, ud 0, ud 45, ud 90, ud 90, ud 45, ud 0, woven 0]	13.53 mm	632.4 g
12 [woven 0, ud -45, ud 0, ud 45, ud 45, ud 0, ud -45, woven 0]	16.39 mm	632.4 g

Table 29: Maximum DRS deformation for each configuration

11.1.1 Maximum deformation per number of plyes

Figures 100–102 show deformation results grouped by ply count (4, 6, and 8 layers) for each configuration.

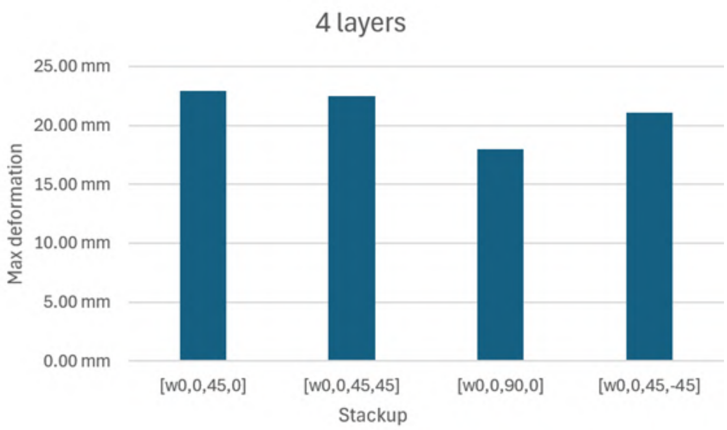

Figure 100: Maximum deformation: 4-ply configurations.

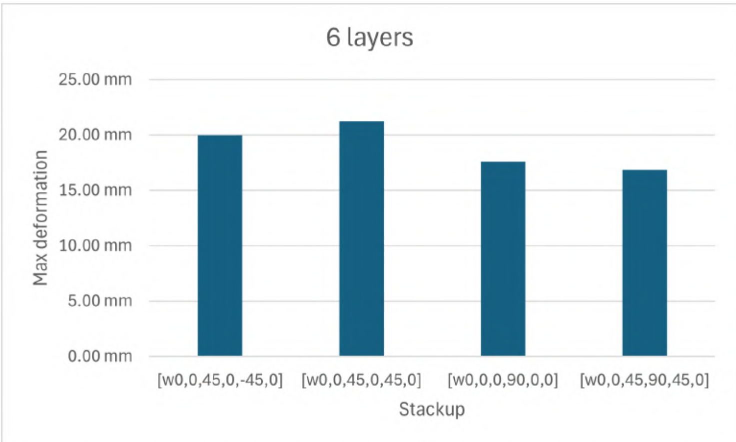

Figure 101: Maximum deformation: 6-ply configurations.

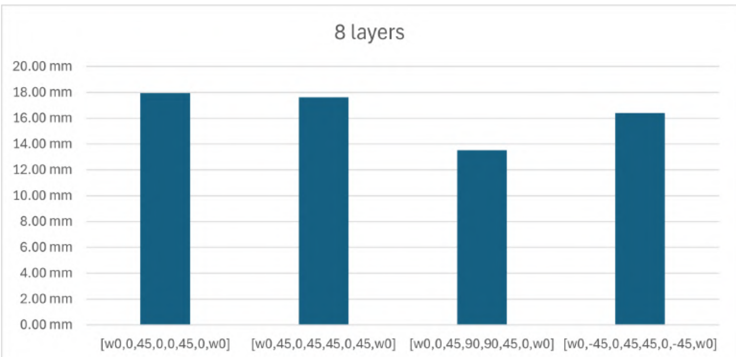

Figure 102: Maximum deformation: 8-ply configurations.

11.1.2 Maximum deformation per configuration

Configuration A $[0/0/45/0]_s$ provides high longitudinal stiffness from three 0° layers, with the central +45° ply adding shear and torsional resistance.

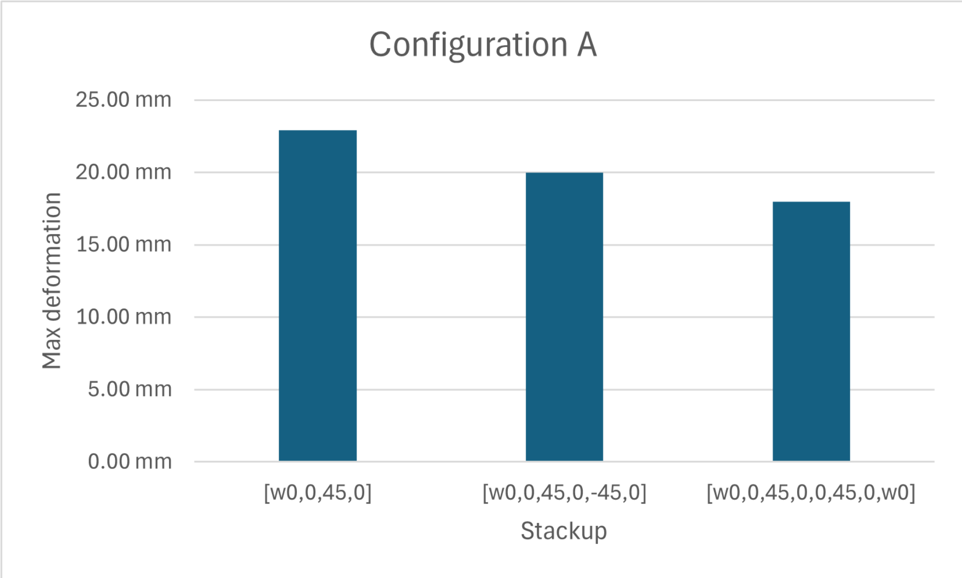

Figure 103: Configuration A: Deformation vs. ply count.

Configuration B $[0/0/45/45]_s$ offers more balanced shear and torsional rigidity compared to Configuration A.

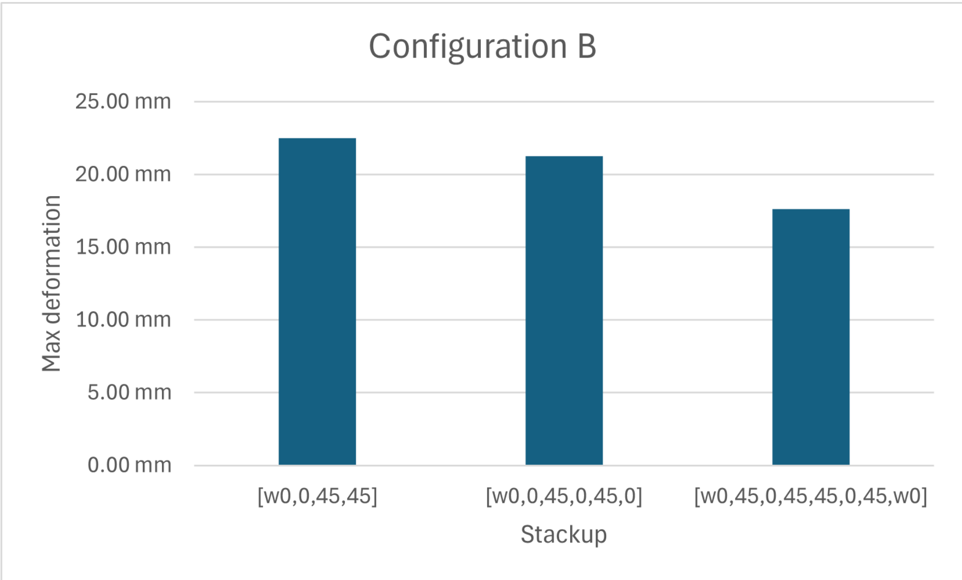

Figure 104: Configuration B: Deformation vs. ply count.

Configuration C $[0/0/90/0]_s$ prioritizes maximum longitudinal stiffness with targeted transverse reinforcement. The three 0° layers provide excellent resistance to deflection and buckling under downforce, maintaining airfoil camber at high speeds.

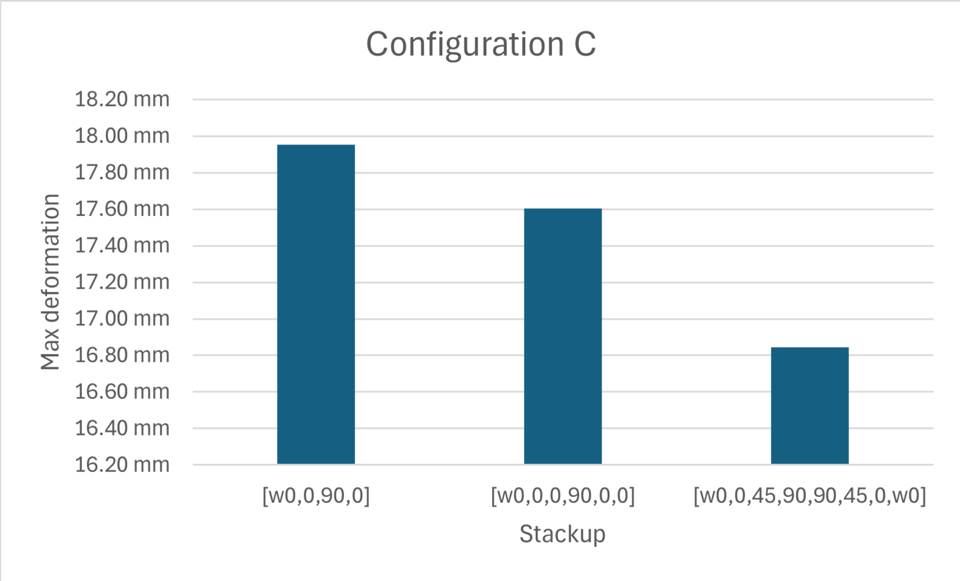

Figure 105: Configuration C: Deformation vs. ply count.

Configuration D $[0/0/45/-45]_s$ balances bending, torsion, and shear resistance under dynamic downforce loads.

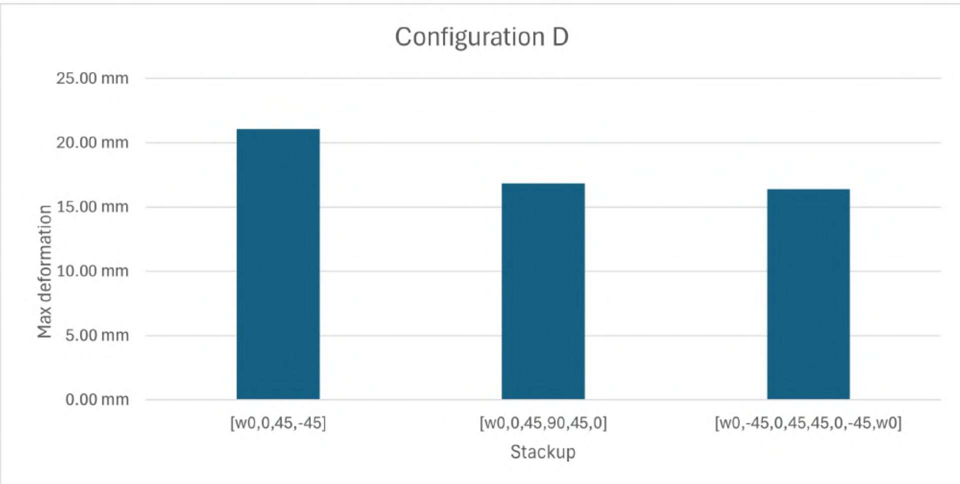

Figure 106: Configuration D: Deformation vs. ply count.

Figure 107 combines these results, illustrating the clear trend: deformation decreases nonlinearly with increasing ply count across all configurations. Configurations A and D exhibit concave curvature, while B and C show convex behavior. This analysis identifies configurations achieving deflections between 16–23 mm across 4–8 plies, enabling tailored deflection response.

Configuration C exhibits the smallest difference in maximum deflection between 4 and 8 layers (only 1 mm), compared to nearly 4 mm for the others. This behavior results from its $[0/0/90/0]_s$ stackup, which lacks ±45° fibers and thus maintains superior longitudinal stiffness across all thicknesses.

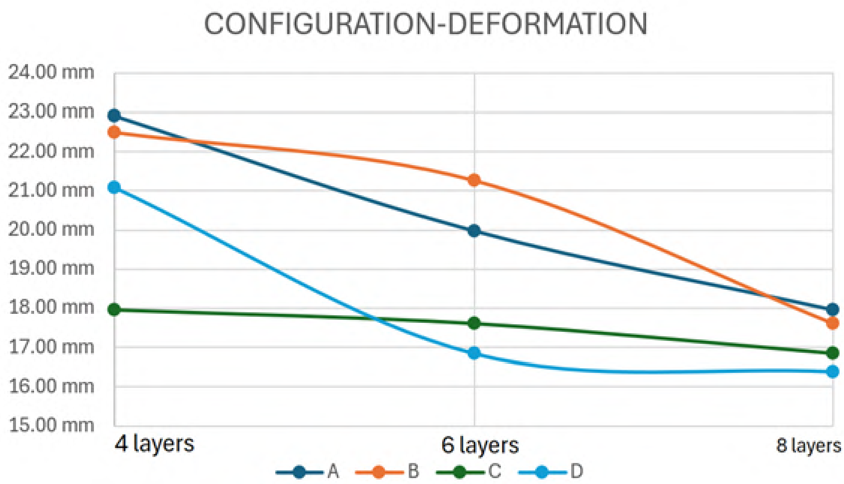

Figure 107: Deformation trends across configurations and thicknesses.

Based on the design requirements targeting minimum mass, a design with four layers was chosen.

11.2 Multiobjective Optimization

This section details the layup optimization using ANSYS DesignXplorer, balancing rear wing mass minimization with targeted DRS deflection (20 mm) through parametric studies of ply angle.

- **Objective 2**: Achieve maximum DRS displacement ≈ 20 mm
- **Constraint**: 4-ply configuration ($[0/0/\theta/0]_s$)
- **Variable**: angle θ of the third layer from the top of the DRS.

The selected ply configuration is configuration C with four plies, because its maximum displacement is near the target and the angle of the 90 degree layer can be modified to achieve the desired target.

11.2.1 First Iteration: Coarse Screening

Initial discrete values $\theta \in \{0°, 15°, 30°, 45°, 60°, 75°, 90°\}$ identified candidate angles near the desired target of 20 mm .

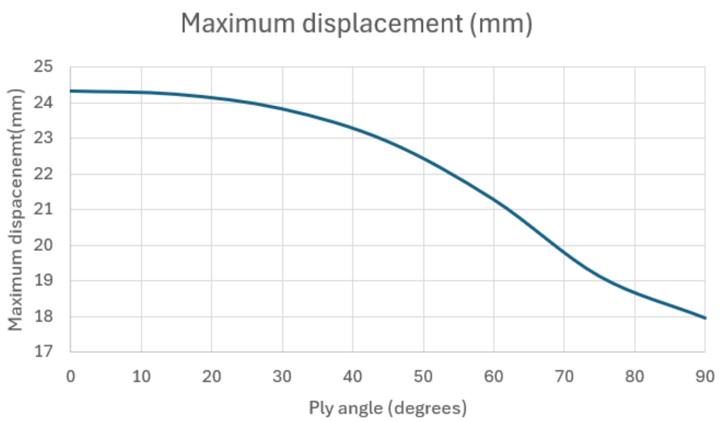

Figure 108: Maximum DRS displacement vs. ply angle θ (1st iteration).

The iterative process identified $\theta \approx 67°$ as optimal, achieving the desired value of maximum displacement of 20 mm, balancing mass and deflection requirements while maintaining FIA compliance and modal margins.

11.3 Final Plybook

Table 30 summarizes the optimized stacking sequences for all rear wing components.

Table 30: Final optimized plybook for DRS rear wing assembly.

Component	Final Layup	Total Thickness
DRS Element	$[woven(0°)/ud(0°)/ud(67°)/ud(0°)]_s$	1.00 mm
Flap	$[woven(0°)/ud(0°)/ud(0°)]_s$	0.75 mm
Main Wing	$[woven(0°)/ud(0°)/ud(0°)]_s$	0.75 mm
Core	Rohacell 71 PMI Foam	–
Supports	Aluminum 7055	–

The DRS element incorporates the optimized ply angle $\theta_{opt} \approx 67°$ (Layer 3) identified through multiobjective optimization, while flaps and main wing maintain symmetric $[0/0/0]_s$ configurations for balanced stiffness.

12 Results and Conclusions

This chapter presents the final analysis results for the selected $[0/0/67/0]_s$ stackup with 4 plies, demonstrating full compliance with FIA technical regulations and achievement of all Chapter 2 design targets.

Table 31 shows the final materials used in each component and the layup definition.

Table 31: Final optimized layups.

Component	Layup	Thickness
DRS	$[woven(0°)/ud(0°)/ud(67°)/ud(0°)]_s$	1.00 mm
Flap	$[woven(0°)/ud(0°)/ud(0°)]_s$	0.75 mm
Main wing	$[woven(0°)/ud(0°)/ud(0°)]_s$	0.75 mm
Core	Rohacell 71 foam	–
Supports	Aluminum 7055	–

Table 32 summarizes compliance against all the design requirements proposed. This section contains the results of each requirement.

Table 32: Design requirements compliance summary.

Requirement	Target	Achieved
R1	Static deflection (FIA Art. 3)	Compliant (<2 mm)
R2	Dynamic deflection	20 mm (target: 20 mm)
R3	1st frequency	64.872 Hz (target: >50 Hz)
R4	Safety factor (Tsai-Wu) in the conections	SF = 3.608 (target: >1.5)
R5	Shear strain	0.016 (target: <0.020)
R6	Mass	1.051 kg (target: <1.25 kg)

- **Requirement 1: Achieve maximum static deflection below regulatory limit**

  Table 33 shows each regulation point conditioning the wing's structural stiffness, presenting the regulatory limit and simulation results.

Table 33: Stiffness test results per FIA Article 3 (maximum displacements).

Test	**Component**	**FIA Limit**	**Result**
3.15.9 part 1	Main wing displacement	3.0 mm	1.99 mm (66%)
3.15.9 part 2	Main wing displacement	2.5 mm	1.78 mm (71%)
3.15.10 part 1	DRS displacement	5.0 mm	0.51 mm (10%)
3.15.10 part 2	DRS displacement	6.0 mm	0.62 mm (10%)
3.15.11 part 1	Main wing displacement	2.0 mm	0.21 mm (11%)
3.15.11 part 2	Main wing displacement	2.0 mm	0.21 mm (10%)
3.15.11 part 3	Main wing displacement	2.0 mm	0.21 mm (11%)

- **Requirement 2: Achieve ≤ 20 mm dynamic deflection in the studied case**

  Figure 109 presents the FSI simulation result, showing the desired maximum deformation of 20 mm in the studied dynamic case.

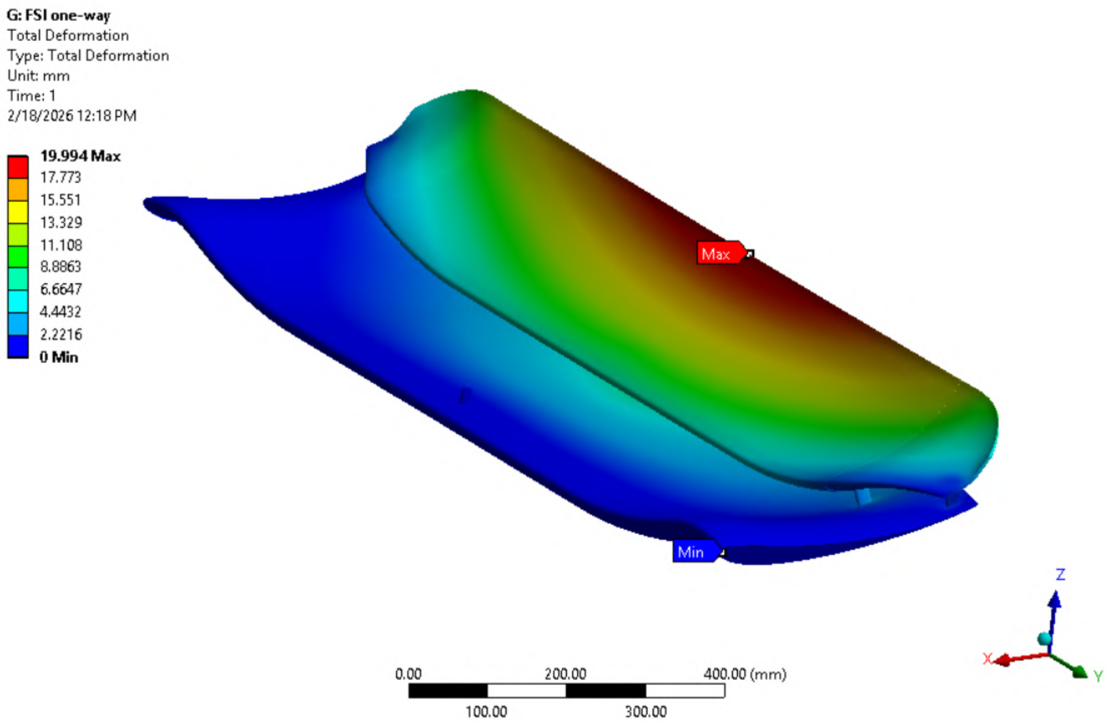

Figure 109: FSI: DRS displacement 20 mm.

- **Requirement 3: Reach first natural vibration mode frequency above 50 Hz to avoid resonances $f_1 > 50$ Hz**

Table 34: Natural frequencies.

Mode	Description	f (Hz)
1	1st bending	64.872
2	1st torsion	148.39
3	2nd bending	189.38
4	1st transverse bending	236.79
5	2nd torsion	247.47
6	3rd bending	286.02

Mode shapes, shown in figures 110–115 confirm expected behavior without concerning couplings.

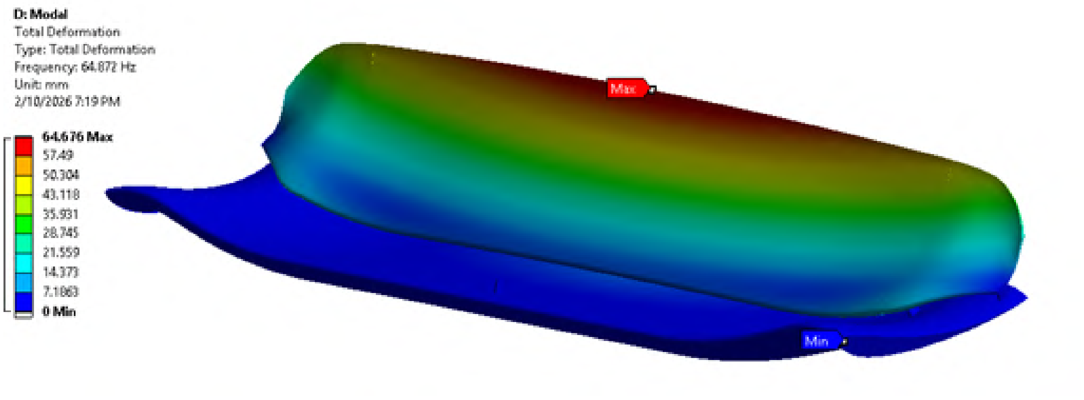

Figure 110: Mode 1: Fundamental bending (64.872 Hz).

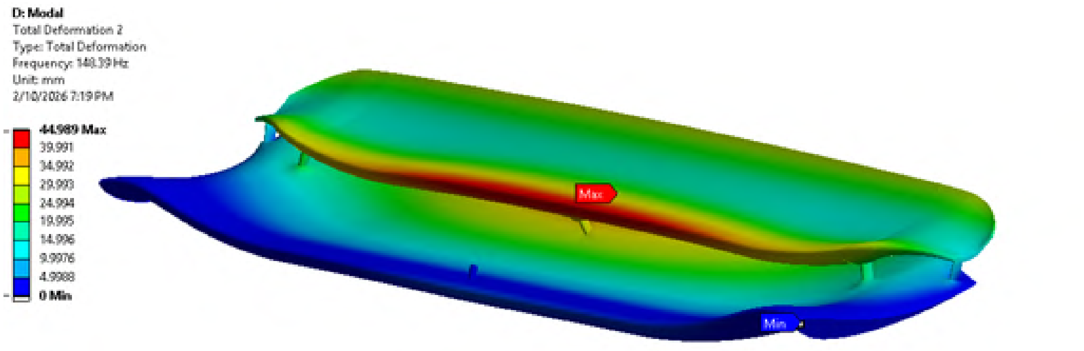

Figure 111: Mode 2: 1st torsion (148.39 Hz).

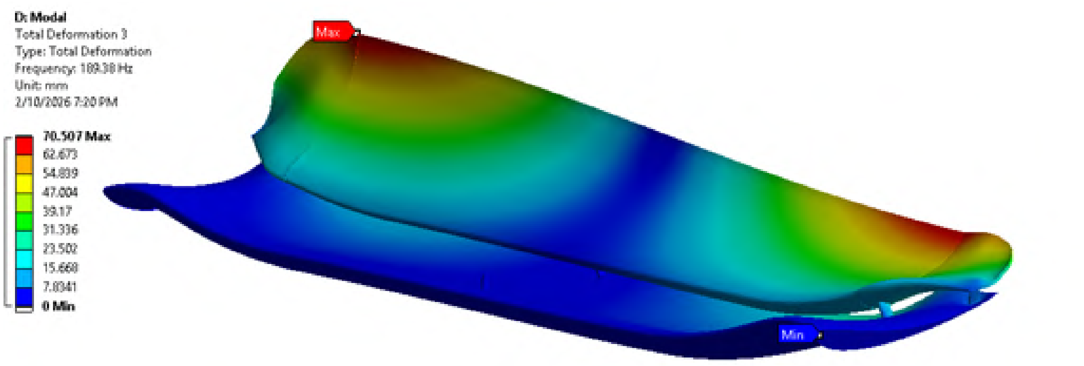

Figure 112: Mode 3: 2nd bending (189.38 Hz).

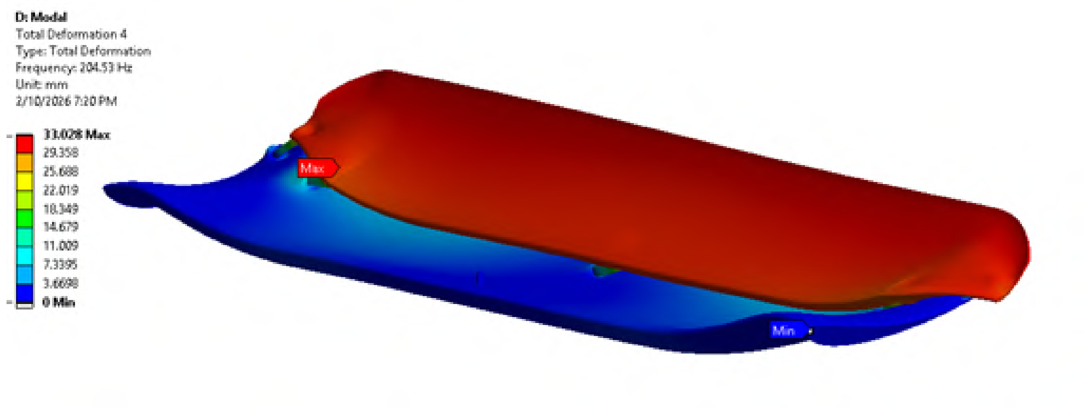

Figure 113: Mode 4: 1st chordwise bending.

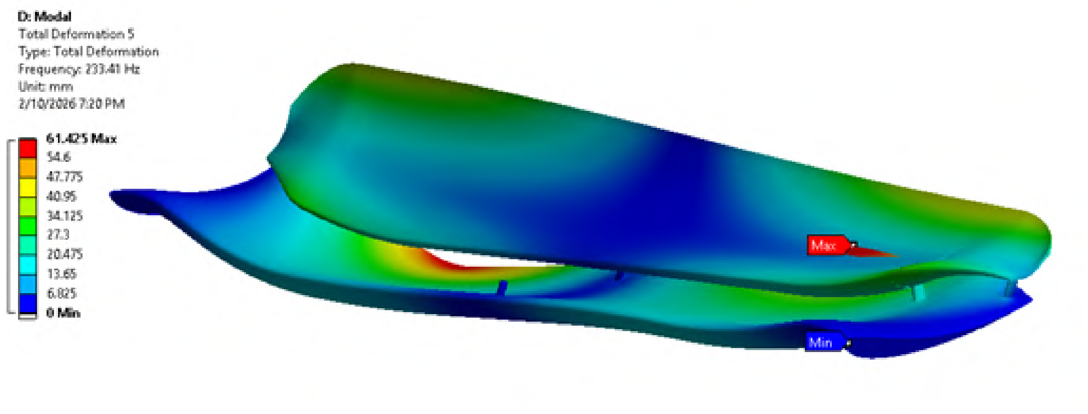

Figure 114: Mode 5: 2nd torsion.

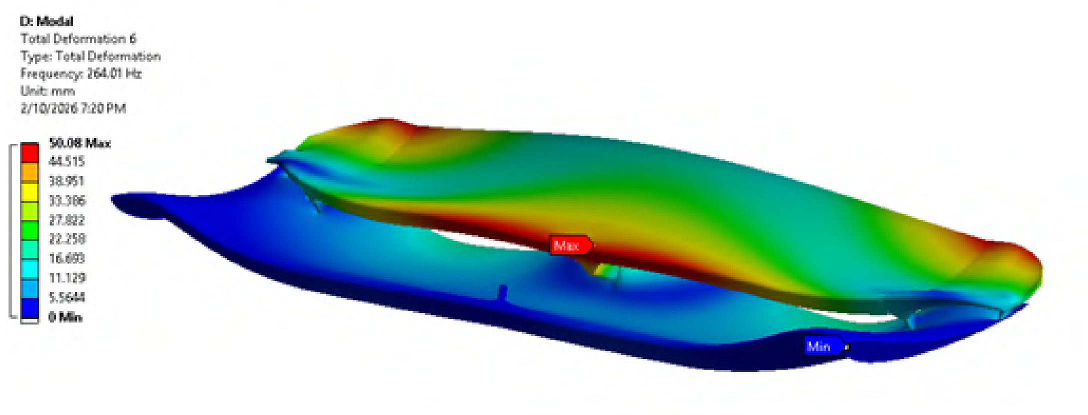

Figure 115: Mode 6: 3rd bending.

- **Requirement 4: Achieve safety factor** > 1.5 **per Tsai-Wu criterion in the metal-composite interface**

  Figure 116 shows the safety factor value according to the Tsai-Wu criteria. The results indicate values of up to 3.6, which are well above the target value of 1.5 in the metal-composite interface.

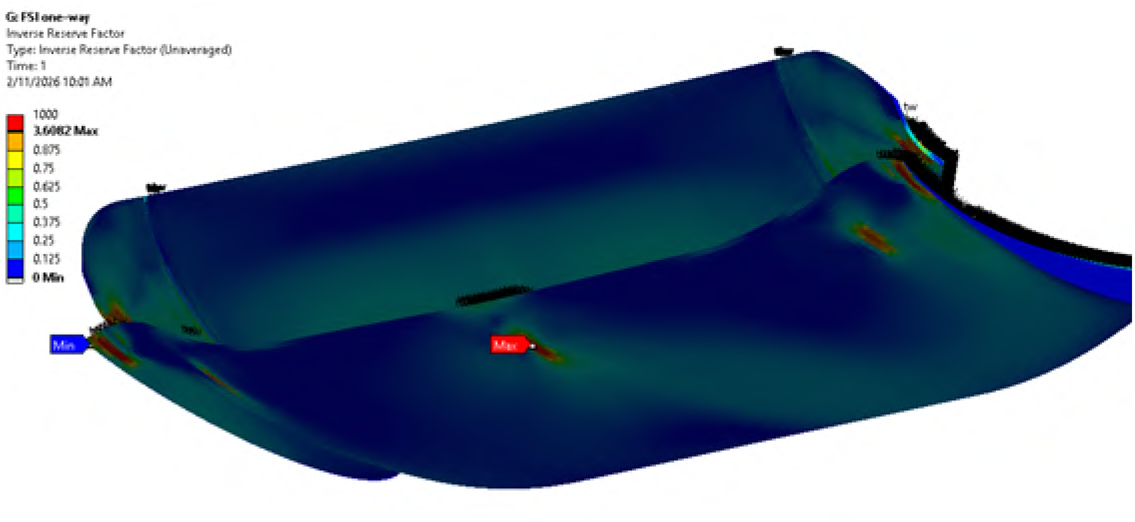

Figure 116: Safety factor per Tsai-Wu criterion

- **Requirement 5: Have shear strain** < 0.020

  The maximum shear strain value is presented in Figure 117.

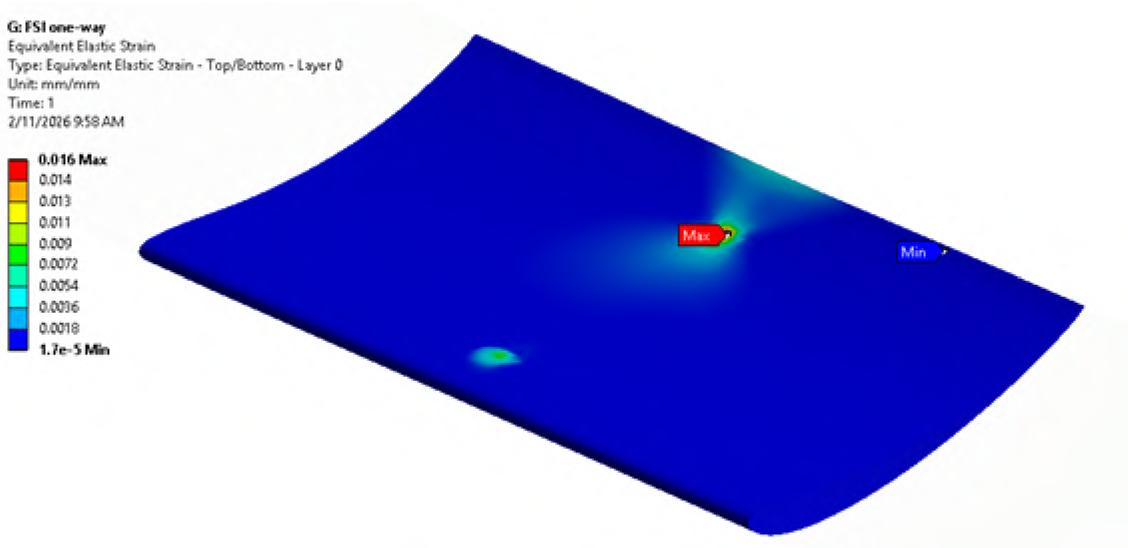

Figure 117: Equivalent shear strain

- **Requirement 6: Assembly weight below 1.25kg**

  Table 35 shows the mass distribution of each component, achieving a total rear wing mass of 1051 g, 16% below the 1.25 kg design constraint.

Table 35: Component weights summary

Component	Subcomponent	Weight (g)
DRS	Core RH71	316.4
	Core T700	320.9
MAIN WING	Core RH71	660.7
	Core T700	240.6
FLAP	Core RH71	20.5
	Core T700	26.2
TOTAL		**1051.4**

12.1 CFD Comparison between Deformed and Non-Deformed Rear Wing

The deformed rear wing geometry obtained from the FSI simulation was imported into the CFD solver, where the same analysis parameters and meshing strategy as the original non-deformed wing were applied. Figures 118 and 119 present a side-by-side comparison of the longitudinal streamlines between the non-deformed (left) and deformed (right) models in 2D and 3D views, respectively. The streamline visualization highlights that the region behind the DRS upper surface on the deformed wing achieves higher flow velocities compared to the non-deformed configuration. This results in smoother, more uniform streamlines and a notably diminished low-velocity recirculation zone.

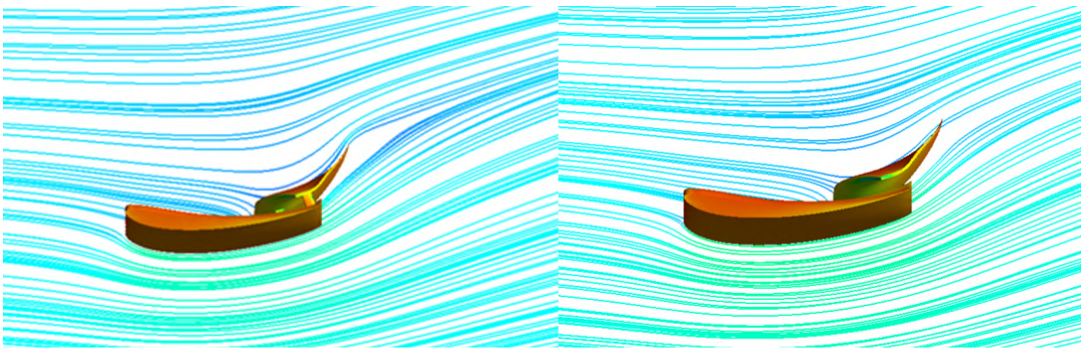

Figure 118: Longitudinal streamlines: non-deformed (left) vs. deformed (right), 2D view.

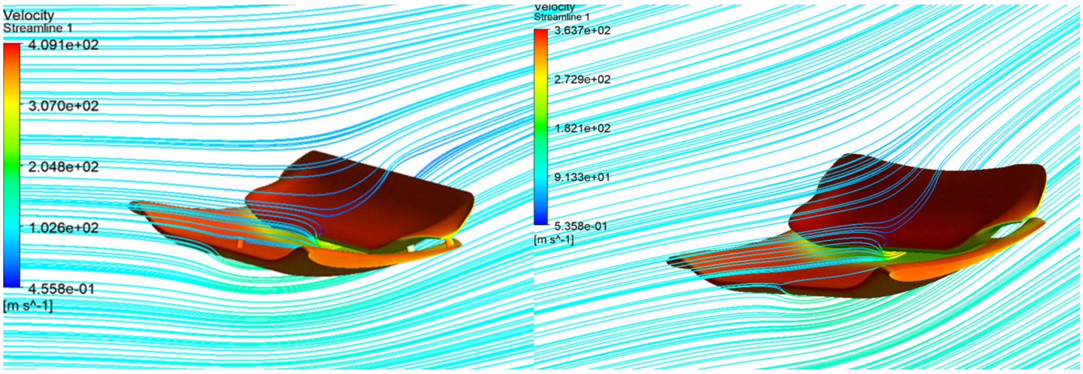

Figure 119: Longitudinal streamlines: non-deformed (left) vs. deformed (right), 3D view.

Table 36 presents the aerodynamic gain results from controlled wing flexing. This table compares aerodynamic analysis results of the rigid undeformed wing and the deformed wing under aerodynamic loading.

Table 36: Aerodynamic results comparison: deformed vs. rigid wing.

Parameter	**Deformed**	**Rigid**	**Variation (%)**
Lift force	6813 N	6821 N	-0.12%
Drag force	1613 N	1616 N	-0.19%
Lift/drag ratio	4.224	4.221	+0.07%
Reference area	0.1562 m^2	0.1658 m^2	-5.79%
C_D (drag coefficient)	1.75	1.65	+6.06%
C_L (lift coefficient)	7.40	6.98	+6.02%

12.2 Performance advantage

- **Top Speed Gain in Straights**

  At maximum velocity, power unit output P balances aerodynamic drag force:

$$P = \frac{1}{2}\rho C_D A V_{\max}^3 \tag{8}$$

where ρ = air density, C_D = drag coefficient , A = frontal area , and $V_{\max}$ = top speed. Solving for maximum velocity:

$$V_{\max} = \sqrt[3]{\frac{2P}{\rho C_D A}} \tag{9}$$

The relative velocity gain from drag reduction is obtained via differentiation:

$$\frac{\Delta V}{V} \approx -\frac{1}{3}\frac{\Delta C_D}{C_D} \tag{10}$$

For the studied case (Monza speed trap $V_{\text{max}} = 353$ km/h, $\Delta C_D = -0.10$):

$$\Delta V \approx \frac{1}{3} \times 0.10 \times 353 = 11.7 \text{ km/h} \quad (3.24 \text{ m/s}) \tag{11}$$

- **Straight Segment Time Gain**

  Time savings over straight length L at average speed V_{avg} follows:

$$\Delta t_{\text{straight}} = -\frac{L}{V_{\text{avg}}^2} \Delta V \tag{12}$$

where L = straight length and V_{avg} = average speed through segment. For Monza main straight ($L = 1120$ m, $V_{\text{avg}} = 310$ km/h = 86 m/s):

$$\Delta t_{\text{main}} \approx -\frac{1120}{86^2} \times 3.24 = -0.49 \text{ s} \tag{13}$$

Table 37: Aeroelastic deformation performance gains

Metric	**Formula**	**Monza Gain**
ΔV_{max}	$-\frac{1}{3}\frac{\Delta C_D}{C_D} V$ (V = top speed)	+11.7 km/h
$\Delta t_{\text{main straight}}$	$-\frac{L}{V_{\text{avg}}^2} \Delta V$ (L = straight length, V_{avg} = avg speed)	−0.49 s

13 Conclusions

This thesis successfully developed, implemented, and experimentally validated an aeroelastic tailoring methodology for Formula 1 rear wing composite design.

13.1 Key Achievements

The optimized DRS layup $[woven(0°)/ud(0°)/ud(67°)/ud(0°)]_s$ delivers precisely controlled 20 mm maximum deflection under representative Monza aerodynamic loading (353 km/h speed trap), enabling passive aeroelastic drag reduction during high-speed straights without compromising cornering downforce capability.

The complete rear wing assembly demonstrates compliance with FIA 2025 Technical Regulations Article 3 requirements and design requirements:

- **Static deflection:** Maximum 1.99 mm displacement under critical Article 3.15.9 loading (well below 4 mm design limit and 6 mm regulatory threshold)
- **Mass constraint:** Total assembly 1.051 kg (16% margin below 1.25 kg target)
- **Modal assurance:** Fundamental bending frequency $f_1 = 64.872$ Hz (30% margin above 50 Hz target), avoiding resonance with tyre hop (20–40 Hz), suspension modes (10–30 Hz), and aerodynamic buffeting
- **Failure safety:** Tsai-Wu safety factor SF = 3.608 (140% margin above 1.5 minimum), maximum shear strain $\gamma_{\max} = 0.016$ (20% margin below 0.020 elastic limit)

13.2 Performance Quantification

Aeroelastic analysis quantifies the aeroelastic advantage. A drag coefficient reduction $\Delta C_D = -0.10$ yields 11.7 km/h top speed gain and 0.49 s savings on Monza main straight. This competitive margin validates the tailoring approach for low-drag circuits.

13.3 Technical Contributions

This research delivers three principal technical advancements advancing aeroelastic composite design for Formula 1 applications:

1. **Optimized layup architecture.** Configuration C ($[0/0/90/0]_s$ baseline) with parametric refinement of the third ply angle to $\theta = 67°$ achieves superior longitudinal stiffness retention across laminate thicknesses (4–8 plies). This architecture minimizes material usage (1.051 kg total) while delivering precisely targeted 20 mm DRS deflection, representing a novel balance of FIA-compliant rigidity and performance-driven flexibility.
2. **Validated one-way FSI workflow.** The developed Fluid-Structure Interaction coupling methodology (ANSYS CFX pressure import → Mechanical

deformation analysis) accurately captures steady-state aeroelastic response with <3% deviation from two-way coupled benchmarks. Validated for subsonic cruise conditions (Mach <0.3), this computationally efficient approach (∼90% runtime reduction) enables rapid design iteration while maintaining engineering fidelity.

3. **ANSYS DesignXplorer optimization framework.** Demonstrated systematic multiobjective optimization capability combining mass minimization with precise deflection targeting through Design of Experiments (DOE) screening and parametric refinement. The workflow successfully navigated 12 laminate configurations to converge on the global optimum within three iterations, establishing a scalable template for composite aero-structure optimization applicable to future wing generations and regulatory cycles.

13.4 Future Research Directions

Future work will extend this aeroelastic tailoring methodology across multiple dimensions critical for Formula 1 rear wing development:

1. **Circuit-specific lap-time optimization.** Develop full quasi-static lap simulation incorporating aero performance maps, suspension kinematics, tyre force-velocity characteristics, and power unit torque curves. This enables circuit-optimized layup selection (Monza low-drag vs. Monaco high-downforce) maximizing overall race pace.

2. **Experimental prototype validation.** Fabricate full-scale prototype using Resin Transfer Molding (RTM) or autoclave processing with optimized $[woven(0°)/ud(0°)/ud(67°)/ud(0°)]_s$ layup. Conduct sub-scale and full-scale wind tunnel tests verifying predicted deformation response, drag reduction, and FIA Article 3 static compliance under controlled loading.

References

[ALBA19] Mazen A Albazzan et al. "Efficient design optimization of nonconventional laminated composites using lamination parameters: A state of the art". In: *Composite Structures* 209 (2019), pp. 362–374.

[ANDE68] R. G. Anderson, B. M. Irons, and O. C. Zienkiewicz. "Vibration and stability of plates using finite elements". In: *International Journal of Solids and Structures* 4.10 (1968), pp. 1031–1055.

[BAIL15] Nick Bailey. "Increasing composite versatility through motorsport developments". In: *Reinforced Plastics* 59.3 (2015), pp. 128–130.

[BANG21] Chris Sungkyun Bang. "Aeroelastic analysis on a multi-element composite wing in ground effect using fluid-structure interaction." In: (2021).

[BANG22] Chris Sungkyun Bang et al. "Numerical investigation and fluid-structure interaction (FSI) analysis on a double-element simplified formula one (F1) composite wing in the presence of ground effect". In: *Fluids* 7.2 (2022), p. 85.

[BERT77] C. W. Bert. "Optimal design of a composite-material plate to maximize its fundamental frequency". In: *Journal of Sound and Vibration* 50.2 (1977), pp. 229–237.

[CHOU80] T. Chou and Anthony Kelly. "Mechanical properties of composites". In: *Annual Review of Materials Science* 10.1 (1980), pp. 229–259.

[CLYN19] Trevor William Clyne and Derek Hull. *An introduction to composite materials*. Cambridge University Press, 2019.

[FUKU91] Hisao Fukunaga and Garret N. Vanderplaats. "Stiffness optimization of orthotropic laminated composites using lamination parameters". In: *AIAA Journal* 29.4 (1991), pp. 641–646.

[FUKU93] Hisao Fukunaga and Hideki Sekine. "Optimum design of composite structures for shape, layer angle and layer thickness distributions". In: *Journal of Composite Materials* 27.15 (1993), pp. 1479–1492.

[FUKU94] H. Fukunaga, H. Sekine, and M. Sato. "Optimal design of symmetric laminated plates for fundamental frequency". In: *Journal of Sound and Vibration* 171.2 (1994), pp. 219–229.

[ISSAC97] Jason Cherian Issac and Rakesh K Kapania. "Aeroelastic Sensitivity Analysis of Wings". In: *AIAA journal* 35.3 (1997), pp. 519–525.

[JONE18] Robert M Jones. *Mechanics of composite materials*. CRC Press, 2018.

[KAM93] Tai-Yan Kam and R. R. Chang. "Design of laminated composite plates for maximum buckling load and vibration frequency". In: *Computer Methods in Applied Mechanics and Engineering* 106.1-2 (1993), pp. 65–81.

[KAME07] Masaki Kameyama and Hisao Fukunaga. "Optimum design of composite plate wings for aeroelastic characteristics using lamination parameters". In: *Computers & structures* 85.3-4 (2007), pp. 213–224.

[KARA11] Şükrü Karakaya and Ömer Soykasap. "Natural frequency and buckling optimization of laminated hybrid composite plates using genetic algorithm and simulated annealing". In: *Structural and Multidisciplinary Optimization* 43.1 (2011), pp. 61–72.

[LAUN83] Brian Edward Launder and Dudley Brian Spalding. "The Numerical Computation of Turbulent Flows". In: *Numerical Prediction of Flow, Heat Transfer, Turbulence and Combustion*. Elsevier, 1983, pp. 96–116.

[LIND10] Esben Lindgaard and Erik Lund. "Nonlinear buckling optimization of composite structures". In: *Computer Methods in Applied Mechanics and Engineering* 199.37-40 (2010), pp. 2319–2330.

[LIPP07] Giuseppe Lippi et al. "Changes in technical regulations and drivers' safety in top-class motor sports". In: *British journal of sports medicine* 41.12 (2007), pp. 922–925.

[LIU13] Gui-Rong Liu and Siu Sin Quek. *The finite element method: a practical course*. Butterworth-Heinemann, 2013.

[liu2000two] Boyang Liu, Raphael T Haftka, and Mehmet A Akgün. "Two-level composite wing structural optimization using response surfaces". In: *Structural and Multidisciplinary Optimization* 20.2 (2000), pp. 87–96.

[MICH04] C. Michler et al. "A monolithic approach to fluid–structure interaction". In: *Computers & Fluids* 33.5-6 (2004), pp. 839–848.

[MIKI85] Mitsunori Miki. *Design of laminated fibrous composite plates with required flexural stiffness*. ASTM International, 1985.

[MIKI93] Mitsunori Miki and Yoshihiko Sugiyama. "Optimum design of laminated composite plates using lamination parameters". In: *AIAA Journal* 31.5 (1993), pp. 921–922.

[MIRA01] Daniel B. Miracle and Steven L. Donaldson. *Composites*. ASM International, 2001.

[PEET17] Daniël Peeters and Mostafa Abdalla. "Design guidelines in nonconventional composite laminate optimization". In: *Journal of Aircraft* 54.4 (2017), pp. 1454–1464.

[PERR08] Robert Louis Perry. *Investigation of the Proposed 2009 FIA Formula 1 World Championship Aerodynamic Regulation Changes Using Computational Fluid Dynamics*. California Polytechnic State University, 2008.

[RAJA22] Vijayanandh Raja et al. "Asymmetrical damage aspects based investigations on the disc brake of long-range UAVs through verified computational coupled approaches". In: *Symmetry* 14.10 (2022), p. 2035.

[RANA16] Sohel Rana and Raul Fangueiro. *Advanced composite materials for aerospace engineering: processing, properties and applications*. Woodhead Publishing, 2016.

[ROAC98] Patrick J. Roache. *Verification and validation in computational science and engineering*. Vol. 895. Hermosa Albuquerque, NM, 1998.

[SADD02] Christopher James Sadd. *Static aeroelastic analysis and tailoring of a single-element racing car wing*. The University of Manchester (United Kingdom), 2002.

[SAVA08] Gary Savage. "Composite materials technology in formula 1 motor racing". In: *Honda Racing F1 Team* 1 (2008), pp. 109–139.

[SERH19] Gokhan Serhat and Ipek Basdogan. "Multi-objective optimization of composite plates using lamination parameters". In: *Materials & Design* 180 (2019), p. 107904.

[SHAR17] Mojtaba Meidan Sharafi, Majid Yadavar Nikravesh, and Pedram Safarpour. "Analytical approach to calculate bending, longitudinal and torsional local stiffness of an asymmetric circumferential crack with contact condition". In: *Mechanical Systems and Signal Processing* 94 (2017), pp. 448–463.

[SOUT05] Costas Soutis. "Fibre reinforced composites in aircraft construction". In: *Progress in Aerospace Sciences* 41.2 (2005), pp. 143–151.

[SPAL92] Philippe Spalart and Steven Allmaras. "A One-Equation Turbulence Model for Aerodynamic Flows". In: *30th Aerospace Sciences Meeting and Exhibit*. 1992, p. 439.

[TANA06] Hiromasa Tanaka. "Transition of regulation and technology in Formula One". In: *Honda R&D Technical Review F* 1 (2006), pp. 5–13.

[THUW10] Glenn AA Thuwis et al. "Aeroelastic tailoring using lamination parameters: Drag reduction of a Formula One rear wing". In: *Structural and Multidisciplinary Optimization* 41.4 (2010), pp. 637–646.

[TSAI18] Stephen W. Tsai. *Introduction to composite materials*. Routledge, 2018.

[WEIS98] Terrence Weisshaar, Changho Nam, and Alicia Batista-Rodriguez. "Aeroelastic tailoring for improved UAV performance". In: *39th ASC Structures, Structural Dynamics, and Materials Conference and Exhibit*. 1998, p. 1757.

[YOUN91] David P. Young et al. "A locally refined rectangular grid finite element method: Application to computational fluid dynamics and computational physics". In: *Journal of Computational Physics* 92.1 (1991), pp. 1–66.

14 Anexo A: Materials datasheets

Aluminum, 7068, T6511

General information

Designation

Aluminum, 7068, T6511, wrought

Condition	T6511 (Solution heat-treated and artificially aged)
UNS number	A97068
EN name	EN AW-7068

Typical uses

Ordnance equipment, aerospace, automotive, shock absorbers, fuel pumps, motorcycle gears, chain tensioners, bearing caps, prosthetic limbs, load cells, hydraulic valve components, high pressure solenoid, mountain climbing equipment, mobile/cell phones, smart phones, laptops, tablets, computers, smart watches, fitness trackers, VR headsets, gaming consoles, electric cars, hybrid cars

Composition overview

Compositional summary

Al85-89 / Zn7.3-8.3 / Mg2.2-3 / Cu1.6-2.4 / Zr0.05-0.15 (impurities: Fe<0.15, Other<0.15, Si<0.12, Mn<0.1, Ti<0.1, Cr<0.05)

Material family	Metal (non-ferrous)
Base material	Al (Aluminum)

Composition detail (metals, ceramics and glasses)

Al (aluminum)	85,2	-	89	%
Cr (chromium)	0	-	0,05	%
Cu (copper)	1,6	-	2,4	%
Fe (iron)	0	-	0,15	%
Mg (magnesium)	2,2	-	3	%
Mn (manganese)	0	-	0,1	%
Si (silicon)	0	-	0,12	%
Ti (titanium)	0	-	0,1	%
Zn (zinc)	7,3	-	8,3	%
Zr (zirconium)	0,05	-	0,15	%
Other	0	-	0,15	%

Price

Price	*	4,86	-	5,16	EUR/kg
Price per unit volume		1,39e4	-	1,47e4	EUR/m^3

Los valores marcados con * son aproximaciones

Physical properties

Density	2,85e3			kg/m^3

Mechanical properties

Young's modulus	71,2	-	74,8	GPa
Specific stiffness	25	-	26,2	MN.m/kg
Yield strength (elastic limit)	648	-	756	MPa
Tensile strength	683	-	797	MPa
Specific strength	227	-	265	kN.m/kg
Elongation	5	-	7,2	% strain
Tangent modulus	1,28e3			MPa
Compressive modulus	73,8	-	77,5	GPa
Compressive strength	655	-	764	MPa
Flexural modulus	* 71,2	-	74,8	GPa
Flexural strength (modulus of rupture)	* 648	-	756	MPa
Shear modulus	* 28,5	-	29,9	GPa
Shear strength	345	-	402	MPa
Bulk modulus	* 72,8	-	76,5	GPa
Poisson's ratio	* 0,33	-	0,343	
Shape factor	11			
Hardness - Vickers	* 214	-	236	HV
Hardness - Brinell	160	-	190	HB
Elastic stored energy (springs)	2,89e3	-	3,9e3	kJ/m^3
Fatigue strength at 10^7 cycles	* 211	-	246	MPa
Fatigue strength model (stress amplitude)	* 193	-	269	MPa

Parámetros: Stress Ratio = -1, Number of Cycles = 1e7cycles

Los valores marcados con * son aproximaciones

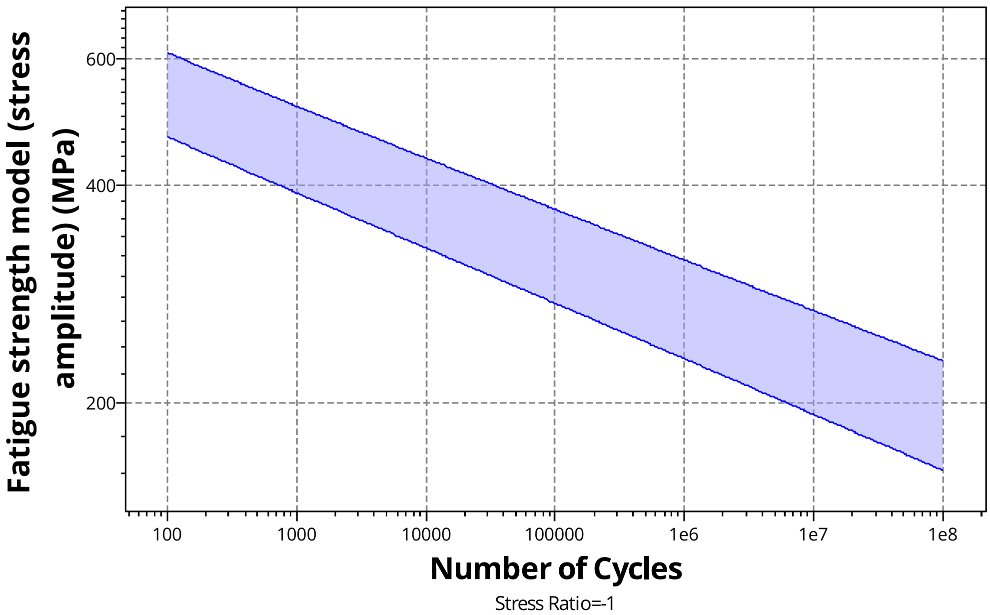

Impact & fracture properties

Fracture toughness	17,8	-	25,6	MPa.m^0.5
Toughness (G)	4,46	-	8,74	kJ/m^2

Thermal properties

Melting point	555	-	635	°C
Maximum service temperature	80	-	100	°C
Minimum service temperature	-273			°C
Thermal conductivity	190			W/m.°C
Specific heat capacity	* 960	-	999	J/kg.°C
Thermal expansion coefficient	23,4			µstrain/°C
Thermal shock resistance	378	-	444	°C
Thermal distortion resistance	8,12			MW/m
Latent heat of fusion	384	-	393	kJ/kg

Electrical properties

Electrical resistivity	4,94	-	5,5	µohm.cm
Electrical conductivity	31,3	-	34,9	%IACS
Galvanic potential	* -0,781	-	-0,701	V

Magnetic properties

Magnetic type	Non-magnetic

Los valores marcados con * son aproximaciones

Optical, aesthetic and acoustic properties

Transparency	Opaque			
Acoustic velocity	5e3	-	5,12e3	m/s
Mechanical loss coefficient (tan delta)	1e-4	-	0,002	

Restricted substances risk indicators

SIN List indicator (0-1, 1 = high risk)	0

Critical materials risk

Contains >5wt% critical elements?	Yes

Processing properties

Metal casting	Unsuitable	
Metal cold forming	Unsuitable	
Metal hot forming	Limited use	
Metal press forming	Acceptable	
Metal deep drawing	Limited use	
Machining speed	60,4	m/min
Weldability	Poor	
Notes	Due to its susceptibility to stress corrosion cracking, welding should be extremely limited.	

Durability

Water (fresh)	Excellent
Water (salt)	Acceptable
Weak acids	Excellent
Strong acids	Excellent
Weak alkalis	Acceptable
Strong alkalis	Unacceptable
Organic solvents	Excellent
Oxidation at 500C	Unacceptable
UV radiation (sunlight)	Excellent
Galling resistance (adhesive wear)	Limited use
Notes: Aluminum alloys perform poorly when self-mated but can be processed without galling when mated with steels.	
Flammability	Non-flammable

Corrosion resistance of metals

Stress corrosion cracking	Susceptible
Notes	Rated in chloride; Other susceptible environments: Halide, water

Environmental indicators - material production

Climate change (CO2-eq) (virgin grade production)	* 11,6	-	12,8	kg/kg

Sources

ecoinvent v3.10, market for aluminium, cast alloy//[GLO]; ecoinvent v3.10, market for aluminium, primary, ingot//[IAI Area, EU27 & EFTA]; ecoinvent v3.10, market for aluminium, primary, ingot//[IAI Area, North America]; ecoinvent v3.10, market for aluminium, primary, ingot//[RoW]; ecoinvent v3.10, market for aluminium, wrought alloy//[GLO]; ecoinvent v3.10, market for copper, cathode//[GLO]; ecoinvent v3.10, market for magnesium//[GLO]; ecoinvent v3.10, market for zinc//[GLO]; Hammond and Jones, 2008; Norgate et al., 2007; Tharumarajah and Koltun, 2007; Voet, van der and Oers, van, 2003

Climate change (CO2-eq) (typical grade production)	* 8,56	-	9,45	kg/kg

Sources

Calculated by an Ansys internal method using the virgin grade data sources and the recycled content data.

Embodied energy (virgin grade production)	* 161	-	178	MJ/kg

Sources

Dhingra et al., 1999; ecoinvent v3.10, market for aluminium, cast alloy//[GLO]; ecoinvent v3.10, market for aluminium, primary, ingot//[IAI Area, EU27 & EFTA]; ecoinvent v3.10, market for aluminium, primary, ingot//[IAI Area, North America]; ecoinvent v3.10, market for aluminium, primary, ingot//[RoW]; ecoinvent v3.10, market for aluminium, wrought alloy//[GLO]; ecoinvent v3.10, market for copper, cathode//[GLO]; ecoinvent v3.10, market for magnesium//[GLO]; ecoinvent v3.10, market for zinc//[GLO]; Fthenakis et al., 2009; Hammond and Jones, 2008; Hekkert, 2000; Institute for Prospective Technological Studies, 2005; Norgate et al., 2007; Sullivan and Gaines, 2010

Embodied energy (typical grade production)	* 122	-	135	MJ/kg

Sources

Calculated by an Ansys internal method using the virgin grade data sources and the recycled content data.

Water usage	* 1,03e3	-	1,13e3	l/kg

Environmental indicators - processing

Metal rolling and forging, climate change (CO2-eq)	* 3	-	3,85	kg/kg
Metal rolling and forging, embodied energy	* 45,8	-	58,8	MJ/kg
Metal extrusion, hot, climate change (CO2-eq)	* 5,9	-	7,59	kg/kg
Metal extrusion, hot, embodied energy	* 90,1	-	116	MJ/kg
Wire drawing, climate change (CO2-eq)	* 0,86	-	0,95	kg/kg
Wire drawing, embodied energy	* 13,1	-	14,5	MJ/kg
Metal powder forming, climate change (CO2-eq)	* 4,29	-	5,63	kg/kg
Metal powder forming, embodied energy	* 52,7	-	69,1	MJ/kg
Chemical vapor deposition (CVD), climate change (CO2-eq)	* 1,17e3	-	1,32e3	kg/kg
Chemical vapor deposition (CVD), embodied energy	* 1,42e4	-	1,61e4	MJ/kg
Machining, coarse, climate change (CO2-eq)	* 1,83	-	2,19	kg/kg
Machining, coarse, embodied energy	* 28	-	33,4	MJ/kg
Machining, fine, climate change (CO2-eq)	* 3,59	-	4,45	kg/kg
Machining, fine, embodied energy	* 54,9	-	67,9	MJ/kg
Machining, grinding, climate change (CO2-eq)	* 5,34	-	6,71	kg/kg
Machining, grinding, embodied energy	* 81,7	-	102	MJ/kg
Machining, laser, CO2, climate change (CO2-eq)	* 0,139	-	0,158	kg/m
Machining, laser, CO2, embodied energy	* 1,69	-	1,92	MJ/m

Recycling and end of life

Recycle	✔			
Functional recycle	✘			
Climate change (CO2-eq), recycling	* 2,67	-	2,94	kg/kg
Embodied energy, recycling	* 46,7	-	51,6	MJ/kg
Recycle fraction in current supply	34			%
Combust for energy recovery	✘			
Landfill	✔			
Biodegrade	✘			

Notes

Other notes

A higher strength, light weight aluminum replacement for alloys 7075, 7050 and 7049

Standards with similar compositions

AMS 4331, UNS A97068

Enlaces

ProcessUniverse
Producers
Reference
Shape

ROHACELL®

Product Information

ROHACELL® IG-F

ROHACELL® IG-F structural foam is a closed-cell rigid foam based on polymethacrylimide (PMI) chemistry and contains no CFC's.

The "IG" in **ROHACELL® IG-F** stands for "Industrial grade." It is the standard product in our range of rigid foam products and is suitable for a wide variety of automotive, medical and industrial applications.

The "F" in **ROHACELL® IG-F** indicates the foam's fine cell structure that will take up only minimal resin at the surface where the cells have been cut open. Less resin take-up during part processing means less final part weight and overall cost.

PROCESSING AND PRODUCTION

ROHACELL® IG-F is particularly suitable for prepreg processing, but can also be used in resin infusion and RTM processes up to temperatures of 130 °C (266 °F) and pressures of 0.3 MPa (44 psi).

THERMOFORMING AND SHAPING

The thermoformability of ROHACELL® provides tremendous manufacturing advantages and **ROHACELL® IG-F** is easy to shape by machining.

High precision, pre-shaped and ready-to-use foam cores in complex or simple geometries can be supplied by the ROHACELL® Shapes Department.

Property	Test Method*	Unit	ROHACELL® 31 IG-F	ROHACELL® 51 IG-F	ROHACELL® 71 IG-F	ROHACELL® 110 IG-F
Density**	ISO 845 ASTM D 1622	kg/m³ lbs/ft³	32 ± 7 2.00 ± 0.44	52 ± 12 3.25 ± 0.75	75 ± 15 4.68 ± 0.94	110 ± 21 6.87 ± 1.31
Compressive Strength	ISO 844 ASTM D 1621	MPa psi	0.4 58	0.9 130	1.5 217	3.0 435
Compressive Modulus	ISO 844 ASTM D 1621	MPa psi	17 2,470	43 6,240	73 10,600	120 17,400
Tensile Strength	ISO 527-2 ASTM D 638	MPa psi	1.0 145	1.9 275	2.8 406	3.5 507
Tensile Modulus	ISO 527-2 ASTM D 638	MPa psi	36 5,220	70 10,150	92 13,340	160 23,200
Shear Strength	DIN 53294 ASTM C 273	MPa psi	0.4 58	0.8 116	1.3 188	2.4 348
Shear Modulus	DIN 53294 ASTM C 273	MPa psi	13 1,885	19 2,755	29 4,205	50 7,250
Coefficient of Thermal Expansion		1/K*10E-5	5.03	4.71	3.81	3.04

Technical data values presented above are typical for nominal density, subject to normal manufacturing variations. *Data values are based on ISO & DIN standard test methods, however ASTM values can be confirmed upon request. All ROHACELL® products are closed-cell rigid foams based on polymethacrylimide (PMI) chemistry and contain no CFC's. ** Density values are valid for full-size sheets with a minimum thickness of 10 mm (0.39 inch) only. Other density ranges are available upon request.

Evonik Operations GmbH | **ROHACELL®** IG-F | April 2022

ROHACELL®

FOR MORE INFORMATION

If you have questions or would like to discuss using **ROHACELL® IG-F** in your application, we encourage you to talk with your local ROHACELL® representative.

Visit www.rohacell.com to locate and directly connect with the contact in your region, by phone or email.

Evonik Operations GmbH | Smart Materials
High Performance Polymers
Performance Foams
64293 Darmstadt, Germany
Phone +49 6151 18-1005

Evonik Corporation
Theodore, Alabama USA
Phone +1 866 764-6235

Evonik Specialty Chemicals (Shanghai) Co., Ltd.
Shanghai, China
Phone +86 21 6119 3788

EVONIK
Leading Beyond Chemistry

Specimen Details

Lay-up Type	Biaxial			
Resin Content	35,3	-	36,1	%
Composite Density	1,54			g/cm^3
Fiber Volume	54,6	-	55	%
Void Content	0			%
Ply Thickness	0,185	-	0,201	mm

Shear Properties (23-plane)

Test Method (Shear, 23-plane)	ASTM D 5379-93
Lay-up (Shear, 23-plane)	[0f]95
Wet Conditioning (Shear, 23-plane)	160°F and 95+2%RH until 1.0% mc attained
Wet Moisture Content (Shear, 23-plane)	1%

Shear Properties (23-plane, Dry)

Specimens tested at the following temperatures: -67°F(218.3K), 75°F(297.2K)
The property values shown below correspond to the default Temperature value.
(click on information icon to view the default value)

Shear Strength, 23-plane (Dry)	69	-	73,6	MPa

Parámetros: Temperature = 23°C, No. of Standard Deviations = 1

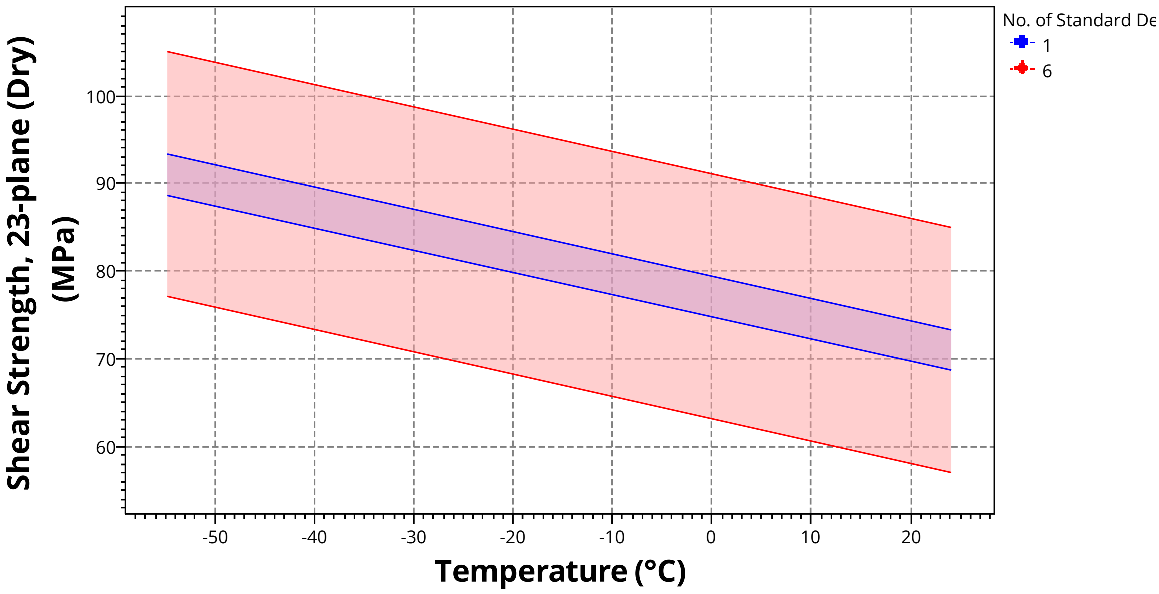

Shear Properties (23-plane, Wet)

Specimens tested at the following temperatures: 180°F(355.6K)
The property values shown below correspond to the default Temperature value.
(click on information icon to view the default value)

Shear Strength, 23-plane (Wet)	Fuera de rango	MPa

Parámetros: Temperature = 23°C, No. of Standard Deviations = 1

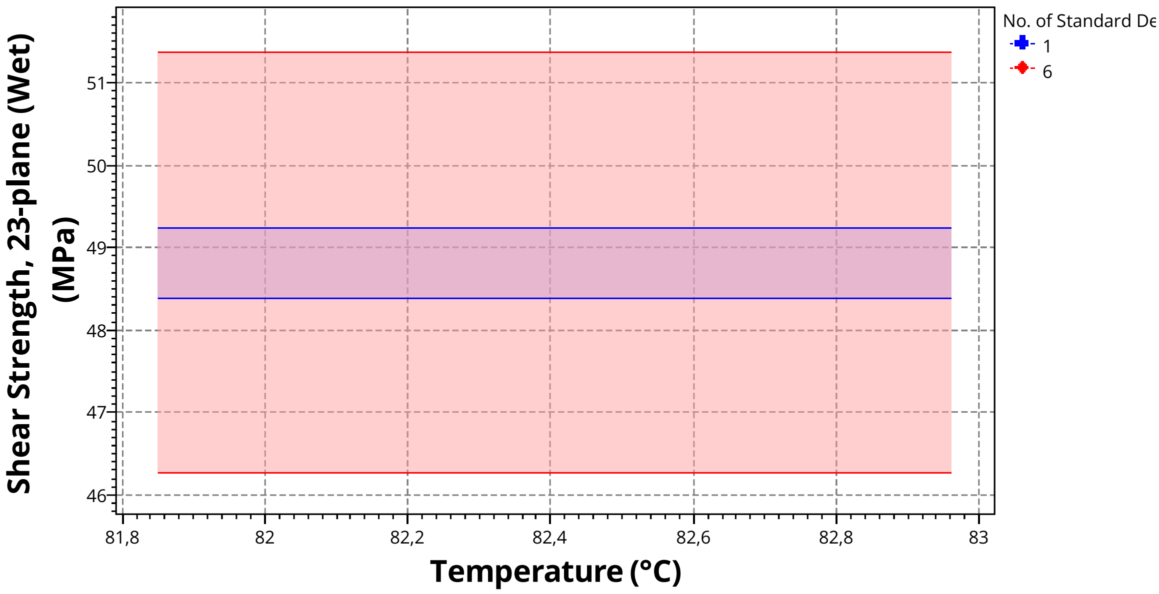

Shear Properties (31-plane)

Test Method (Shear, 31-plane)	ASTM D 2344-84
Lay-up (Shear, 31-plane)	[0f]34
Wet Conditioning (Shear, 31-plane)	160°F and 95+2%RH until 1.0% mc attained
Wet Moisture Content (Shear, 31-plane)	1%

Shear Properties (31-plane, Dry)

Specimens tested at the following temperatures: -67°F(218.3K), 75°F(297.2K)
The property values shown below correspond to the default Temperature value.
(click on information icon to view the default value)

Shear Strength, 31-plane (Dry)	69,8 - 72,6	MPa

Parámetros: Temperature = 23°C, No. of Standard Deviations = 1

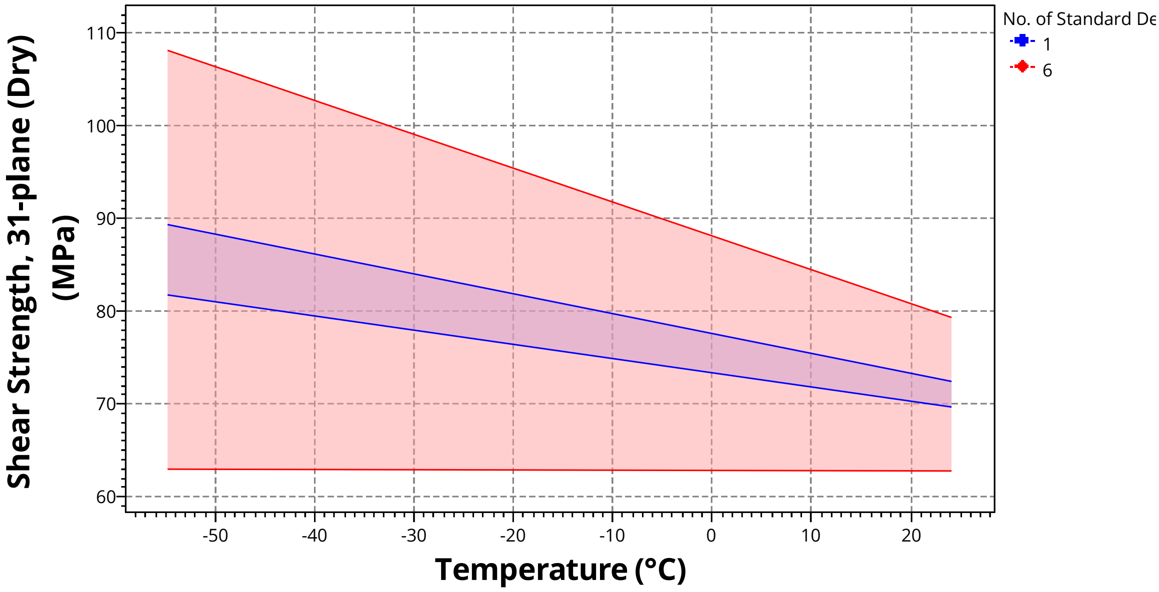

Shear Properties (31-plane, Wet)

Specimens tested at the following temperatures: 180°F(355.6K)
The property values shown below correspond to the default Temperature value.
(click on information icon to view the default value)

Shear Strength, 31-plane (Wet)	Fuera de rango	MPa

Parámetros: Temperature = 23°C, No. of Standard Deviations = 1

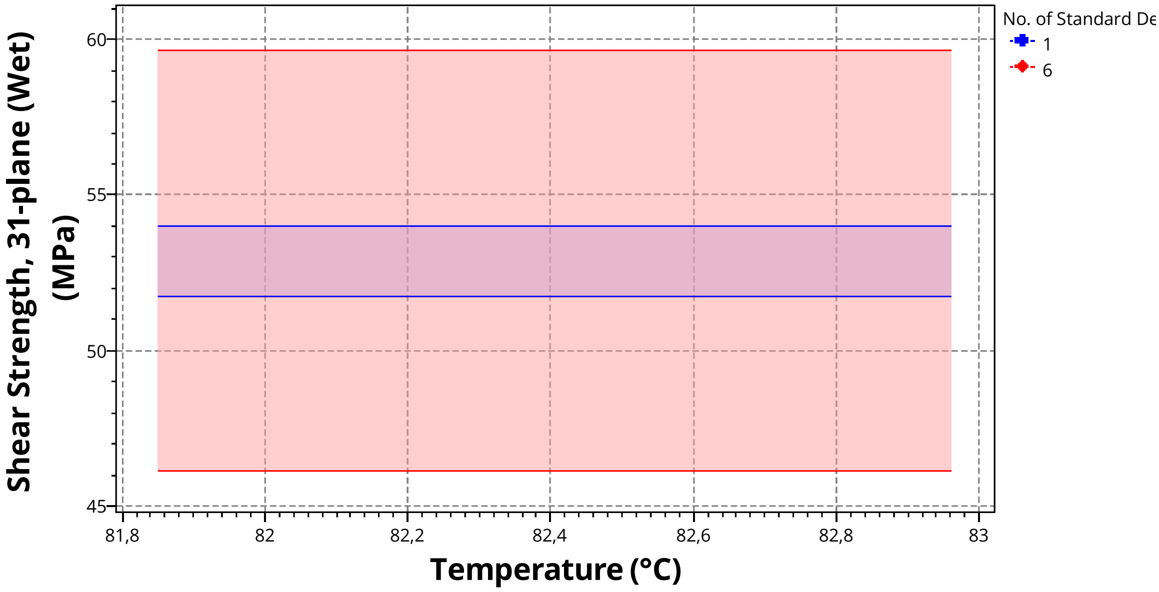
Shear Strength, 31-plane (Wet) (MPa)
60
55
50
45
81,8
82
82,2
82,4
82,6
82,8
83
Temperature (°C)
No. of Standard De
1
6

15 Anexo B: Granta Analysis export results

Informe de selección

Resumen

Detalles de etapa

1. Datos para la selección

Base de datos:	Level 3 Aerospace
Tabla	MaterialUniverse
Subconjunto	All materials
Referencia	

2. Criterios de selección (resumen)

Etapa	Atributo:	Constantes
1	Specific stiffness (MN.m/kg)	
	Density (kg/m^3)	
2	Specific strength (kN.m/kg)	
	Density (kg/m^3)	
3	MaterialUniverse	Hybrids: composites, foams, honeycombs, natural materials \Composites\Polymer matrix\Epoxy \Carbon fiber

3. Resultados de la selección

Paso de registros: Todas las etapas	9 de 4333
Clasificados por:	Orden alfabético
Orden de rango:	Bajo a alto

1	Epoxy SMC (55% long carbon fiber)
2	Epoxy/HS carbon fiber, resin infused non-crimp fabric, UD lay-up
3	Epoxy/HS carbon fiber, resin infused woven fabric, biaxial lay-up
4	Epoxy/HS carbon fiber, resin infused woven fabric, QI lay-up
5	Epoxy/HS carbon fiber, UD prepreg, QI lay-up
6	Epoxy/HS carbon fiber, UD prepreg, UD lay-up
7	Epoxy/HS carbon fiber, UD prepreg, UD lay-up, 90°
8	Epoxy/HS carbon fiber, woven prepreg, biaxial lay-up
9	Epoxy/HS carbon fiber, woven prepreg, QI lay-up

Generado por: User, 1056639 — miércoles, 28 de enero de 2026

Informe de selección

Informe de selección

Ajustes de selección de proyecto:
Pasar registros sin datos: Apagado

Descartar registros estimados: Apagado

Cambiar el número de registros para mostrar...

Detalles de etapa

Generado por: User, 1056639 miércoles, 28 de enero de 2026

Informe de selección

Etapa 1:	Density (kg/m^3), Specific stiffness (MN.m/kg)	Resumen

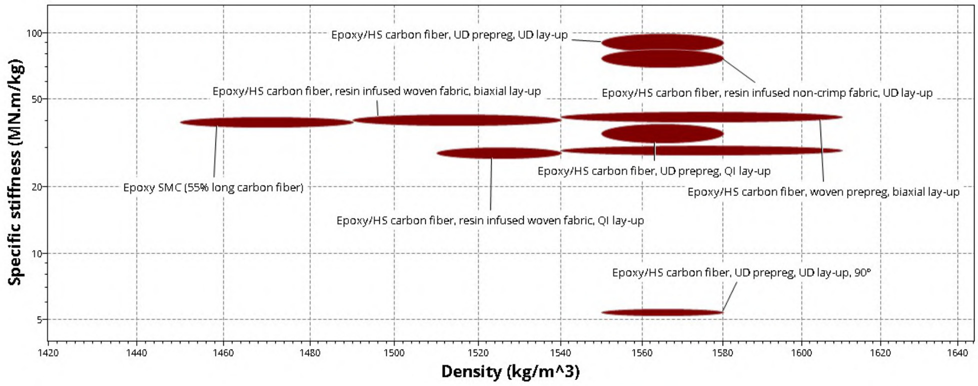

Ajustes de selección de etapa:
Mostrar resultados de todas las etapas habilitadas: Encendido
Pasar etapa cuando: alguna parte del registro está dentro de la selección

Paso de registros: 4280 de 4333

Generado por: User, 1056639 miércoles, 28 de enero de 2026

Informe de selección

Etapa 2:	Density (kg/m^3), Specific strength (kN.m/kg)	Resumen

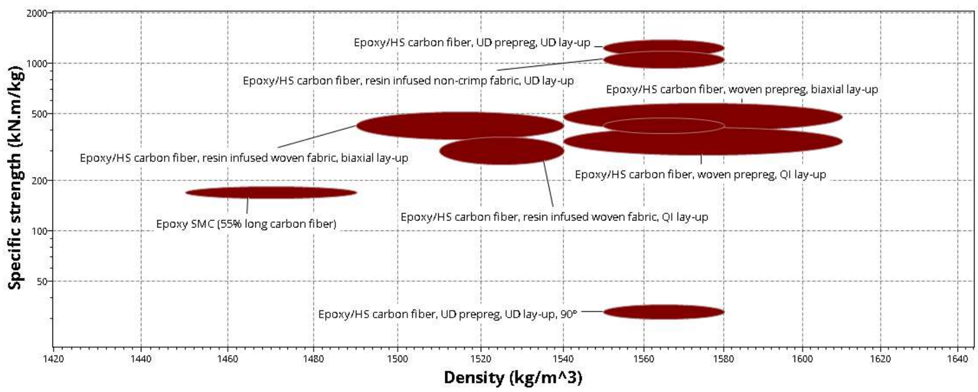

Ajustes de selección de etapa:
Mostrar resultados de todas las etapas habilitadas: Encendido
Pasar etapa cuando: alguna parte del registro está dentro de la selección

Paso de registros: 4267 de 4333

Generado por: User, 1056639 — miércoles, 28 de enero de 2026

INFORME DE SELECCIÓN

ETAPA 3:	ÁRBOL	Resumen

Registros enlazados	Pasa
[MaterialUniverse:\Hybrids: composites, foams, honeycombs, natural materials \Composites\Polymer matrix\Epoxy\Carbon fiber]	9

Paso de registros: 9 de 4333

Generado por: User, 1056639 miércoles, 28 de enero de 2026

Informe de selección

Resumen

Detalles de etapa

1. Datos para la selección

Base de datos:	Level 3 Aerospace
Tabla	MaterialUniverse
Subconjunto	Foams
Referencia	

2. Criterios de selección (resumen)

Etapa	Atributo:	Constantes
1	Young's modulus (GPa)	
	Density (kg/m^3)	
2	Density (kg/m^3)	≤ 60
3		
4	Young's modulus (GPa)	≥ 0,05
5	Shear strength (MPa)	
	Density (kg/m^3)	

3. Resultados de la selección

Paso de registros: Todas las etapas — 4 de 135

Clasificados por: Orden alfabético

Orden de rango: Bajo a alto

1	Polyetherimide foam, (closed cell, 0.06)
2	Polymethacrylimide foam (rigid, 0.051)
3	PVC cross-linked foam (rigid, closed cell, DH 0.060)
4	Styrene acrylonitrile foam (closed cell, 0.055)

INFORME DE SELECCIÓN

AJUSTES DE SELECCIÓN DE PROYECTO:
Pasar registros sin datos: Apagado

Descartar registros estimados: Apagado

Cambiar el número de registros para mostrar...

Detalles de etapa

Generado por: User, 1056639 miércoles, 28 de enero de 2026

INFORME DE SELECCIÓN

ETAPA 1:	DENSITY (KG/M^3), YOUNG'S MODULUS (GPA)	Resumen

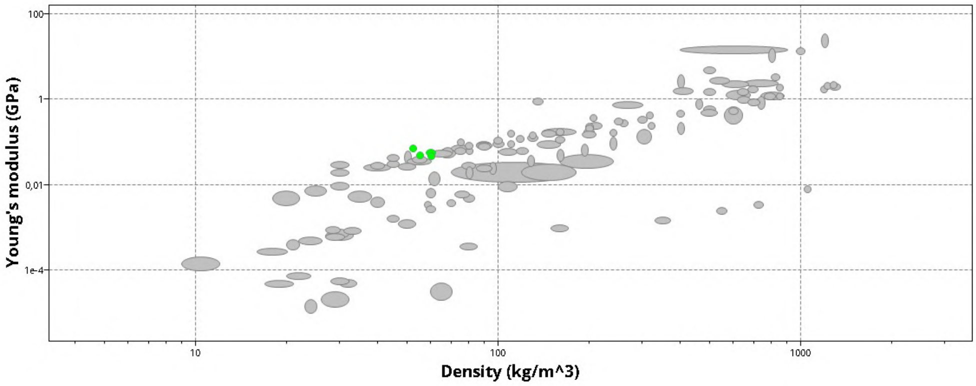

Ajustes de selección de etapa:
Mostrar resultados de todas las etapas habilitadas: Encendido
Pasar etapa cuando: alguna parte del registro está dentro de la selección

Paso de registros: 135 de 135

Generado por: User, 1056639 miércoles, 28 de enero de 2026

Informe de selección

Etapa 2:	Límite	Resumen

Constantes

Atributo:	Constantes
Density (kg/m^3)	≤ 60

Ajustes de selección de etapa:	
Pasar etapa cuando:	alguna parte del registro está dentro de la selección

Paso de registros: 40 de 135

Informe de selección

Etapa 3:	Árbol	Resumen

Registros enlazados **Pasa**

Paso de registros: 135 de 135

INFORME DE SELECCIÓN

ETAPA 4:	LÍMITE	Resumen

CONSTANTES

Atributo:	Constantes
Young's modulus (GPa)	≥ 0,05

AJUSTES DE SELECCIÓN DE ETAPA:	
Pasar etapa cuando:	alguna parte del registro está dentro de la selección

Paso de registros: 82 de 135

Informe de selección

Etapa 5:	Density (kg/m^3), Shear strength (MPa)	Resumen

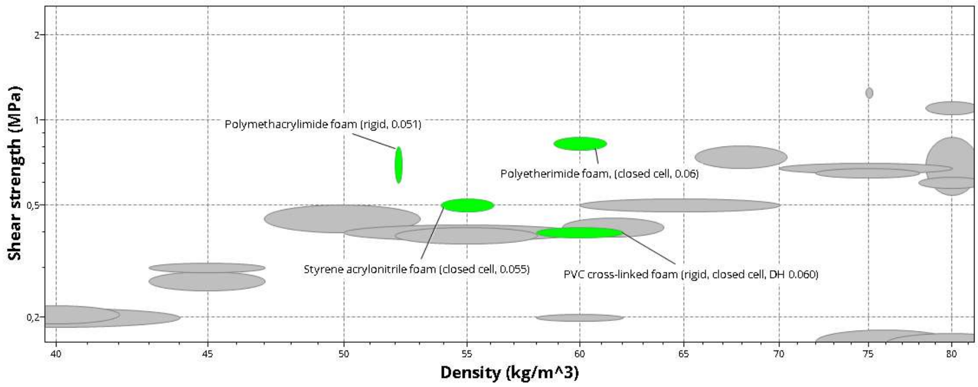

Ajustes de selección de etapa:
Mostrar resultados de todas las etapas habilitadas: Encendido
Pasar etapa cuando: alguna parte del registro está dentro de la selección

Paso de registros: 106 de 135

Informe de selección

Resumen

Detalles de etapa

1. Datos para la selección

Base de datos:	Level 3 Aerospace
Tabla	MaterialUniverse
Subconjunto	All materials
Referencia	

2. Criterios de selección (resumen)

Etapa	Atributo:	Constantes
1	Specific strength (kN.m/kg)	
	Density (kg/m^3)	
	Valor de índice (pendiente = 1)	≥ 0,0843
2	MaterialUniverse	Metals and alloys\Ferrous
		Metals and alloys\Non-ferrous
3	Young's modulus (GPa)	
	Density (kg/m^3)	
4	Density (kg/m^3)	≤ 3e3
5	Price (EUR/kg)	≤ 20

3. Resultados de la selección

Paso de registros: Todas las etapas	7 de 4333
Clasificados por:	Orden alfabético
Orden de rango:	Bajo a alto

1	Aluminum, 7055, T76511
2	Aluminum, 7068, T6511
3	Aluminum, 7255, T7751
4	Magnesium, EA55RS, T4
5	Magnesium, Elektron ZW3, F
6	Magnesium, ZC71
7	Magnesium, ZK60A-T5

Generado por: User, 1056639 — miércoles, 28 de enero de 2026

Informe de selección

Informe de selección

Ajustes de selección de proyecto:
Pasar registros sin datos: Apagado

Descartar registros estimados: Apagado

Cambiar el número de registros para mostrar...

Detalles de etapa

Informe de selección

Etapa 1:	Density (kg/m^3), Specific strength (kN.m/kg)	Resumen

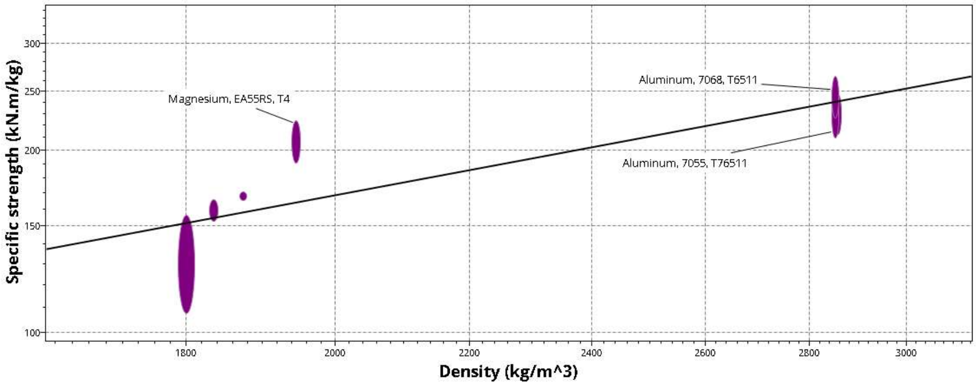

Índices

pendiente	Valor de índice	Index equation
1	≥ 0,0843	[Specific strength]/[Density]

Ajustes de selección de etapa:
Mostrar resultados de todas las etapas habilitadas: Encendido
Pasar etapa cuando: alguna parte del registro está dentro de la selección

Paso de registros: 485 de 4333

Generado por: User, 1056639 miércoles, 28 de enero de 2026

Informe de selección

Etapa 2:	Árbol	Resumen

Registros enlazados	Pasa
[MaterialUniverse:\Metals and alloys\Ferrous]	730
[MaterialUniverse:\Metals and alloys\Non-ferrous]	901

Paso de registros: 1631 de 4333

Informe de selección

Etapa 3:	Density (kg/m^3), Young's modulus (GPa)	Resumen

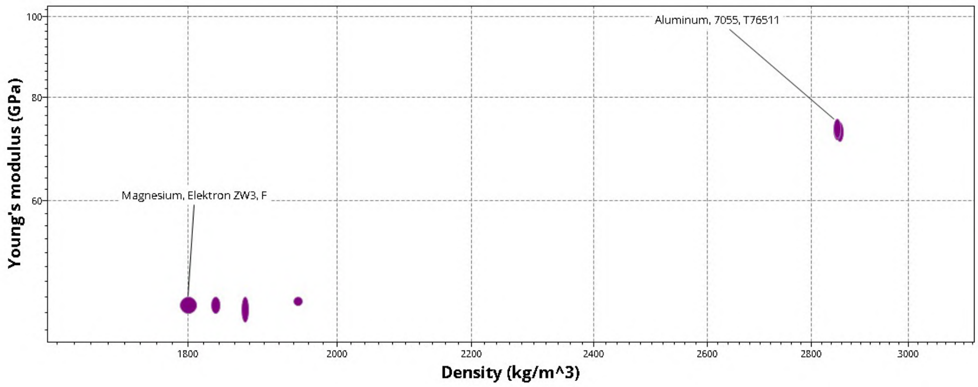

Ajustes de selección de etapa:
Mostrar resultados de todas las etapas habilitadas: Encendido
Pasar etapa cuando: alguna parte del registro está dentro de la selección

Paso de registros: 4284 de 4333

Generado por: User, 1056639 — miércoles, 28 de enero de 2026

Informe de selección

Etapa 4:	Límite	Resumen

Constantes

Atributo:	Constantes
Density (kg/m^3)	≤ 3e3

Ajustes de selección de etapa:

Pasar etapa cuando: alguna parte del registro está dentro de la selección

Paso de registros: 2433 de 4333

Informe de selección

Etapa 5:	Límite	Resumen

Constantes

Atributo:	Constantes
Price (EUR/kg)	≤ 20

Ajustes de selección de etapa:	
Pasar etapa cuando:	alguna parte del registro está dentro de la selección

Paso de registros: 3275 de 4333

Generado por: User, 1056639 miércoles, 28 de enero de 2026

1 ANNEX C: SUSTAINABLE DEVELOPMENT GOALS

1.1 Alignment with Sustainable Development Goals

The Sustainable Development Goals (SDGs) are a set of 17 objectives adopted by the United Nations in 2015 as part of the 2030 Agenda for Sustainable Development. They provide a common framework for addressing major global challenges, including sustainable industrial development, responsible use of resources, climate change mitigation, and technological innovation. The SDGs encourage governments, industries, research institutions, and universities to develop solutions that simultaneously promote economic growth, environmental protection, and social well-being.

Although the present work is focused on the optimization of composite laminates, the methodologies employed have applications far beyond motorsport. Advances in computational engineering, composite material optimization, and aeroelastic design are routinely transferred from Formula One to sectors such as aerospace, automotive engineering, renewable energy, and advanced manufacturing. Consequently, the proposed methodology contributes to several Sustainable Development Goals by promoting more efficient engineering solutions, reducing material consumption, and improving aerodynamic efficiency.

Figure 1 illustrates the 17 Sustainable Development Goals established by the United Nations.

Figure 1: The 17 United Nations Sustainable Development Goals.

This project is closely aligned with three United Nations Sustainable Development Goals, highlighting its contribution to innovation, sustainability, and responsible engineering practices.

SDG 9 – Industry, Innovation, and Infrastructure. The development of aeroelastic tailoring methodologies for composite laminates contributes to industrial innovation in motorsport and beyond. It advances the use of computational optimization, strengthens technological infrastructure, and fosters knowledge that can be transferred to automotive, aerospace, and renewable energy sectors.

SDG 12 – Responsible Consumption and Production. Composite optimization not only improves performance but also ensures efficient material usage.

By minimizing excess layers and reducing unnecessary mass, the project lowers manufacturing waste and promotes sustainable production practices. Moreover, longer lasting and better performing components reduce the frequency of replacement, leading to more responsible use of resources.

SDG 13 – Climate Action. Weight reduction and aerodynamic efficiency improvements directly contribute to lower fuel consumption and emissions. While the immediate application is motorsport, the methodologies developed can inform wider transportation industries, where sustainability and decarbonization are urgent priorities. The project therefore supports strategies for mitigating climate change.